2019

Longitudinal histopathological, immunohistochemical, and In Situ hybridization analysis of host and viral biomarkers in liver tissue sections of Ebola (EBOV) infected rhesus macaques

BOSTON UNIVERSITY

SCHOOL OF MEDICINE

Thesis

LONGITUDINAL HISTOPATHOLOGICAL, IMMUNOHISTOCHEMICAL, AND IN SITU HYBRIDIZATION ANALYSIS OF HOST AND VIRAL BIOMARKERS IN LIVER TISSUE SECTIONS OF EBOLA (EBOV) INFECTED RHESUS MACAQUES

by

ALEXANDRA GREENBERG

B.A., Johns Hopkins University, 2014
MSPH, Johns Hopkins Bloomberg School of Public Health, 2016

Submitted in partial fulfillment of the

requirements for the degree of

Master of Science

2019

Approved by

First Reader

Nicholas A. Crossland, D.V.M., DACVP
Assistant Professor of Pathology and Laboratory Medicine and
Investigator, NEIDL

Second Reader

Louis J. Toth, Ph.D.
Assistant Professor of Anatomy & Neurobiology

ACKNOWLEDGMENTS

I would like to thank Dr. Gwynneth Offner for her unending support during my time in the MAMS program and Dr. Louis Toth for his mentorship both with my thesis and while acting as his teaching assistant. I want to sincerely thank Dr. Nicholas Crossland, for his enthusiasm to invite me into his lab and train me in histopathology, immunohistochemistry, and *In Situ* hybridization techniques as well as his invaluable help with my research project and resulting thesis.

Additionally, thank you to Dr. Richard S. Bennett, PhD and his team at the National Institute of Allergy and Infectious Diseases (NIAID) Integrated Research Facility (IRF) for performing the BSL-4 work that made this project possible, collecting the rhesus macaques liver samples preparing formalin-fixed paraffin embedded tissue blocks used for this research under the Interagency agreement NOR 15 003 -001-0000. The non-human primate work completed at the NIAID Integrated Research Facility was supported by NIAID Division of Intramural Research and NIAID Division of Clinical Research and was performed under Battelle Memorial Institute Contract (No. HHSN272200700016I).

Thank you as well to Dr. Bertrand Russell Huber, MD, PhD for allowing me to use the VA-BU-LF Brain Bank's Vectra Polaris Automated Quantitative Pathology Imaging System for whole slide scanning and image acquisition.

LONGITUDINAL HISTOPATHOLOGICAL, IMMUNOHISTOCHEMICAL, AND IN SITU HYBRIDIZATION ANALYSIS OF HOST AND VIRAL BIOMARKERS IN LIVER TISSUE SECTIONS OF EBOLA (EBOV) INFECTED RHESUS MACAQUES

ALEXANDRA GREENBERG

ABSTRACT

INTRODUCTION: Ebola virus (EBOV) is a highly infectious and often lethal filovirus that causes hemorrhagic fever, with a reported case fatality rate of 40–90%. There are currently no Food and Drug Administration (FDA) approved medical countermeasures (MCMs) for EBOV. Non-human primates (NHPs) remain the gold standard animal model for EBOV research as they most accurately recapitulate human disease.

OBJECTIVE: This study aimed to characterize the temporal viral pathogenesis of EBOV in the liver of infected rhesus macaques using routine histopathology, multiplex immunohistochemistry (mIHC) and multiplex fluorescent *In Situ* Hybridization (mFISH), refined by digital pathology (DP) and image analysis (DIA).

METHODS: 21 FFPE liver sections from EBOV-infected rhesus macaques were examined microscopically (Uninfected controls n=3; 3 DPE n=3; 4 DPE n=3; 5 DPE n=3; 6 DPE n=3; Terminal n=6). Tissues were stained with H&E and PTAH for histopathological scoring. Three serial sections were fluorescently immunolabeled or hybridized under three independent conditions (1.EBOV VP35, Tissue Factor, CD68; 2.EBOV VP35, Heppar, Myeloperoxidase (MPO); 3.EBOV *VP35*, *IL-6*, *ISG-15*). *S*lides were digitized by a Vectra Polaris™ fluorescent whole slide scanner and DIA was conducted using Halo™ image analysis software. Statistical analysis was conducted using GraphPad Prism™ 8.0.

RESULTS: Comparing **peracute** (3-4 DPE) to **acute** (5-6 DPE) and **terminal** (6-8 DPE) EBOV infection, there is a statistically significant ($p < 0.05$) increase in hepatic inflammation and fibrin thrombi, correlating with an absolute increase in macrophages (CD68), neutrophils (MPO), and total % of Tissue Factor in the liver. There is also a significant increase in the severity of necrosis, which correlates with a decrease in Heppar. While there was significant colocalization of VP35 and CD68 starting at 4 DPE, there was only rare colocalization of VP35 with Heppar, even in terminal animals. Similar to mIHC, progressive and statistically significant differences were observed in gene expression when comparing **peracute** to **acute** and **terminal** EBOV infection. *IL-6* predominated within periportal fibrovascular compartments, but also colocalized within cells concurrently expressing EBOV *VP35*. EBOV *VP35* expression was observed within histiocytes, endothelial cells, and less commonly hepatocytes. *ISG-15* expression was observed in periportal regions and in proximity to cells expressing EBOV *VP35*, but colocalization within EBOV *VP35* expressing cells was an extremely rare event.

CONCLUSION: Qualitative tools are well suited for confirming virulence and viral tissue tropism, but do little to build on our current understanding of disease. Using DIA in partnership with mIHC and mFISH, this study quantified statistically significant temporal changes in the immunoreactivity and hybridization of host and viral biomarkers that have previously been linked to the pathogenesis of EBOV. Taken together, these tools have enabled us to characterize minute changes that reflect magnitudes of biological variability simply not feasible to detect with the human eye. Furthermore, spatial context has refined our current understanding of differential gene expression of EBOV, which has the potential to aid in development of host-directed therapies. The establishment of these benchmarks will serve as a guide for the validation of cross-institutional EBOV animal models.

TABLE OF CONTENTS

LIST OF TABLES

LIST OF FIGURES

LIST OF ABBREVIATIONS

ALT ..... Alanine Transaminase

ANOVA ..... Analysis of Variance

AQ ..... Area Quantification

AR ..... Antigen Retrieval

AST ..... Aspartate Transaminase

BSL ..... Biosafety Level

BU ..... Boston University

BUN ..... Blood Urea Nitrogen

CBC ..... Complete Blood Count

DIA ..... Digital Image Analysis

DIC ..... Disseminated Intravascular Coagulation

DP ..... Digital Pathology

DPE ..... Days Post-exposure

EBOV ..... Ebola Virus

EDV ..... Ebola Virus Disease

FDA ..... Food and Drug Administration

FFPE ..... Formalin-fixed Paraffin-embedded

FISH ..... Fluorescent *In Situ* Hybridization

FL ..... Fluorescent

H&E ..... Hematoxylin and Eosin

HP ..... High-Plex

IHC ..... Immunohistochemistry

IL-6 ..... Interleukin-6

iPSC ..... immortalized Pluripotent Stem Cell

IRF ..... Integrated Research Facility

ISG-15 ..... Interferon-stimulated Gene-15

MARV ..... Marburg Virus

MCMs ..... Medical Countermeasures

mdDC ..... Monocyte-derived Dendritic Cells

MPO ..... Myeloperoxidase

MPS ..... Mononuclear Phagocytic System

NEIDL ..... National Emerging Infectious Diseases Laboratories

NHPs ..... Non-human Primates

NIAID ..... National Institute of Allergy and Infectious Diseases

PBMC ..... Peripheral Blood Mononuclear Cell

PHH ..... Primary Human Hepatocyte

PT ..... Pro-thrombin

PTAH ..... Phosphotungstic Acid-Hematoxylin

PTT ..... Partial Thromboplastin Time

ROI ..... Region of Interest

RT-PCR ..... Reverse Transcription Polymerase Chain Reaction

TF ..... Tissue Factor

WSI ..... Whole Slide Image

INTRODUCTION

Ebola virus (EBOV) is a highly infectious and often lethal filovirus that causes hemorrhagic fever, with a reported case fatality rate of 40-90% (Mühlberger & Hensley, 2017; Speranza et al., 2018). The high variability in case fatality has been attributed to differences in virulence across different species and strains of EBOV, and variations in case reporting and case management (Lefebvre et al., 2014). EBOV transmission in competent host species occurs through direct exposure via broken skin and/or mucosal surfaces to infected body fluids (i.e. vomitus, diarrhea, semen, etc.), typically after and not during the incubation period (Meyers et al., 2015). Early clinical manifestations include non-specific flu-like symptoms such as fever, chills, diarrhea, dehydration, fever and lymphadenopathy. Disseminated intravascular coagulation (DIC), is a late-stage sequelae in humans and NHPs, which typically manifest between 6-10 days post-infection and is clinically represented by prolonged PT (pro-thrombin) and PTT (partial thromboplastin time) times, thrombocytopenia, and cutaneous, mucosal, and alimentary petechial and echymotic hemorrhages. The cause of DIC is multifactorial, and ultimately is attributed to a combination of endothelial dysfunction and enhanced vascular permeability, activation of the coagulation cascade with microvascular fibrin thrombosis, depletion of platelets and clotting factors, hepatocellular degeneration and necrosis resulting in decreased production of clotting factors, and a generalized pro-inflammatory state driven by inflammatory cytokines and chemokines including IL-1, IL-6, IL-8, INF-a and TNF-a (Hutchinson & Rollin, 2007). In severe cases, disease progression leads to

hypovolemic shock, sepsis, multiple organ failure, and death (Geisbert et al., 2003a; El Sayed et al., 2016). There are currently no Food and Drug Administration (FDA) approved medical countermeasures (MCMs) for EBOV prevention or treatment (Lin et al., 2015; Mühlberger & Hensley, 2017; Nakayama & Saijo, 2013) although there are an increasing number of experimental vaccines and post-exposure countermeasures currently under development (Hayden, Bausch, & Friede, 2017).

Due to the magnitude and widespread distribution of the 2013-2016 West African EBOV outbreak, there has been an unprecedented urgency to improve our knowledge of EBOV pathogenesis, as well as to enhance our ability to develop and validate the safety and efficacy of novel diagnostic tests, vaccines, and therapeutic interventions (Mühlberger & Hensley, 2017). The 2013-2016 outbreak was the largest EBOV outbreak to date, declared a Public Health Emergency of International Concern by the World Health Organization, with over 28,500 cases, greater than ten times the cumulative cases from all past Ebola outbreaks combined. There were more than 11,000 deaths reported across fifteen countries, which came with exceptional social, economic, and political costs (Mühlberger & Hensley, 2017). The never-before-seen scale of this outbreak was in part due to lack of healthcare infrastructure and resources in affected countries, insufficient and unprepared local healthcare workforce, and the spread of the virus into densely populated urban centers and eventually, across borders (Buseh et al., 2015). As the world becomes more and more interconnected, outbreak containment for highly infectious diseases like Ebola will become a greater challenge than ever before, making it

paramount that governmental and private appropriations continue to fund research aimed at developing and validating the safety and efficacy of MCMs.

Experimental Therapeutics for EBOV

Before 2013, scientific research on efficacy of EBOV prevention and treatment measures and pathogenesis studies were limited (Speranza et al., 2018). In 2002, the FDA established the *"Animal Rule"*. This new rule permitted the demonstration of efficacy for MCMs using animal studies in lieu of human clinical trials, in those instances where human trials would be unethical because of the serious clinical effects of the agent and where field trials would not be feasible because of the infrequency of human exposure to the agent. Preclinical development of MCMs in animal models is done through highly regulated and controlled studies, which facilitates collection of robust data sets to determine MCM efficacy. During the outbreak, clinical trials for promising vaccine candidates and monoclonal antibody therapies (Table 1), which had previously demonstrated efficacy in preclinical animal models, were accelerated in disease-affected countries, but only one trial demonstrated vaccine efficacy in humans (Mühlberger & Hensley, 2017; Espeland et al., 2018; Dhama et al., 2018). Given that clinical trials began late in the outbreak, it was not possible to reach statistically significant sample sizes for many of the studies before the outbreak ended. Furthermore establishing efficacy of MCMs in natural human outbreaks is inherently more challenging when comparing to animal models as the definitive time from inoculation to treatment, route of administration, or inoculation dosage cannot be determined and other confounding

variables, such as comorbidities and variation in the degree of local healthcare infrastructure and capacity are well established (Carter et al., 2018).

Additionally, recent research has shown that virus persists in EBOV survivors through isolation from aqueous humor in patients with uveitis and semen from men weeks after resolution of clinical disease (Chughtai, Barnes, & Macintyre, 2016). Because of this, it is now recommended that any EBOV vaccine confer immunity for at least 2 years (Dhama et al., 2018). Demonstration of statistically significant long-lasting immunity following vaccination requires ongoing clinical trials, but trial length is typically dependent on the duration of outbreaks. There are currently new trials underway for EBOV vaccines and treatments, including monoclonal therapies and antivirals (Table 1), in the Democratic Republic of Congo in response to a new outbreak that began in 2018 (National Institute of Allergy and Infectious Diseases, 2018).

While there are now experimental therapeutics available for EBOV and additional candidates undergoing animal and human testing, our understanding of EBOV viral pathogenesis and viral persistence in human survivors remains incomplete, which will likely be a challenge for approval of any MCMs under "*Animal Rule"*, due to the requirement to demonstrate mechanism of action of vaccines and drugs in animal models (Food & Drug Administration CDER, 2015). Continued pathogenesis research is therefore imperative to develop and adopt MCMs that can prevent and mitigate future public health emergencies due to the spread of EBOV.

Table 1. Experimental EBOV treatments and vaccines.

Type of MCM	Name	Formulation and Target	Company	Trial(s) & Results
VACCINES	*rVSV-ZEBOV vaccine candidate (V920)*	Single dose Vesicular stomatitis virus (VSV)-based vaccine; targeting EBOV Glycoprotein (GP)	Merck	Phase III trial in Guinea; safe and effective in adults >18; rapid immune response sustained up to one year post-vaccination
	Ad26-ZEBOV/MVA-BN-Filo vaccine candidates	Prime-boost regimen; Adenovirus-based prime & modified vaccinia virus Ankara boost at 28 or 56 days; targeting EBOV GP & VP40	Janssen Vaccines & Prevention B.V. in collaboration with Bavarian Nordic GmbH	Phase III clinical trial, did not reach statistical significance
	ChAd3-EBO-Z vaccine candidate	Single dose Adenovirus-based vaccine; targeting EBOV GP	GlaxoSmithKline	Phase II
		Ad-based vaccine given in combination with a booster dose of the MVA-BN-Filo vaccine candidate	Bavarian Nordic GmbH	Phase III trial; elicited B- and T-cell immune responses; did not reach statistical significance
TREATMENTS	*ZMapp*	3, chimeric monoclonal antibody (mAb) cocktail	Mapp Biopharma-ceutical	PREVAIL II Phase I/II clinical trial in Guinea, Liberia, Sierra Leone, and the US; did not reach statistical significance but showed a trend towards efficacy
	REGN-3470-3471-3479	Fully human 3-mAb cocktail	Regeneron	Undergoing Phase I clinical study
	Favipiravir	Broad-spectrum antiviral active against RNA viruses	Toyama Chemical	Phase I/II Trial in Guinea, did not reach statistical significance
	Remdesivir	Antiviral drug	Gilead Sciences	Undergoing Phase I clinical study

**Information in table adapted from Espeland et al., 2018 and Dhama et al., 2018.*

Ebola Virus, Viral Pathogenesis, and Host Response

EBOV is a single-stranded, negative-sense RNA virus, with the genome encoding seven structural viral proteins from the 5' to 3' end: nucleoprotein (NP), viral protein 35 (VP5), viral protein 40 (VP40), glycoprotein (GP), viral protein 30 (VP30), viral protein 24 (VP24), and RNA Polymerase (L). GP is the only structural protein expressed as a transmembrane protein on the virion surface, facilitating viral entry via host cell attachment, receptor binding, and membrane fusion within the endosome (Lee & Saphire, 2009). EBOV viral RNA is encapsidated by nucleocapsid proteins to form a ribonucleoprotein (RNP) complex, which is the minimum replicative unit of EBOV. Polymerized nucleocapsids form filamentous EBOV viral particles composed of 5 EBOV structural proteins: NP, VP35, VP30, L and VP24. NP, VP35, and V24 are essential and sufficient to mediate nucleocapsid transport within the host cytoplasm (Takamatsu, Kolesnikova & Becker, 2018). NP encapsidates the genome, while VP35 is a polymerase cofactor, VP30 is a transcriptional activator, and RNA polymerase L facilitates genome replication and transcription. VP24 facilitates RNP assembly (Baseler et al., 2017). VP40 is a membrane-associated matrix protein, which regulates viral transcription, coordinates RNP and virion assembly in host cells, and facilitates viral budding from infected cells (Madara et al., 2015). Additionally, VP35 and VP24 have been shown to inhibit the immune response by blocking interferon production and signaling (Lubaki et al., 2016). VP35, which is the second most abundant EBOV protein, has been shown in recent studies to have additional functions that interfere with the early innate immune response (Baseler et al., 2017), making it a useful marker for quantification of EBOV and

comparison with interferon activity in infected animals.

Recent studies, in addition to providing insight into the EBOV genome and viral structure, have shed new light on how EBOV infection is established and how the virus disseminates in the body. Research in both humans and non-human primates has shown that following infection, EBOV spreads through blood vessels and lymphatics, likely via monocytes, macrophages and dendritic cells, which have previously collectively been referred to as the mononuclear phagocytic system (MPS), with subsequent endothelial replication and dissemination to sites of secondary viral replication, specifically the lymph nodes, spleen, and liver (Martines, et al., 2014; Mühlberger & Hensley, 2017). EBOV causes widespread immune dysregulation with upregulation of interferon (IFN) and IFN-stimulated genes (ISGs), including ISG-15, release of cytokines and chemokines, including interleukin-6 (IL-6), and impairment of the innate immune response (Speranza & Connor, 2017; Caballero et al., 2016).

ISG-15 and IL-6 were selected for use in this study based on published and ongoing research at the NEIDL that indicates significant global upregulation of these genes in response to EBOV infection in vitro and in vivo (Speranza & Connor, 2017), as well as availability of biomarker reagents for multiplex fluorescent *In Situ* Hybridization. IFN-stimulated gene-15 (ISG-15) is an antiviral ubiquitin-like protein expressed by both immune and non-immune cells, found both freely intracellular and as a protein modifier extracellular, that has been shown to inhibit ubiquitination of Ebola VP40 protein and subsequently prevent viral budding in vitro in human cells (dos Santos & Mansur, 2017; Hermann & Bogunovic, 2017). IL-6 is a cytokine produced by various immune and non-

immune cells for host defense in response to infection and tissue injury (Tanaka, Narazaki, & Kishimoto, 2014). IL-6 has pro-inflammatory effects, particularly in the liver, where it stimulates production of C-reactive protein, serum amyloid and fibrinogen and reduces production of fibronectin, albumin, and transferrin. IL-6 contributes to increased platelet production and thrombocytosis and when its production is upregulated, contributes to cytokine storm, similar to what has been seen in EBOV (Tanaka, Narazaki, & Kishimoto, 2014; Hellman, 2015). IL-6 has also been shown to induce synthesis of Tissue Factor (TF) by human peripheral blood monocytes (PBMCs) and PBMCs have been found to increase production of TF during EBOV (Blackwell Science Ltd, 2001; Geisbert et al, 2003b). TF is the membrane receptor for coagulation factors VII and VIIa and is responsible for initiation of the external coagulation cascade. It can be found on multiple cell phenotypes and plays an essential role in thrombosis and inflammation. In EBOV it has been shown to increase significantly, leading to accumulation of fibrin and contributing to development of DIC (Geisbert et al., 2003b). Following EBOV infection, changes are also observed in complete blood count (CBC) including lymphopenia, thrombocytopenia and neutrophilia. Eventually, this can be followed by multi-organ failure and death 1-to-2 weeks post-symptom onset, although factors contributing to variations in disease severity are poorly understood (Nakayama & Saijo, 2013; Speranza et al., 2018).

While the spleen is also a major site of viral replication, with a large resident macrophage cell population, terminal disease in NHPs corresponds with peak viral loads in the liver associated with hepatocellular degeneration and necrosis (Martines et al.,

2014; Spengler et al., 2017). Gross findings of EBOV infection include an enlarged pale friable liver. This is histologically characterized by kupffer cell hyperplasia, hepatocyte degeneration and necrosis, and intracytoplasmic inclusion bodies that represent viral nucleocapsid aggregates. Clinical laboratory tests show an initial increase in liver leakage enzymes aspartate transaminase (AST) and alanine transaminase (ALT), followed by prolonged clotting times (PT and PTT), and decreased albumin and total protein. These findings are suggestive of hepatocellular injury and decreased liver function respectively; albeit hypoalbuminemia is also likely attributed to loss in fluids if supported clinically (i.e. vomiting and diarrhea). Additional findings include azotemia represented by rising blood urea nitrogen (BUN) and creatinine, which is primarily attributed to pre-renal disease/dehydration caused by hypovolemia. Renal tubular necrosis has also been observed microscopically indicating direct renal disease also may play a role in azotemia (Cooper et al., 2018; Lin et al., 2015; Martines et al., 2014). Recent studies have shown that increased viral titers in the liver (quantified via RT-PCR) and markedly elevated AST levels are associated with lower EBOV survival rates (Reisler et al., 2017; Speranza et al., 2018). Yet, viral replication in hepatocytes remains poorly characterized and discrete histopathological changes in the liver have not previously been investigated longitudinally and quantified in NHPs or in vitro models of primary hepatocyte cell lines (Spengler et al., 2017).

Animal Models of EBOV

Due to ethical concerns, the classification of EBOV as a select agent, requirement of Biosafety Level 4 (BSL-4) containment, and the sporadic and unpredicted nature of outbreaks, studies on both human and animal samples for EBOV infection have been limited (Martines et al., 2014). Research on EBOV pathogenesis, particularly in the liver, has been conducted in various animal models, including humanized mice, guinea pigs, ferrets, and NHPs, specifically baboons, marmosets, cynomolgus macaques and rhesus macaques (Martines et al., 2014; Perry, Bollinger, & White, 2012; Smither et al., 2015). Routes of viral inoculation utilized in animal models have included intramuscular, conjunctival, oral, aerosol and intranasal (Cooper et al., 2018; Martines et al., 2014; Reisler et al., 2017; Spengler et al., 2017; Speranza et al., 2018; Johnson et al., 1995). NHPs represent the gold standard for EBOV research, given their high fidelity to recapitulate human disease pathophysiology. NHPs do not require viral adaptation and typical signs include the development of a macular rash, petechial and ecchymotic hemorrhages, coagulation abnormalities, elevated liver enzymes, thrombocytopenia, lymphocytopenia, and robust pro-inflammatory cytokine responses (Hoenen et al., 2006).

With the exception of a single longitudinal study in cynomolgus macaques (Geisbert et al., 2003a), the majority of NHP studies have examined the terminal stage or chronic clinically resolved stages of EBOV disease (Lin et al., 2015; Nakayama & Saijo, 2013). Microscopically, the temporal and spatial progression of EBOV in the liver from initial viral replication to death or recovery has yet to be characterized. Little is known about what causes inter-host variability in EBOV infection, although EBOV severity has

been linked to increased viral load in the liver (Reisler et al., 2017). Further research is warranted concerning hepatocellular dysfunction and death in EBOV and mechanisms of EBOV driven aberrations of host-immune response in the liver.

Well-characterized models of EBOV infection are indispensable for the development of MCMs, given that their approval will likely require use of the FDA's *"Animal Rule"* (Mühlberger & Hensley, 2017). There are four criteria that must be met for *"Animal Rule"* to be used to approve MCMs based on animal studies (Table 2), one of which is that the pathophysiology of EBOV must be well understood and proven to be consistent across the model(s) used and in humans (Snoy, 2010).

Table 2. Animal Rule Criteria as defined by the FDA.

(1) Mechanism of Action for MCM is clear	"There is a reasonably well-understood pathophysiological mechanism of the toxicity of the substance and its prevention or substantial reduction by the product."
(2) Multiple animal models (or one animal model with high fidelity to human disease pathogenesis) demonstrate effect of MCM	"The effect is demonstrated in more than one animal species expected to react with a response predictive for humans, unless the effect is demonstrated in a single animal species that represents a sufficiently well-characterized animal model for predicting the response in humans."
(3) Same endpoint used in animal study as desired in humans	"The animal study endpoint is clearly related to the desired benefit in humans, generally the enhancement of survival or prevention of major morbidity."
(4) Pharmacokinetics and pharmacodynamics in animal model(s) can be extrapolated to humans	"The data or information on the kinetics and pharmacodynamics of the product or other relevant data or information, in animals and humans, allows selection of an effective dose in humans."

Rodents, including mice and hamsters, require viral adaptation or immunosuppression to cause clinical disease and do not exhibit all of the hallmarks of EBOV host-response as observed in humans and NHPs, making them suboptimal models for evaluating MCMs. For example, mice infected with mouse-adapted EBOV, unlike humans and NHPs, do not develop DIC and in guinea pigs that do exhibit fibrin deposition and coagulopathy, it is much less severe than in humans and NHPs (Nakayama & Saijo, 2013). NHPs such as rhesus macaques present their own ethical and logistical challenges, which include consistently higher case fatality rates than humans, and are expensive and cumbersome to work with, but remain the gold standard model for characterizing the pathogenesis of EBOV and for evaluating MCMs.

Given the inherent challenges of working with animal models, a demand for novel, more convenient and affordable disease models for EBOV are desired. Limitations for existing in vitro models using immortalized human hepatocytes, such as the Huh7 human hepatocarcinoma cell line, include the absence of TLR4 expression (an important innate pathogen pattern recognition receptor for EBOV) and the absence of a robust interferon response when infected with EBOV (Preliminary data, Mühlberger Lab, NEIDL). Preliminary partnership studies with the CReM and NEIDL have shown that primary hepatocytes derived from induced pluripotent stem cells (iPSCs) and liver organoids more faithfully recapitulate the host-viral responses observed in natural disease, including a robust interferon and cytokine response. These novel *in vitro* platforms will be invaluable resources for investigating basic science research and will propel translational studies using animal models (Bennett et al., 2017).

Specific Aims

The purpose of this study was to characterize the pathogenesis of acute in vivo Ebola (EBOV) infection in the liver of infected rhesus macaques. The ultimate goal was to characterize the host response signature to EBOV infection over time, which can then serve as a benchmark for novel models such as iPSCs, liver organoids, and a platform for evaluating efficacy of EBOV MCMs, including vaccines and antiviral therapies. This work used digital image analysis to provide novel insights into the organ-specific host response to EBOV.

Experiments were conducted to:

1) Characterize histomorphological features of EBOV in the liver utilizing routine hematoxylin and eosin and Phosphotungstic Acid-Hematoxylin (PTAH) staining
2) Quantify the temporal spread of viral infection within unique hepatic compartments utilizing multiplex immunofluorescence
3) Quantify host gene expression of cellular pathways involved in pro-inflammatory and innate immunity in response to EBOV

Below are histopathological, immunohistochemical, and *In Situ* hybridization findings collected from a group of 21 rhesus macaques. Data was obtained from liver samples provided by the National Institute of Allergy and Infectious Diseases Integrated Research Facility (NIAID IRF).

METHODS

Animals and Method of Infection

The NHP tissue samples used in this study (Table 3) were collected by the NIAID IRF under Battelle Memorial Institute Contract No. HHSN272200700016I and provided for use at the NEIDL under the Interagency agreement NOR 15 003 -001-0000. The IRF conducted a challenge study to explore EBOV Kikwit natural history with 27 rhesus macaques of Chinese origin. Our laboratory reviewed samples collected during scheduled or terminal endpoint-triggered necropsy from 3 control animals and 18 EBOV infected macaques, six of which were terminal (6-8 DPE). Euthanasia criteria for terminal animals were developed prior to study start and only clinical signs were used in the euthanasia decision. No secondary hematology or chemistry values were utilized. Clinical signs of appearance, respiration, recumbency, and non-responsiveness were scored on a predetermined scale (Appendix I). When the score total was 8 or 9, the PI or a co-investigator consulted with the facility veterinarian and a decision was made regarding euthanasia. Animals were euthanized immediately when a total score of ≥ 10 was reached. Animals that were moribund, as evidenced by a core temperature below 34°C (<93°F), or were in severe respiratory distress were also euthanized immediately.

Under BSL-4 conditions at the NIAID IRF, animals were exposed to EBOV/Kikwit isolate diluted to a target concentration of 1,000 PFU in a volume of 1 mL /dose. Injections were delivered intramuscularly into the left lateral triceps muscle on 13-DEC-2017, 03-APR-2018, 06-MAY-2018, and 17-MAY-2018 for challenge groups 1-4,

respectively. The injection site was consistent across all NHPs and marked for tissue collection at necropsy. Control animals were not injected with EBOV/Kikwit. EBOV/Kikwit-exposed animals were observed for the development of clinical signs of EBOV infection and, to allow for temporal analysis of EBOV pathogenesis post-infection, were humanely euthanized either at terminal endpoints (6-8 DPE) or at predetermined time points (3-6 DPE) before a necropsy was performed.

Table 3. Non-human primates used in this study (excludes Challenge Group 1).

Study Group	Challenge Group	Animal Number	Animal Tattoo	Sex	Weight (first baseline, kg)	Birth Date
Non-infected control	2 (not infected)	NHP C1	RA1082	Female	7.32	15MAR2011
		NHP C2	RA1819	Female	4.72	18MAR2012
		NHP C3	RA1856	Male	8.08	15MAR2012
Terminal (no manipulations)	1	NHP1	RA1565	Male	13.02	27APR2012
		NHP2	RA0451	Female	6.58	15APR2011
		NHP3	RA0787	Female	6.60	09FEB2011
		NHP4	RA1777	Male	10.02	30APR2012
		NHP5	RA0561	Male	8.08	22JUN2011
		NHP6	RA0710	Female	5.42	16MAY2011
Terminal (routine manipulations)	2	NHP7	RA0700	Female	5.48	12MAY2011
		NHP8	RA1818	Female	6.30	8MAR2012
		NHP9	RA1779	Male	10.98	15SEP2011
		NHP10	RA1790	Female	5.82	30MAY2011
		NHP11	RA0917	Male	9.32	19APR2011
		NHP12	RA1423	Male	8.26	22NOV2012
3 DPE Scheduled Necropsy	3	NHP13	RA0223	Male	10.14	15APR2012
		NHP14	RA0449	Female	6.64	20MAR2011
		NHP15	RA1834	Female	5.96	29MAY2012
5 DPE Scheduled Necropsy	3	NHP16	RA0452	Female	5.10	21MAR2011
		NHP17	RA0522	Female	7.34	07APR2011
		NHP18	RA1639	Female	8.04	12APR2012
4 DPE Scheduled Necropsy	4	NHP19	RA0717	Female	6.10	21OCT2011
		NHP20	RA0850	Male	9.46	21NOV2011
		NHP21	RA1849	Male	8.10	04FEB2012
6 DPE Scheduled Necropsy	4	NHP22	RA1074	Female	7.42	30APR2011
		NHP23	RA1325	Male	10.86	25MAY2011
		NHP24	RA1803	Female	5.32	04MAR2012

For this follow-on study, only Challenge Group 2 Terminal animals as well as Group 3 and 4 scheduled necropsy animals were evaluated. Liver samples were collected during a scheduled or terminal endpoint-triggered necropsy in bead beater tubes with TRIzoI or as formalin-fixed tissue blocks to measure interferon responses in these tissues.

All animals were humanely euthanized in accordance with defined experimental endpoints and gross necropsy was performed. The requested tissues were collected (at least one dimension <1 cm) and were inactivated according to IRF SOP SF-24 in the NIAID IRF BSL-4 facility. Samples were fixed for 72 hours in 10% neutral buffered formalin, after which a buffer exchanged was performed, removed from the BSL-4 laboratory, processed in a Tissue-Tek VIP-6 automated vacuum infiltration processor (Sakura Finetek USA, Torrance, CA, USA), followed by paraffin embedding with a Tissue-Tek model TEC unit (Sakura Finetek USA, Torrance, CA, USA). Once inactivated, tissue samples were treated as non-infectious and all subsequent histopathological staining and analysis was performed in BSL-2 conditions at the NEIDL.

Brightfield histopathological preparation and evaluation

5 μm histology sections were prepared using formalin-fixed paraffin-embedded (FFPE) tissues from the liver, cut using a Leica RM2255 Fully Automated Rotary Microtome. Tissue samples were deparaffinized in xylene and rehydrated in a graded ethanol series followed by washing in distilled water. All slides were stained with hematoxylin and eosin (H&E) before mounting. Phosphotungstic acid-haematoxylin stain (PTAH) was used on some liver sections to confirm fibrin deposition suspected based on

H&E findings. Brightfield images were captured with a Leica DM2500 LED microscope at 400x (dry) - 600x (oil immersion).

All slides were reviewed for specific microscopic features to determine pathologic changes across time points and assess inter-animal variability. Dr. Nicholas Crossland, a board-certified veterinary pathologist, performed scoring based on severity of these features, while blinded to clinical and biochemical data for each specimen. Based on preliminary observations, definitions were set for semi-quantitative, ordinal or binary scores to use for progression of specific morphological features in the liver and overall severity of organ-specific histopathological changes. Parameters evaluated were degree of inflammation, necrosis, and fibrin deposition as well as presence or absence of intracytoplasmic eosinophilic viral inclusions. A composite score was assigned for each animal based on the sum of the values assigned for each individual evaluated parameter (Table 4).

Table 4. Criteria used for Histopathological Scoring of the liver.

Necrosis	
0 (Absent)	No necrosis
1 (Minimal)	Rare multifocal single cell necrosis adjacent to sinusoidal histiocytic inflammation
2 (Mild)	Multifocal necrosis of neighboring hepatocytes ; more widespread
3 (Moderate to marked)	Multifocal coalescing areas of hepatocellular loss (absence of hepatocytes in large areas replaced by fibrin, edema, hemorrhage and inflammatory cells)
Inflammation	
0 (Absent)	No inflammation
1 (Mild)	Rare, multifocal, localized inflammation within sinusoids consisting of aggregated histiocytes and neutrophils
2 (Moderate)	Sinusoidal expansion by > 5 neighboring histiocytes admixed with variable numbers of neutrophils
3 (Severe)	Inflammatory foci consisting of neutrophils admixed with histiocytes and fibrin in areas of hepatocellular loss (necrosis)
Fibrin deposition	
0 (Absent)	No fibrin deposition evident
1 (Mild)	Rare, multifocal occlusion of sinusoids by fibrin
2 (Moderate)	Routine, multifocal occlusion of sinusoids and veins by fibrin thrombi
Inclusions	
0 (Absent)	No viral inclusions observed
1 (Present)	Eosinophilic cytoplasmic viral inclusions observed

Statistical Analysis for Brightfield Histopathology

For liver semi-quantitative histopathological scores, given the ordinal nature of the data, the non-parametric Kruskal Wallis test was used to evaluate for statistical significance between days post-exposure (DPE) and histology scores over time across the six unmatched groups (Control, 3 DPE, 4 DPE, 5 DPE, 6 DPE, and Terminal/7-9 DPE). The two-stage linear step-up procedure of Benjamini, Krieger and Yekutieli was applied, threshold (α rate of 0.05), a priori to correct for multiple comparisons. GraphPad Prism 8.0 was used for all statistical tests and formulation of graphical depictions of results.

Multiplex Fluorescent Immunohistochemistry (mIHC)

Multiplex fluorescent immunostaining was conducted following the Opal™ 4-color User Manual (Akoya Biosciences, Menlo Park, CA, USA). Independent 3-plex immunohistochemistry panels were developed, optimized and applied on serial sections of liver derived from each of the 21 animals outlined in this study, prepared via the same workflow used for brightfield slides. Antibodies included EBOV VP35 and a combination of liver associated host proteins, known to differentiate specific anatomical compartments and/or cell types (Table 5).

Before mIHC was performed, individual antibodies were optimized via single-plex IHC with each primary antibody on 9 liver section slides. Three slides were stained with the manufacture's recommended primary dilution and there were 3 slides each with two-fold and 4-fold dilutions. For each dilution, 1, 2 and then 3 ARs were performed on different slides to evaluate the influence of repeated antigen retrieval (AR) for the given antibody. Images were taken of each slide using the same exposure time to select the optimal primary antibody dilution, the dilution with the most specific and broadest dynamic range, and to determine the final order of antibodies for mIHC (Table 5).

For mIHC, 5 μM tissue sections were cut from FFPE liver samples from each non-infected and EBOV infected rhesus macaques. Tissues were then deparaffinized and soaked in 10% formalin for 20 minutes before undergoing heat-mediated antigen retrieval (AR) using AR6 buffer and a steamer set to 100° C to ensure uniform heating of the tissue. Subsequent heat-mediated ARs were also performed under these conditions. Slides were incubated in antibody diluent/blocking agent for 10 minutes to block endogenous

peroxidase activity. Then primary antibodies for the given 3-plex mIHC were applied at the concentration and in the order determined through optimization, followed by visualization (Table 5).

Table 5. Optimized mIHC conditions.
**mIHC-3 (Appendix II) is not included because, while* WSIs *were collected, DIA could not be performed.*

Condition	**Primary Antibody**	*Animal and Isotype*	*Tissue marker*	Manufacturer, Catalog # and Lot #	Concen-tration	**TSA-conjugated Fluorochrome**	Manufacturer, Catalog # and Lot #	Concen-tration	**AR**
1	Anti-Zaire Ebola VP35	Ms IgG2b	EBOV Viral particles	Kerafast EMS703 090315	1/300	Green (Opal 520)	PerkinElmer FP1487A 2380385	1/400	1
	Heppar (OCH1E5)	Ms IgG1	Hepatocytes	ThermoFisher MA5-12417 TD2559592A	1/50	Far red (Opal 690)	PerkinElmer FP1497A 2491340	1/100	2
	Myelo-peroxidase (MPO)	Rb IgG	Neutrophils	ThermoFisher PA5-16672 TE2572301G	1/200	Red (Opal 570)	PerkinElmer FP1488A 2496488	1/200	3
2	VP35	Ms IgG2b	EBOV Viral particles	Kerafast EMS703 090315	1/300	Green	PerkinElmer FP1487A 2380385	1/400	1
	CD68	Ms IgG1	Monocytes/ Macrophages	Dako M081401-2 20047711	1/50	Far red	PerkinElmer FP1497A 2491340	1/100	2
	Tissue Factor (CD142, TF9-10H10)	Ms IgG1	Extrinsic Coagulation pathway	ThermoFisher MA1-83495 TI2638538	1/50	Red	PerkinElmer FP1488A 2496488	1/200	3

Fluorescent *In Situ* Hybridization (FISH)

Fluorescent *In Situ* hybridization (FISH) was conducted following the RNAscope Multiplex FL v2 User Manual (Advanced Cell Diagnostics, Hayward, CA, USA). The same day as the FISH assay, 5 μM sections of FFPE liver tissue samples were cut and prepared to limit RNA degradation. Samples were deparaffinized and pretreated with hydrogen peroxide for 10 minutes to block endogenous peroxidase activity, followed by heat-mediated target retrieval using a steamer set to 100° C for 15 minutes. This was followed by RNAscope Protease Plus incubation in the ACD Hybez II Oven for 30 minutes. The target probes were then applied to the samples for hybridization with a two-hour incubation in the oven followed by signal amplification and probe visualization (Table 5). A positive control probe was included to confirm integrity of sample RNA and a negative control probe was included to confirm specificity of staining. The positive control probe was a marker known to stain the housekeeping gene *Vegfa* in macaque tissue (Advanced Cell Diagnostics, Cat # 487211, Lot # 18143A) and the negative control probe was for the non-specific bacterial gene *DapB* of *Bacilus subtilis* (Advanced Cell Diagnostics, Cat. # 310043, Lot # 17264A).

Table 6. FISH target probes and visualization.

	Probe	*mRNA marker*	Manufacturer, Catalog # and Lot #	**HRP-conjugated Fluorochrome**	Manufacturer, Catalog # and Lot #	Conc.
C1	**Mmu-*ISG1501***	**Interferon-stimulated gene 15**	Advanced Cell Diagnostics 540521 18136A	Far red (Opal 690)	PerkinElmer FP1497A 2491340	**1/750**
C2	**Hs-*IL6*-C2**	**Interleukin 6**	Advanced Cell Diagnostics 310371-C2 18270A	Red (Opal 570)	PerkinElmer FP1488A 2496488	**1/750**
C3	**V-Ebola-*VP35*-C3**	**EBOV Viral Protein VP35**	Advanced Cell Diagnostics 451691-C3 18116B	Green (Opal 520)	PerkinElmer FP1487A 2380385	**1/750**

Whole Slide Scanning and Digital Image Analysis for mIHC & FISH

All mIHC and FISH slides were digitized at 200x via fluorescent multispectral imaging with the Vectra Polaris Automated Quantitative Pathology Imaging System (Akoya Biosciences), equipped with an LED light source and monochrome camera. Acquisition parameters are outlined in Table 6. Terminal animal tissue samples were used to optimize exposures for each assay, via auto-exposure on a region of interest (ROI) and scanning to ensure parameters were correct. Then remaining slides for that assay were batch loaded and digitized, with parameters selected using the auto-exposure and auto-focus features on an ROI of the slide, and correction for any slide parameters outside of the range set based on terminal animals (no more than 3X channel exposure for terminal animals, except for green channel < 30 ms; Table 7).

Table 7. Optimized WSI scanning exposures.

Condition	Exposure Range
mIHC-1	
DAPI	2 – 5 ms
Opal 570	25 – 75 ms
Opal 690	30 – 90 ms
Opal 520	5 – 30 ms
mIHC-2	
DAPI	2 – 5 ms
Opal 570	25 – 75 ms
Opal 690	30 – 90 ms
Opal 520	5 – 30 ms
FISH (less variable)	
DAPI	2 – 5 ms
Opal 570	*50 – 75 ms*
Opal 690	*25 – 40 ms*
Opal 520	3 – 7 ms

Digitized whole slides were analyzed using image analysis software (HALO™, Indica Labs, Inc., Corrales, NM). Slides were first manually annotated to remove tissue artifacts (i.e. folds, air bubbles, fluorescent precipitate, etc.) and to select the tissue ROI(s) for digital analysis (Figure 2). Histogram threshold values were modified in viewer settings to minimize background signal and improve visibility of biomarkers within the real-time tuning window. For mIHC slides, quantitative outputs were derived from the Area Quantification FL (AQ) and High-Plex FL (HP) modules. For tissue ROI(s) included for analysis, Area Quantification FL reports total area positivity as a percentage and total tissue area (μm^2) for up to three fluorescent dyes used, as well as total area and percent positivity for 2 or more dyes (merged or overlapping dyes). High-Plex FL outputs include the absolute number of cells as well as cellular phenotyping for

cells expressing two or more fluorescent dyes within a defined cellular compartment. For both modules, minimum dye intensity thresholds were established for dye detection (Figure 1A). In order to accurately detect cells within tissue samples, in addition to dye thresholds, HP requires setting of nucleus, membrane and cytoplasm detection thresholds and ranges (Figure 1B-D).

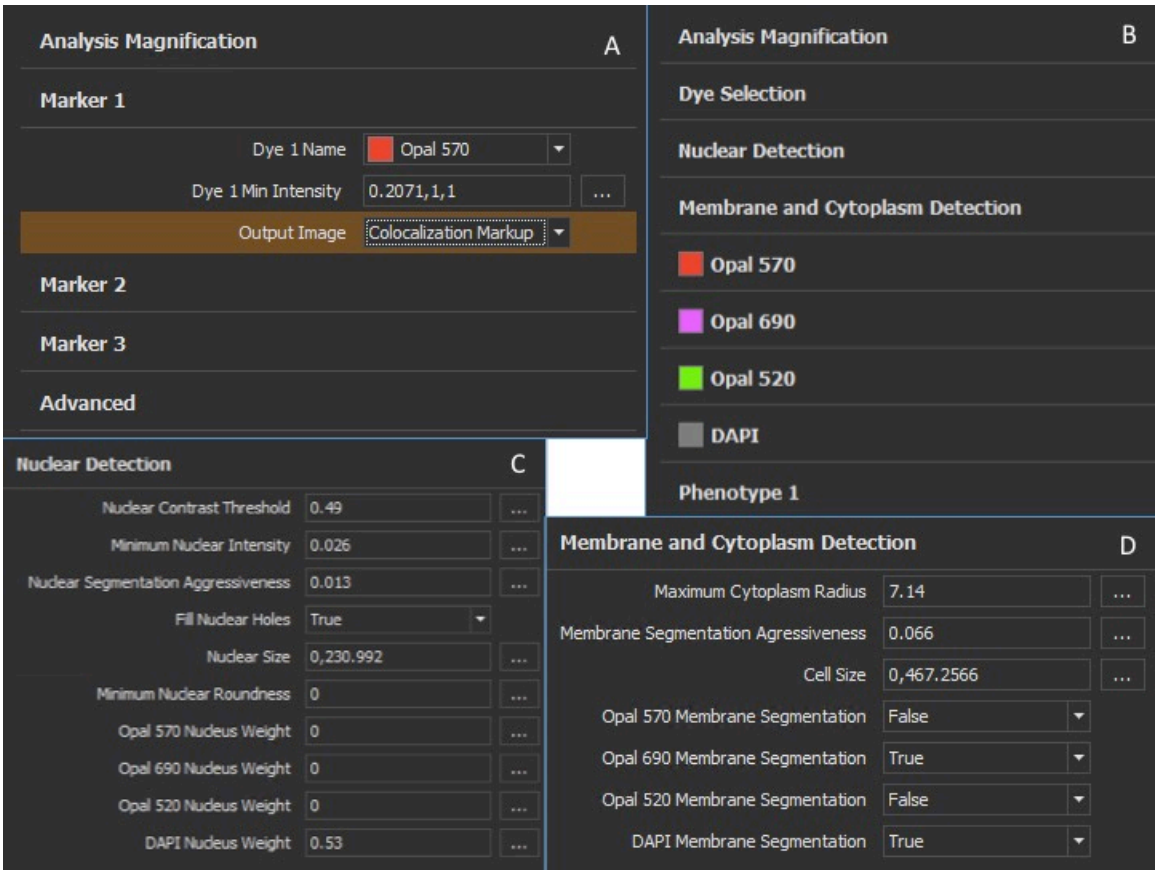

Figure 1: Halo™ Area Quantification FL and High-Plex FL Module parameters.
(A) AQ parameters to set for each dye (marker)
(B) All HP parameters, (C) HP Nucleus Detection parameters (D) HP Membrane and Cytoplasm Detection parameters

Module parameters were set for AQ and HP using real-time tuning, field of view and whole slide analysis, which were done at 1.5 magnification. For both modules, thresholds were set for minimal intensity for each fluorescence dye using terminal animals and real-time tuning of an ROI with targeted differential staining visualized. Then terminal settings were loaded and parameters were refined for each individual slide from earlier time points based on knowledge of anatomical specificity of liver biomarkers. For AQ, WSIs, with annotations to remove artifacts, were analyzed. For HP, given difficulties encountered in applying the HP Module for WSI analysis, a 10x field of view was analyzed on each slide to quantify number of cells per μm^2.

After running modules with initial annotations and thresholds, adjustments were made based on preliminary whole slide output images. To minimize variation across conditions for mIHC, cell detection and dye threshold parameters were set for the HP module using condition 1 and then these settings were imported, once finalized, for condition 2 analyses. Threshold parameters were then refined further using real-time tuning, if not already at the most accurate value to maximize specificity and sensitivity of the algorithm. Dr. Crossland, given his expertise as a trained veterinary pathologist, assisted with setting appropriate and accurate parameters for all modules and reviewed final annotations, parameters, modules, and resulting analyses. This iterative process of running, re-tuning, validating, and confirming modules before finalizing results was undertaken with the goal of improving reliability and accuracy of subsequent data analysis.

Digital whole slide images (WSI) and associated annotations and analyses, with

their threshold and detection parameters, were uploaded to Dr. Crossland's BU SCC laboratory storage and can be accessed upon request.

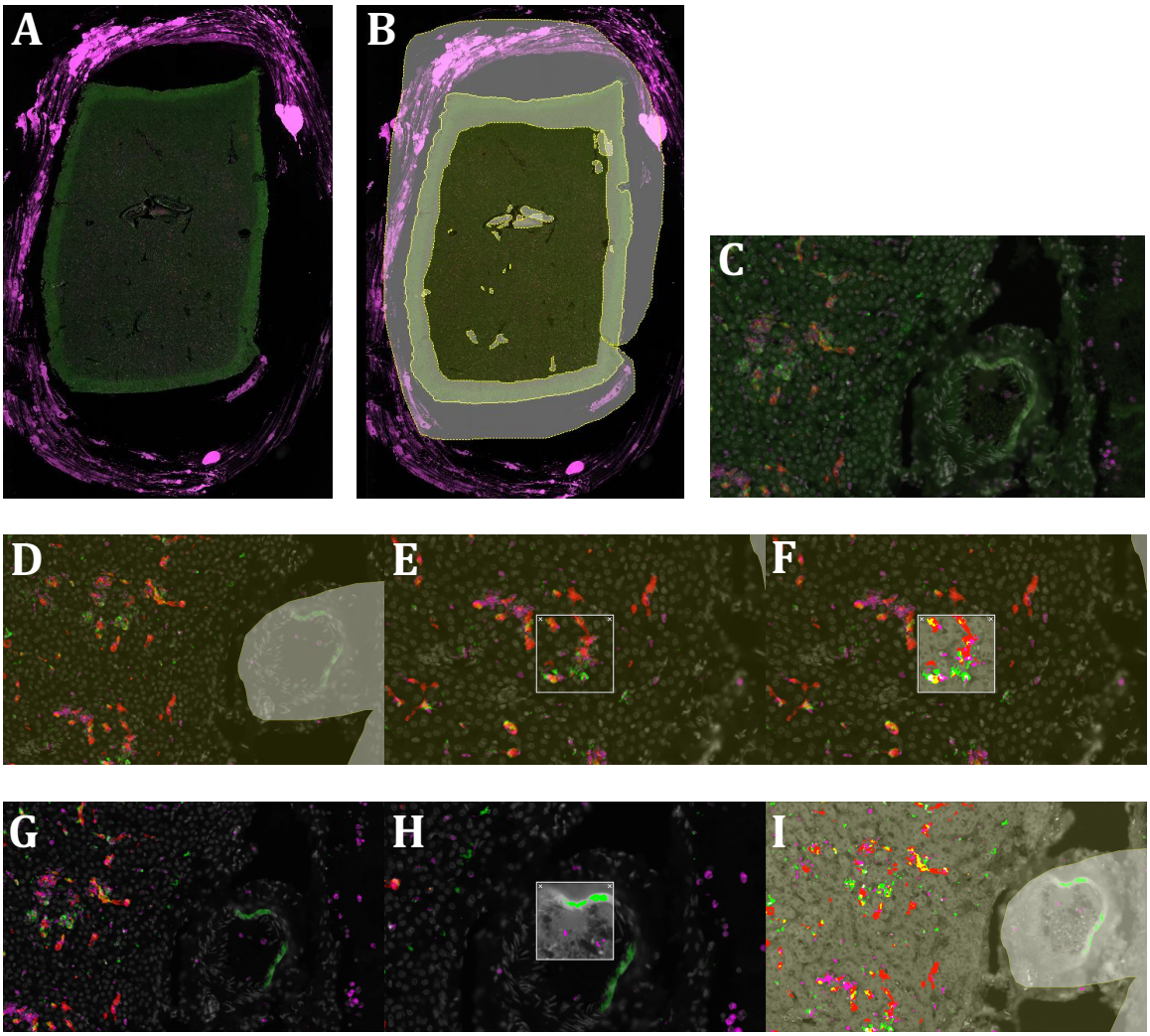

Figure 2: Halo™ Digital Image Analysis workflow.
(A) Imported whole slide image (WSI) scan in Halo™, (B) Annotated whole slide scan with artifacts removed from region(s) of interest (ROI) that will be included in area for analysis, (C) 20x Field of view, unadjusted stained slide (D) Alteration of black and white balance and channel intensity to reduce background noise and increase sensitivity for analysis at selected thresholds, (E) Real-time tuning window for the Halo™ Area Quantification (AQ) FL module, (F) Real-timing tuning analysis mark-up, (G) Unannotated 20x field of view with false positive staining, (H) Real-time tuning mark-up shows analysis of false-positive without annotation, (I) Field of view AQ mark-up with

annotation to remove false-positive from ROI for analysis, colocalization indicated by change in color in areas of 2+ channel overlap

Statistical Analysis for mIHC and FISH

One-way analysis of variance (ANOVA) was used, given that mIHC and FISH results were quantitative and parametric, to determine if statistical significance existed for host and viral biomarker expression. One-way ANOVA was performed on percent area reactivity/hybridization for each biomarker to account for variations in tissue sample size. One-way ANOVA was also conducted on changes in percent of cells positive for certain markers over time per given area. Values were compared for each measure within and across all groups (control, DPE groups, and terminal) with post-hoc Tukey correction for multiple comparisons. Measurements were then compared for colocalization of markers percent area over time using these same tests. Changes were compared in different markers over time to one another to assess whether they were correlated using Pearson's correlation coefficient (r). Quantitative results were also compared to ordinal histopathology scores using correlation coefficients to see if histopathological, immunohistochemical and *In Situ* hybridization findings were related. Simple linear regression was conducted of various parameters on ordinal scores and percent area VP35 immunoreactivity. Both linear regression and correlation coefficients were used because of the ordinal nature of the data, to provide comparison in case of overfitting of data via simple linear regression since logistic regression is not available in GraphPad Prism™ 8. For all statistical analysis, P-values < 0.05 were considered statistically significant.

RESULTS

Qualitative Histopathology

The first distinct histomorphological feature attributed to EBOV disease was observed **3 DPE** in one animal, which exhibited mild sinusoidal expansion by histiocytes (inflammation-1; Figure 3A) and rare histiocytic cytoplasmic viral inclusions (Figure 4A). At **4 DPE**, one animal exhibited histiocytic cytoplasmic viral inclusions, but displayed no evident inflammation or fibrin deposition, while the two remaining animals both exhibited mild sinusoidal expansion by histiocytes (inflammation-1), rare sinusoidal fibrin thrombi (fibrin-1; Figure 4D), and histiocytic cytoplasmic viral inclusions. By **5 DPE**, all animals exhibited minimal-to-mild multifocal hepatocellular necrosis (necrosis-1 or 2; Figures 5B and C), rare to occasional sinusoidal fibrin thrombi (fibrin-1 or 2; Figure 4D and E), moderate expansion of sinusoids by histiocytes and neutrophils (inflammation-2; Figure 3B), and an increased frequency of cytoplasmic viral inclusions, which for the first time included both histiocytes and hepatocytes (Figure 4A and B).

At **6 DPE**, 2 of 3 animals displayed moderate hepatocellular necrosis (necrosis-2), with the remaining animal having mild hepatocellular necrosis. All 3 animals displayed moderate sinusoidal expansion by histiocytes and multifocal fibrin thrombi (inflammation-2, fibrin-2). At **terminal** time points, 5 of 6 animals displayed occasional sinusoidal fibrin thrombi (fibrin-2), with one animal displaying rare fibrin thrombi (fibrin-1). 4 animals had moderate expansion of sinusoids by histiocytes (inflammation-2), while the remaining two animals had either severe inflammation consisting of

neutrophils and histiocytes (inflammation-3; Figure 3C), or rare sinusoidal aggregates of histiocytes (inflammation-1). Four of six terminal animals exhibited moderate hepatocellular necrosis (necrosis-2), while the remaining two animals had either severe hepatocellular loss (necrosis-3; Figure 5D) or rare scattered individual hepatocellular necrosis (necrosis-1; same animal with inflammation-1).

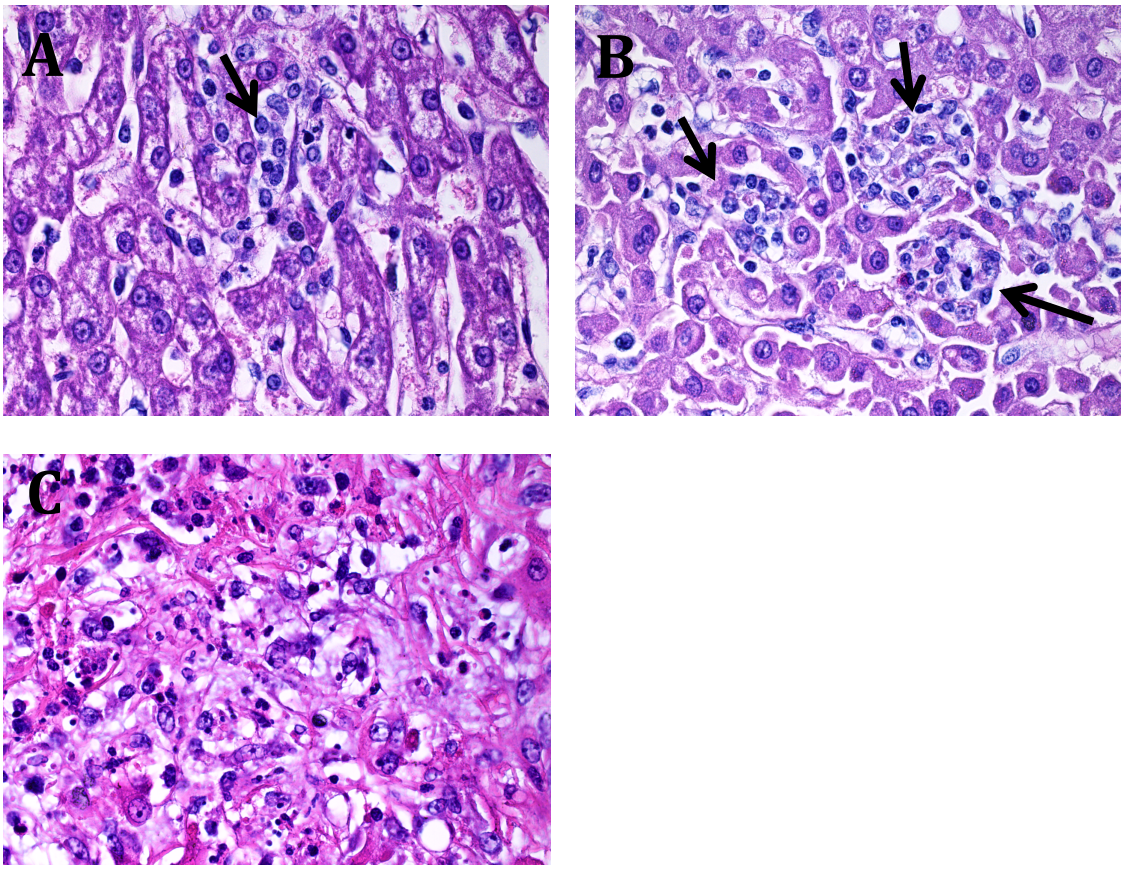

Figure 3: Progression of inflammation in liver of EBOV-infected Rhesus Macaques. (A) 1 - Rare, increased numbers of histiocytes and neutrophils within sinusoids, 3 DPE, (B) 2 - Expansion of sinusoidal spaces by aggregates of >5 histiocytes, 5 DPE, (C) 3 - Presence of large foci of histiocytes and neutrophils within an area of hepatocellular loss and karyorrhectic debris, terminal animal. *Images A-C stained with H&E, magnification 600x with oil immersion*.

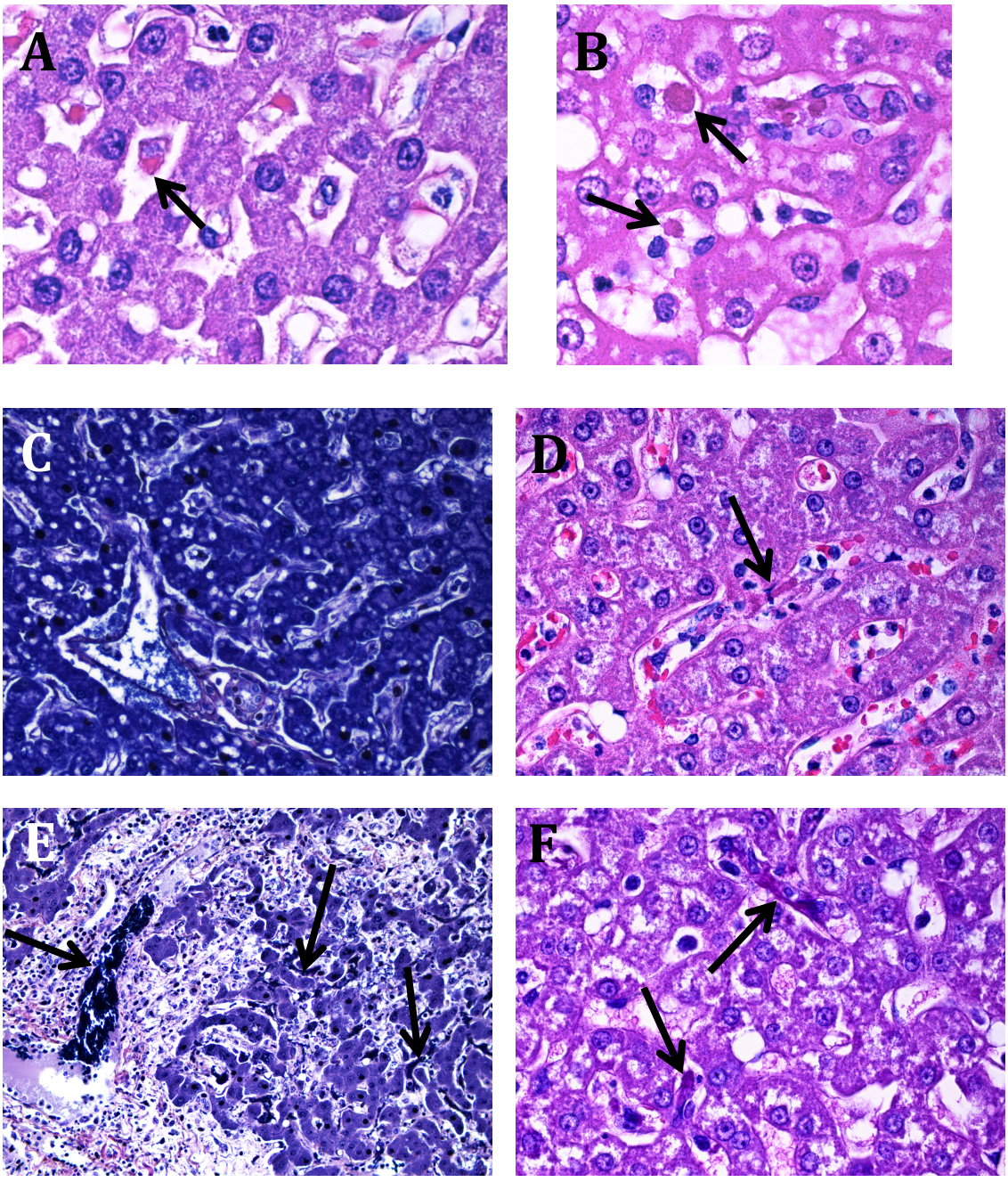

Figure 4: Viral inclusions and fibrin thrombi in liver of EBOV-infected Rhesus Macaques.
(A) Cytoplasmic histiocytic viral inclusion, 3 DPE, (B) Hepatocellular cytoplasmic viral inclusions, 5 DPE, (C) 0 – Non-infected control animal stained with PTAH, no sinusoidal fibrin deposition visible, (D) 1 – Rare, multifocal occlusion of sinusoids by fibrin

thrombi, 4 DPE, (E) PTAH stain illustrating sinusoidal and venous fibrin thrombi, terminal animal, (F) Multiple sinusoidal fibrin thrombi, 6 DPE. *Images A, B, D, & F stained with H&E, magnification 600x with oil immersion. Images C & E stained with PTAH, magnification 400x and 200x, respectively.*

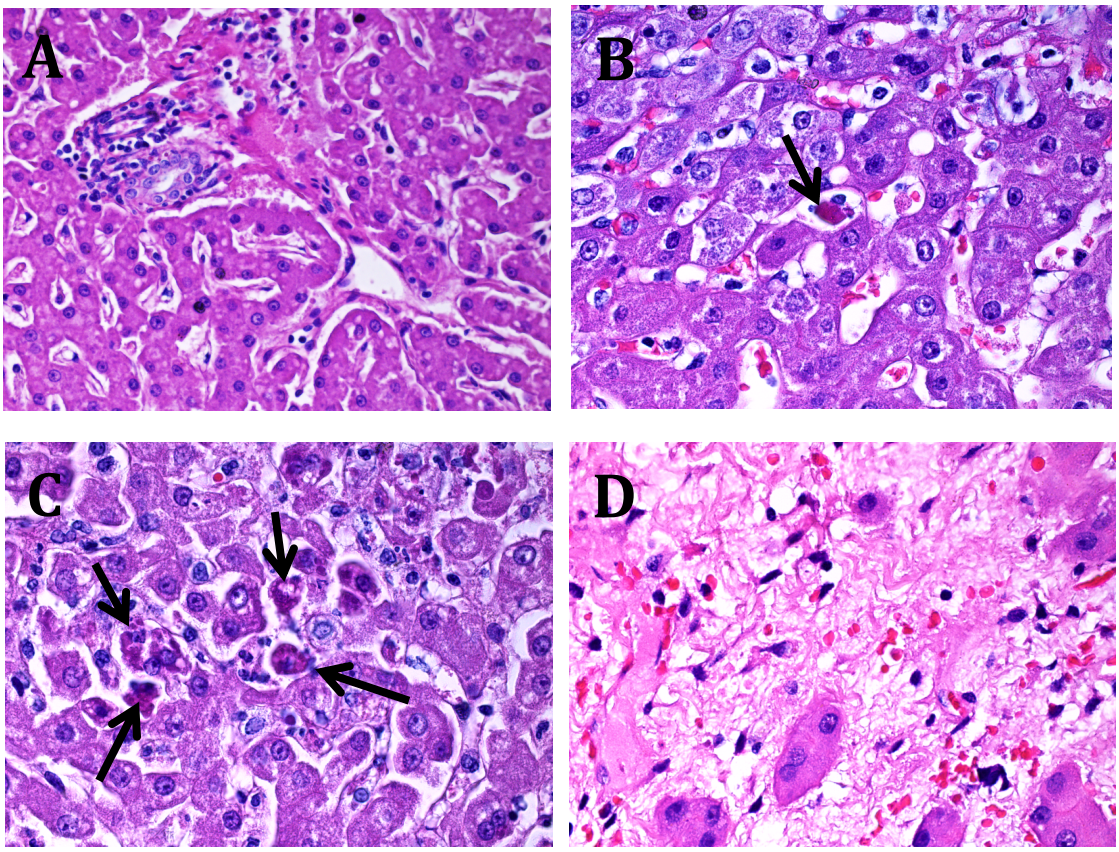

Figure 5: Progression of necrosis in liver of EBOV-infected Rhesus Macaques. (A) 0 - Non-infected control animal with normal hepatic architecture, (B) 1 - Rare single cell hepatocellular necrosis, 5 DPE, (C) 2 - Multifocal neighboring hepatocellular necrosis, 5 DPE, (D) 3 - Coalescing area of hepatocellular loss, terminal. *Images A-D stained with Hematoxylin & Eosin (H&E). Magnification A, 400x; B-D, 600x with oil immersion.*

Ordinal Histopathology Scoring

Severity of necrosis, inflammation, fibrin deposition and overall cumulative histopathology scores were statistically significant among control and 3 DPE animals compared to terminal animals. Additional statistical significance was observed between necrosis in 4DPE and terminal animals; and fibrin deposition between 5 and 6 DPE animals compared to control and 3 DPE animals. Preliminary findings from H&E analysis informed separation of animals into **peracute** (3-4 DPE with a Cumulative Score < 4) and **acute** (5-6 DPE with a Cumulative Score > 4) as well as **terminal** (6-8 DPE) groups. These groups were defined based on observation of changes in histopathology relative to control animals that were mild versus moderate to severe in the liver of EBOV-infected rhesus macaques.

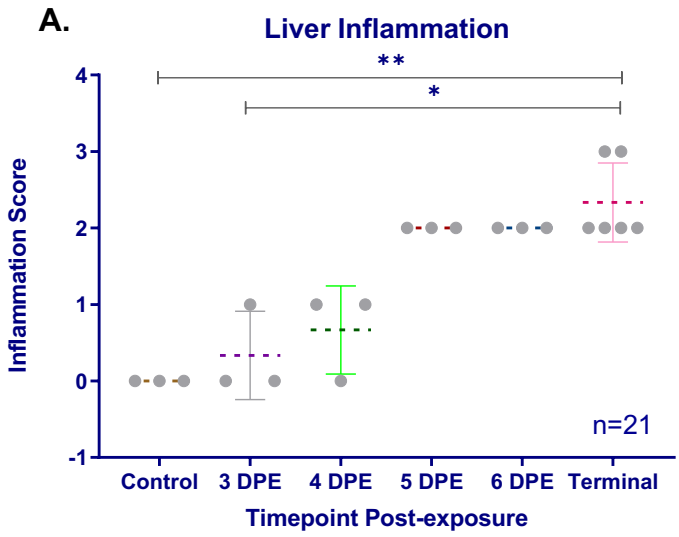

B.

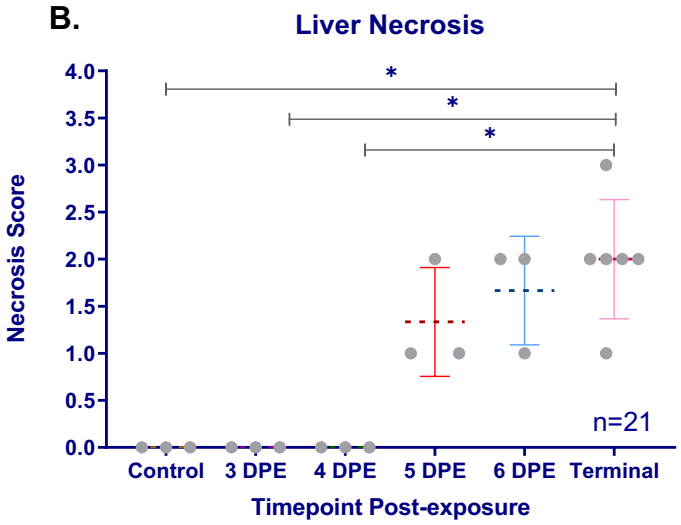
Liver Necrosis
Necrosis Score
4.0
3.5
3.0
2.5
2.0
1.5
1.0
0.5
0.0
*
*
*
n=21
Control
3 DPE
4 DPE
5 DPE
6 DPE
Terminal
Timepoint Post-exposure

C.

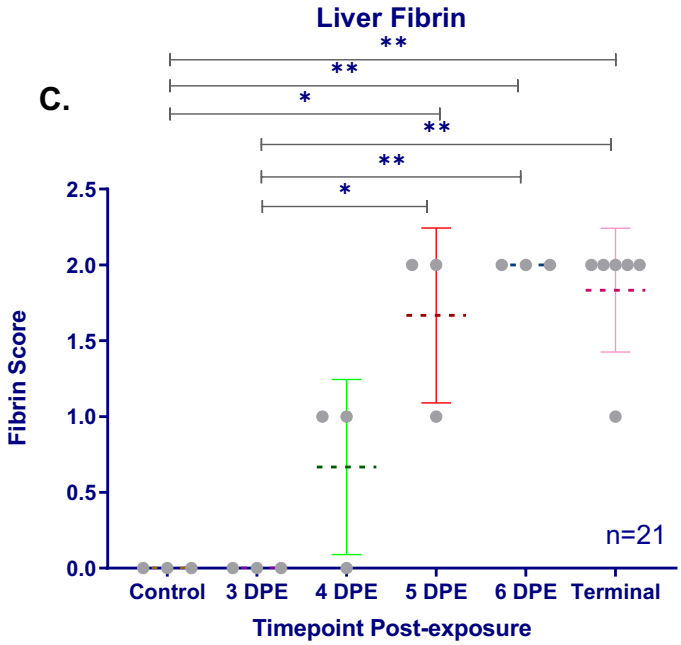
Liver Fibrin
Fibrin Score
2.5
2.0
1.5
1.0
0.5
0.0
**
**
*
**
**
*
n=21
Control
3 DPE
4 DPE
5 DPE
6 DPE
Terminal
Timepoint Post-exposure

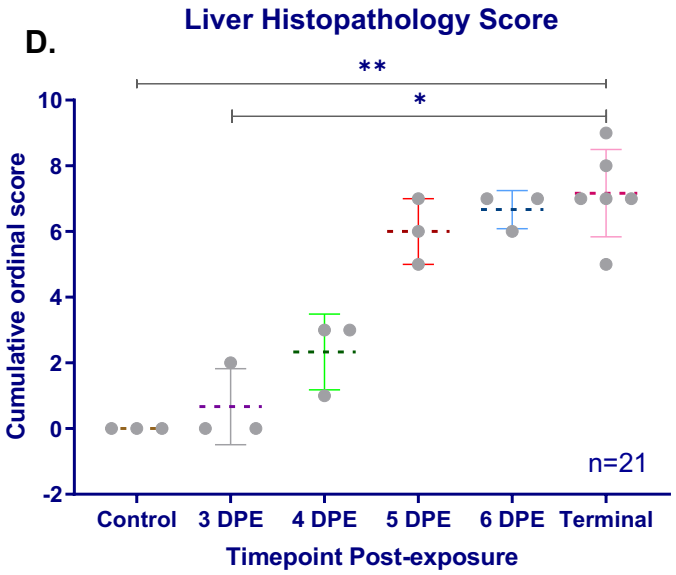

Figure 6: Semi-quantitative analysis of hepatic histopathology findings in EBOV-infected Rhesus Macaques.

(A) Inflammation, (B) Necrosis (C) Fibrin

(D) Cumulative liver score calculated as the sum of the former three parameters, plus 1 if viral inclusions were present

For all parameters, including overall score, there was a statistically significant difference across time points (P=0.0033; P=0.0042; P=0.0037; P=0.0045, Kruskal Wallis). Specifically, between individual time points, differences between control and terminal as well as 3 DPE and terminal groups were statistically significant ($P < .05$, Benjamin, Krieger and Yekutieli).

**For each time point, the dashed line represents the mean, bars represent the standard deviation, and individual plot points represent the value for the given parameter for each animal at that time- point.*

*ns = non-significant P-value, *P-value < 0.05, **P-value < 0.005, ***P-value < 0.0005, ****P-value < 0.00005.*

mIHC Digital Image Analysis

Independent Biomarker Immunoreactivity - Condition 1

Raw Image	Halo™ AQ Mark-up
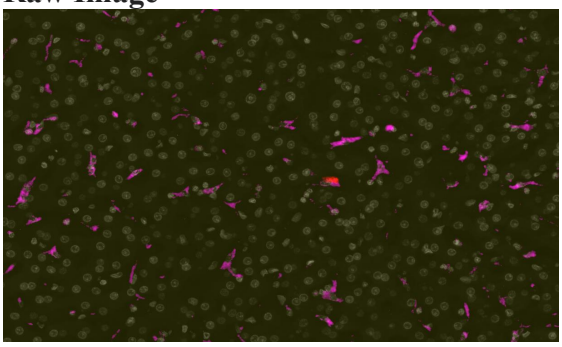	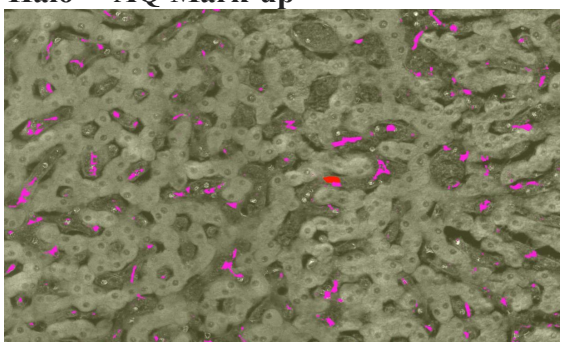
Control	
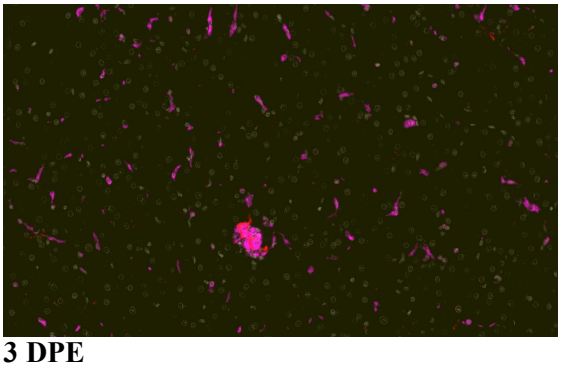	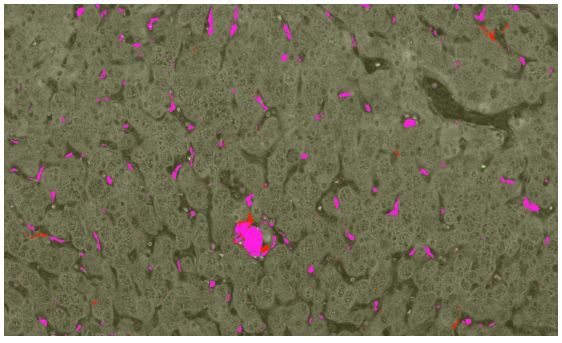
3 DPE	
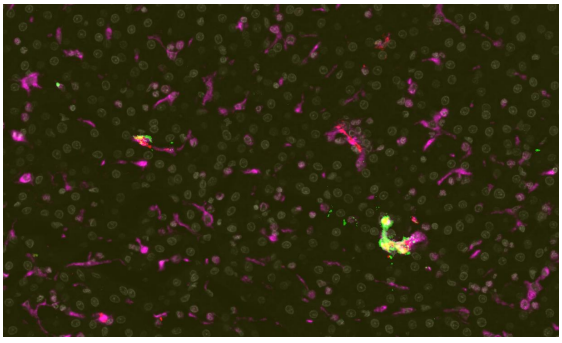	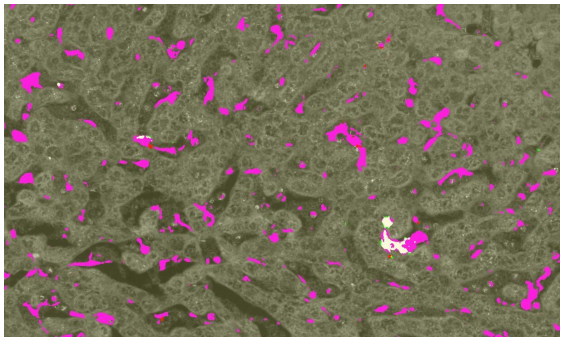
4 DPE	

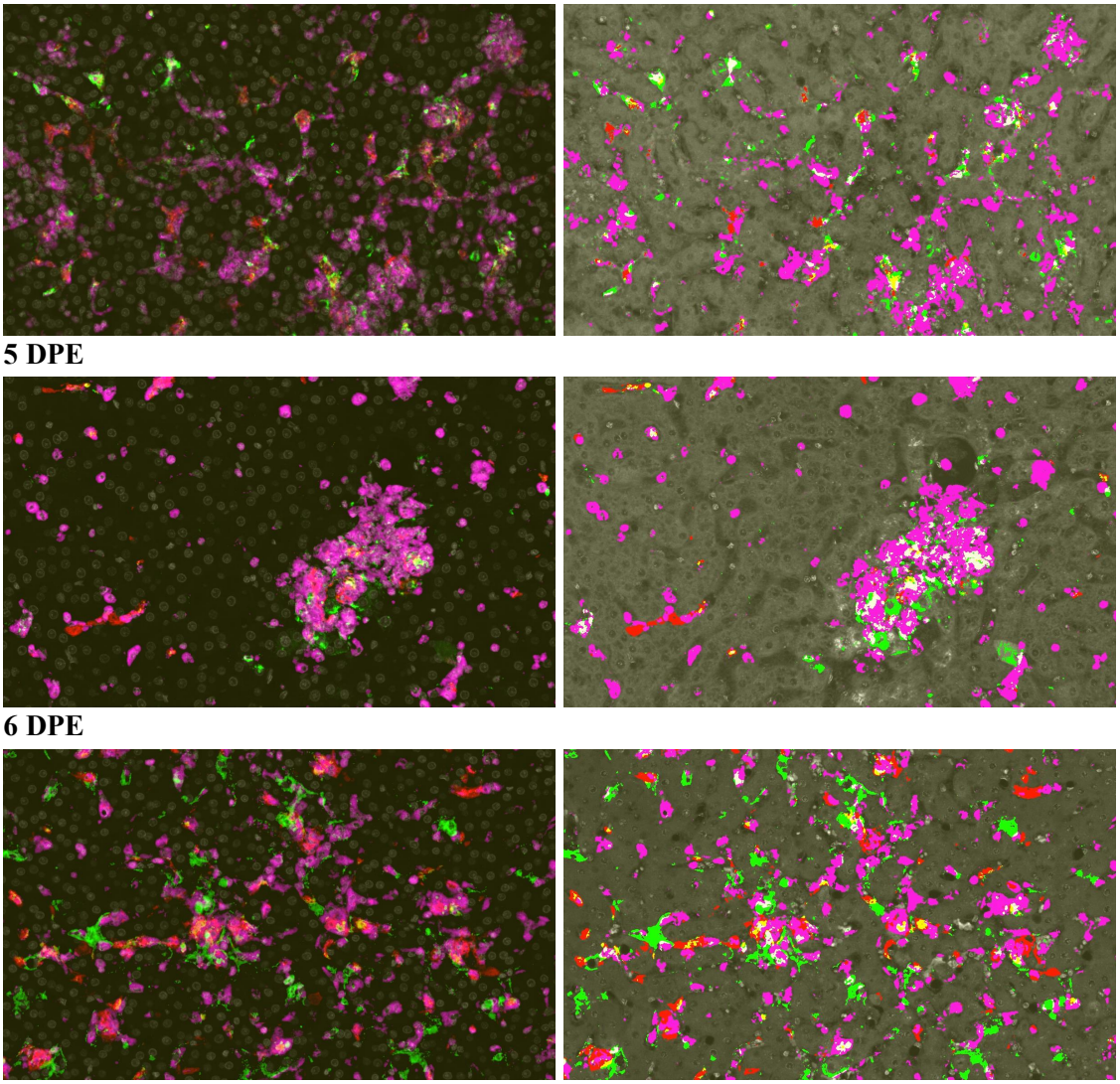

Figure 7: Changes over time in area of hepatic tissue immunoreactive for VP35 (Green), Tissue Factor (Red) and CD68 (Cyan).

EBOV VP35 percent immunoreactivity ranged from a minimum of 0.037% (controls excluded; 0%) at 3 DPE to a maximum of 2.94% in a terminal animal. Intergroup statistical significance for VP35 was observed for terminal animals across all time points except for 6 DPE, and between control, 3 DPE and 4 DPE animals relative to

6 DPE animals (Figure 8A). TF percent immunoreactivity ranged from a minimum of 0.0028% in a control animal and 0.0098% at 3 DPE to a maximum of 2.91% in a terminal animal. Statistical significance of terminal animals was observed when compared to all other groups ≤ 5 DPE (Figure 8B). CD68 percent immunoreactivity ranged from 1.43% in a control animal to 7.7% in a 6 DPE animal. Statistical significance of terminal and 6 DPE animals was observed when compared to all other groups ≤ 4 DPE (Figure 8C).

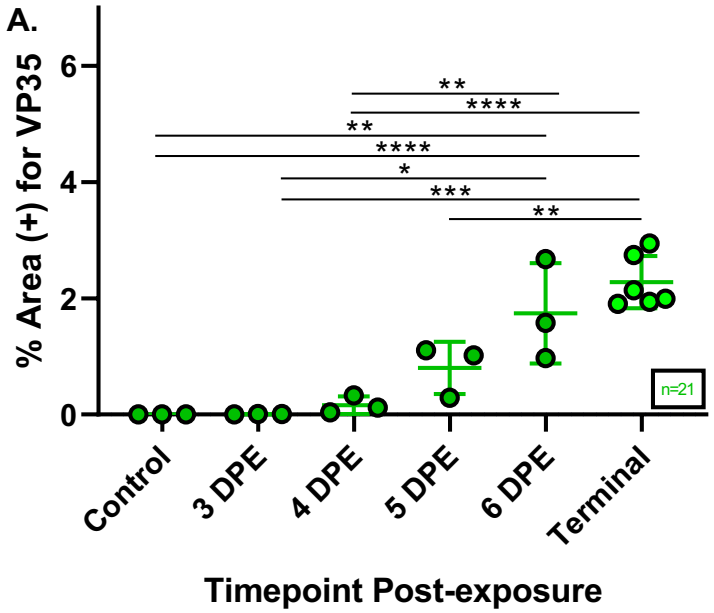

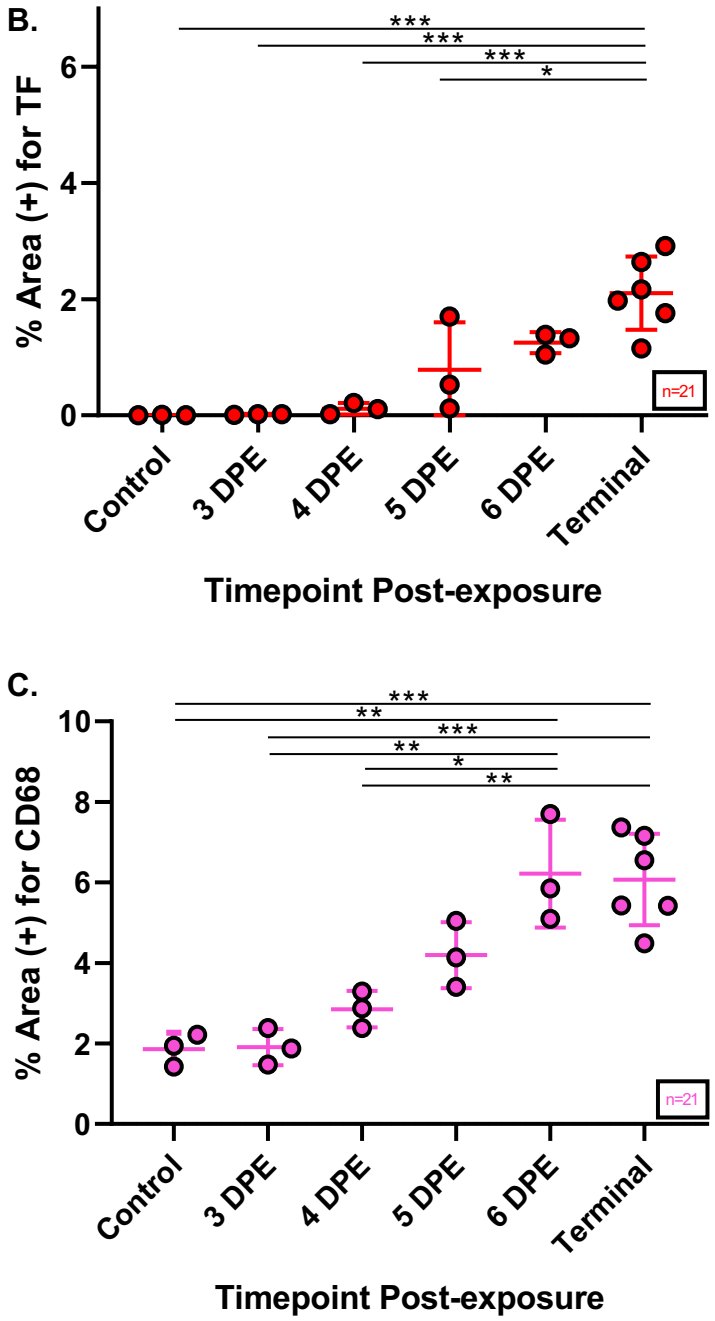

Figure 8: Temporal change in the total area % immunoreactivity of mIHC-1 viral and host biomarkers in the liver of Rhesus Macaques.
(A) VP35 Assay 1, (B) Tissue Factor (TF), (C) CD68
One-way ANOVA and post-hoc Tukey correction for multiple comparisons: P-value < 0.0001 for all analyses performed. Graphs indicate which groups showed statistically significant differences from one another for each marker.

Raw Image **Halo HP Mark-up**

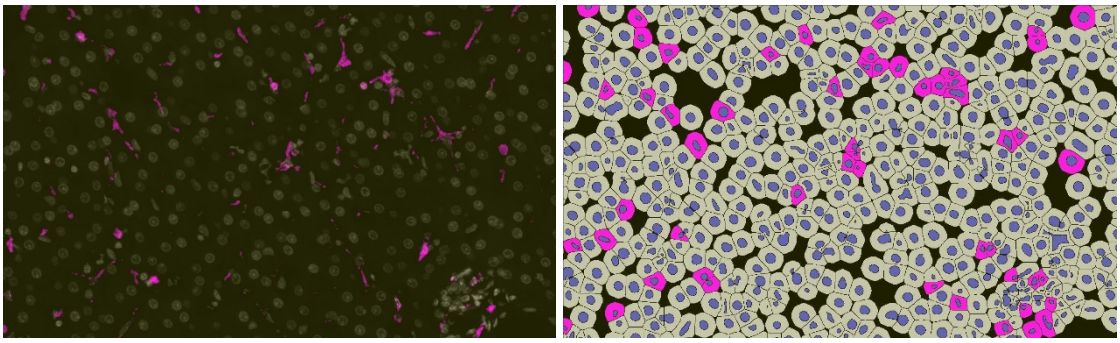

Control

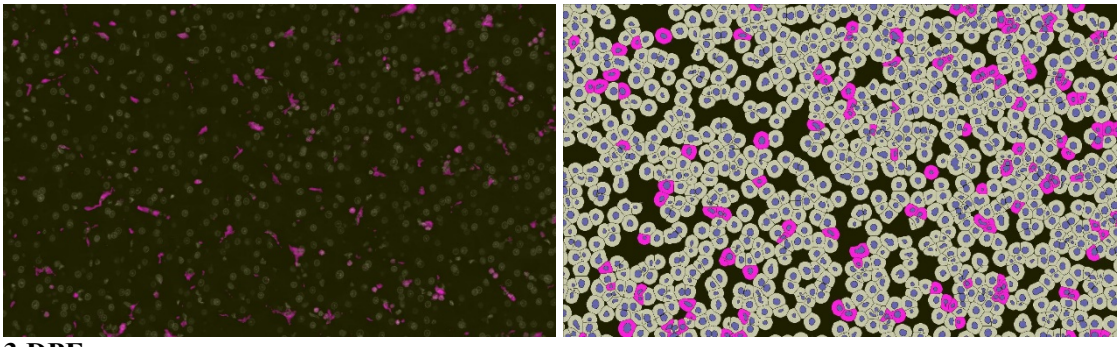

3 DPE

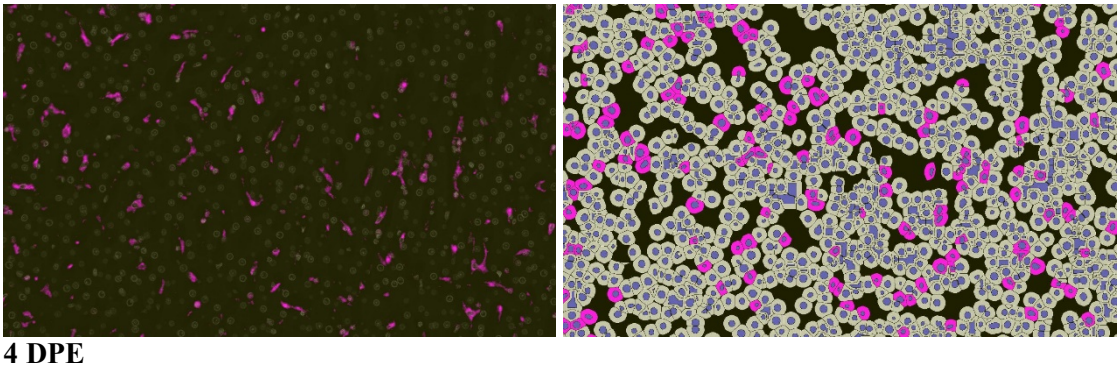

4 DPE

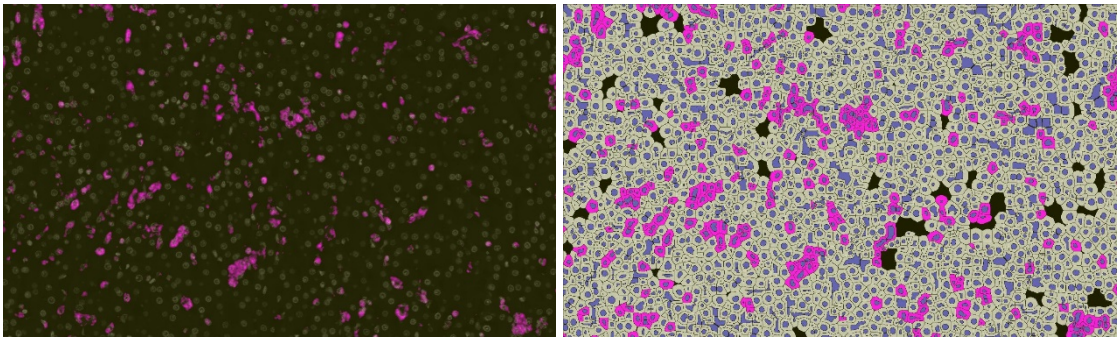

5 DPE

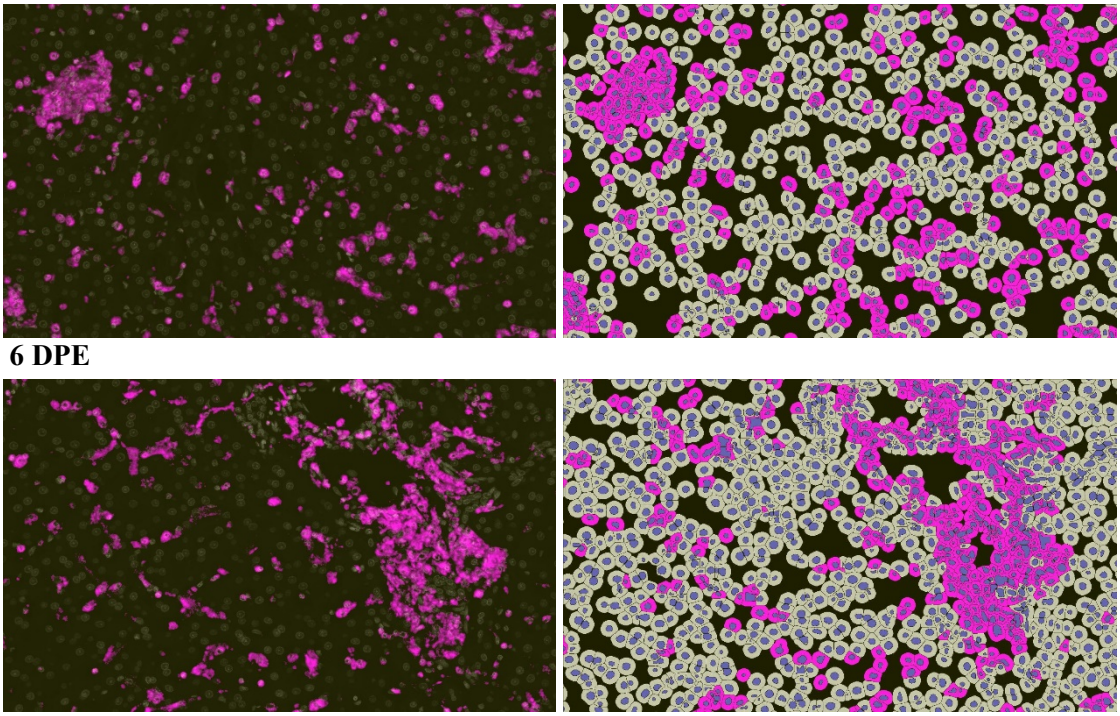

Figure 9: Changes over time in number of cells per μm² of hepatic tissue immunoreactive for CD68 (Macrophage marker).

Number of cells per μm² immunoreactive for CD68 ranged from 0.000278165 in a control animal to 0.001271192 in a 6 DPE animal. Statistical significance of terminal and 6 DPE animals was observed when compared to all other groups ≤ 4 DPE as well as for control-3 DPE animals relative to 5 DPE animals (Figure 10).

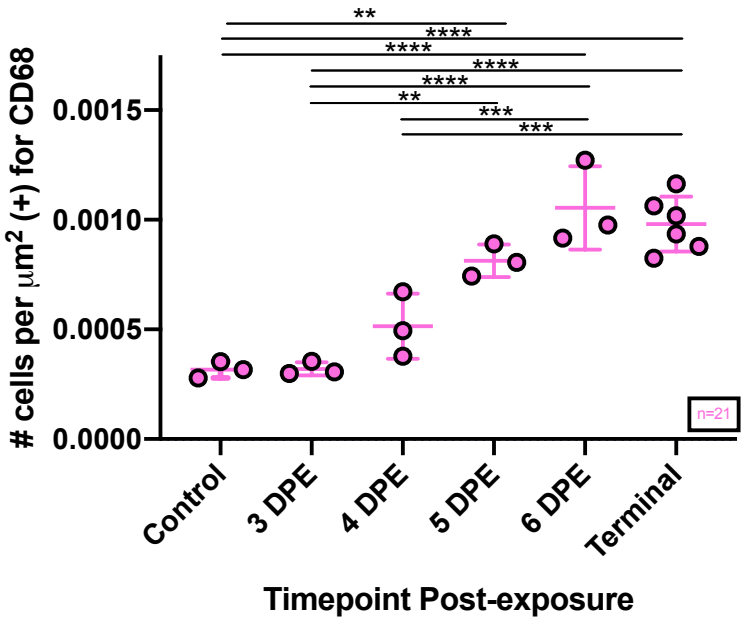

Figure 10: Temporal change in the number of cells per µm² immunoreactive for CD68.
One-way ANOVA and post-hoc Tukey correction for multiple comparisons: P-value < 0.0001.

The increases in area quantification for CD68 over time and TF over time were directly correlated with changes in immunoreactivity for VP35 (r = 0.93; r = 0.87) and increases in CD68 and TF were also strongly correlated to each other (r = 0.85). As expected, colocalization was strongly correlated with increased in individual biomarkers over time. Additionally, AQ and HP module results for CD68 were very highly correlated (r = 0.98).

Table 8. Correlation Matrix for mIHC-1.

	VP35	CD68	TF	CD68 & TF	CD68 & VP35	TF & VP35	CD68, TF & VP35
VP35	1.00	0.93	0.87	0.83	0.91	0.81	0.78
CD68	0.93	1.00	0.85	0.83	0.92	0.78	0.78
TF	0.87	0.85	1.00	0.97	0.75	0.83	0.80
CD68 & TF	0.83	0.83	0.97	1.00	0.73	0.78	0.80
CD68 & VP35	0.91	0.92	0.75	0.73	1.00	0.86	0.88
TF & VP35	0.81	0.78	0.83	0.78	0.86	1.00	0.97
CD68, TF & VP35	0.78	0.78	0.80	0.80	0.88	0.97	1.00

Colocalization of Biomarker Immunoreactivity - Condition 1

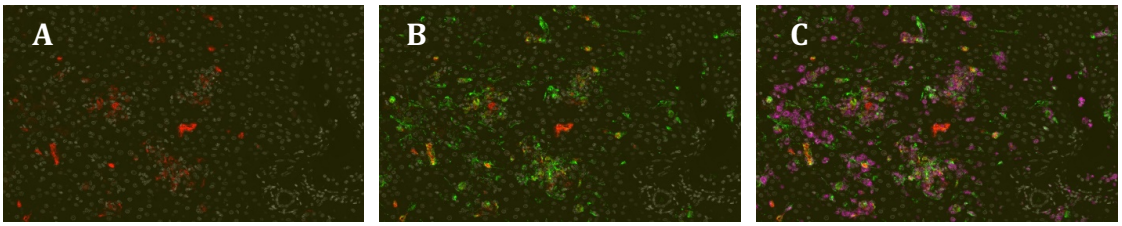

Figure 11: Colocalization of Tissue Factor, VP35 and CD68 at 6 DPE.
In the same ROI, the red channel, visualizing TF, the green channel, visualizing EBOV VP35, and the cyan channel visualizing CD68 can be viewed independently and together to observe where dyes merge.
(A) Red, (B) Red and green, (C) Red, green and cyan

Colocalization of CD68 and TF (Figure 12A), as well as VP35 and TF (Figure 12C), was statistically increased between **peracute** (3-4 DPE) and **terminal** (6-8 DPE) animals. Colocalization of CD68 and TF ranged from 0.0031% at in a control animal to 1.16% in a terminal animal and colocalization of VP35 and TF ranged from 0.0000019% at 3 DPE to 0.61% in a terminal animal. Colocalization of CD68 and VP35 (Figure 12B) ranged from 0.0011% at 3 DPE to 0.96% in a 6 DPE animal and also increased significantly from peracute (control-4 DPE) to acute (5-6 DPE) and terminal (6-8 DPE) time points in the course of infection. Colocalization of all three biomarkers included in mIHC-1 ranged from 0.0000015% at 3 DPE to 0.28% in a terminal animal and increased significantly as well from peracute time points (control-4 DPE) when compared to both 6 DPE and terminal animals (Figure 12D).

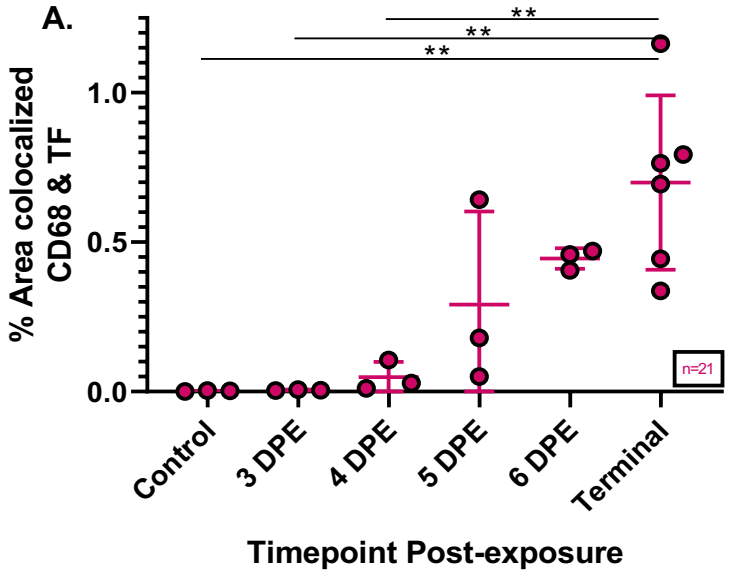

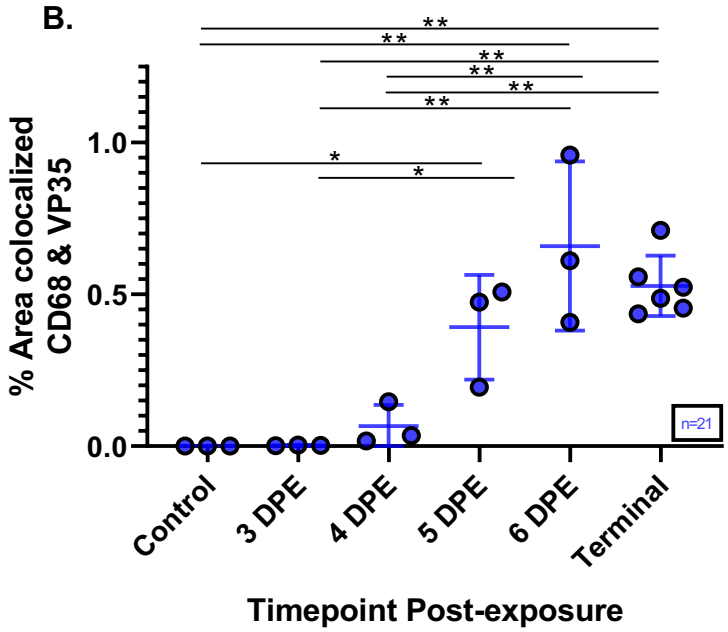
B.
% Area colocalized
CD68 & VP35
1.0
0.5
0.0
n=21
Control
3 DPE
4 DPE
5 DPE
6 DPE
Terminal
Timepoint Post-exposure

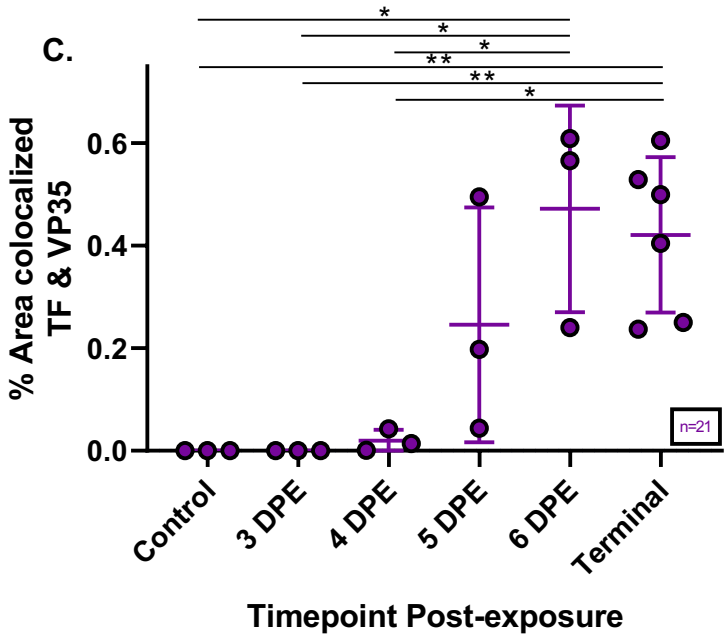
C.
% Area colocalized
TF & VP35
0.6
0.4
0.2
0.0
n=21
Control
3 DPE
4 DPE
5 DPE
6 DPE
Terminal
Timepoint Post-exposure

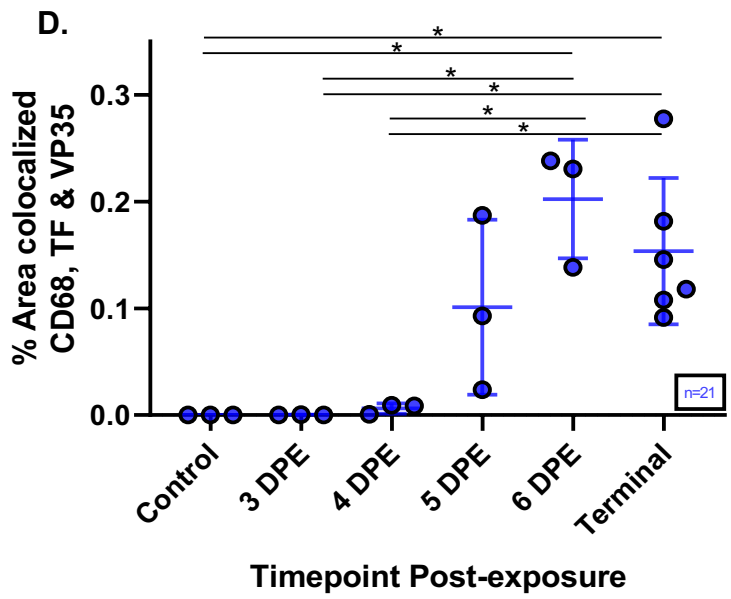

Figure 12: Temporal change in the colocalization of mIHC-1 viral and host biomarkers in the liver of Rhesus Macaques.
(A) CD68 and Tissue Factor (TF), (B) CD68 and VP35, (C) Tissue Factor and VP35, (D) CD68, TF and VP35
One-way ANOVA and post-hoc Tukey correction for multiple comparisons: (A) P-value = 0.006, (B) P-value < 0.0001, (C) P-value = 0.006, (D) P-value = 0.004

Independent Biomarker Immunoreactivity - Condition 2

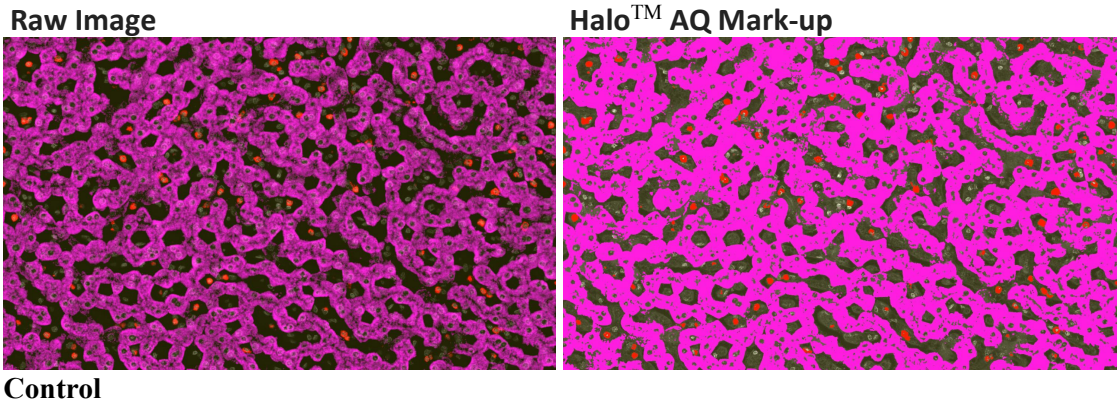

Control

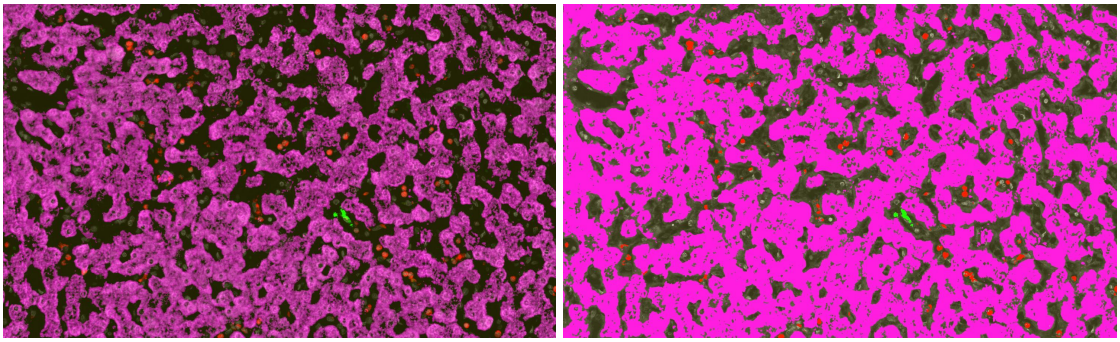

3 DPE

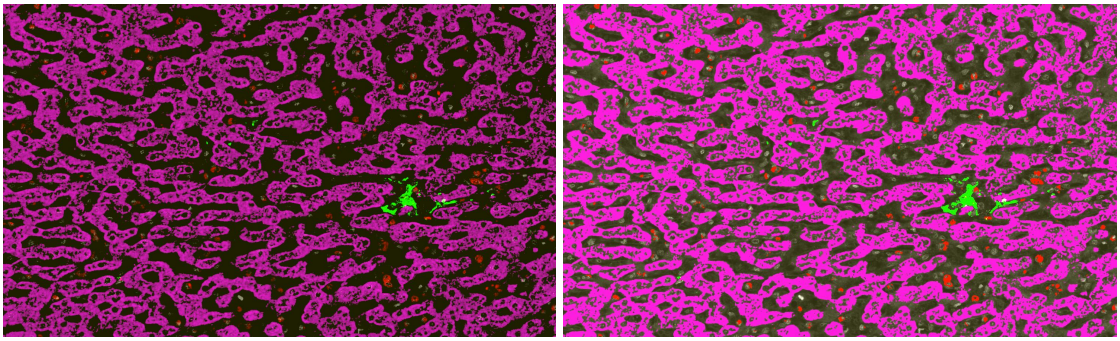

4 DPE

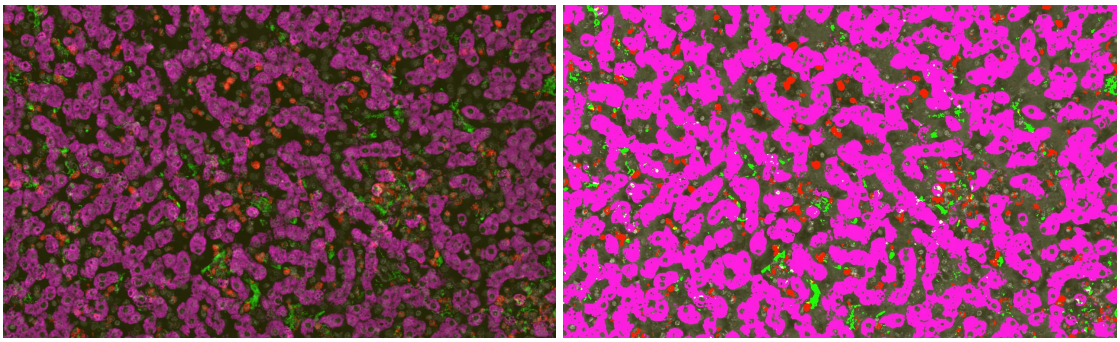

5 DPE

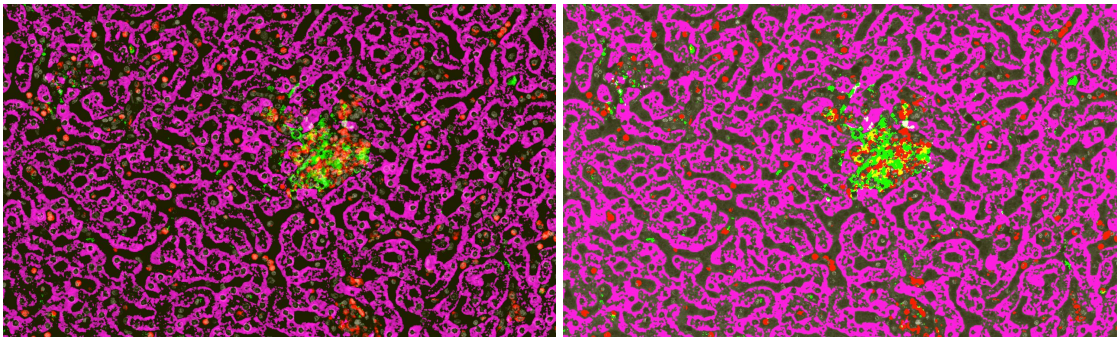

6 DPE

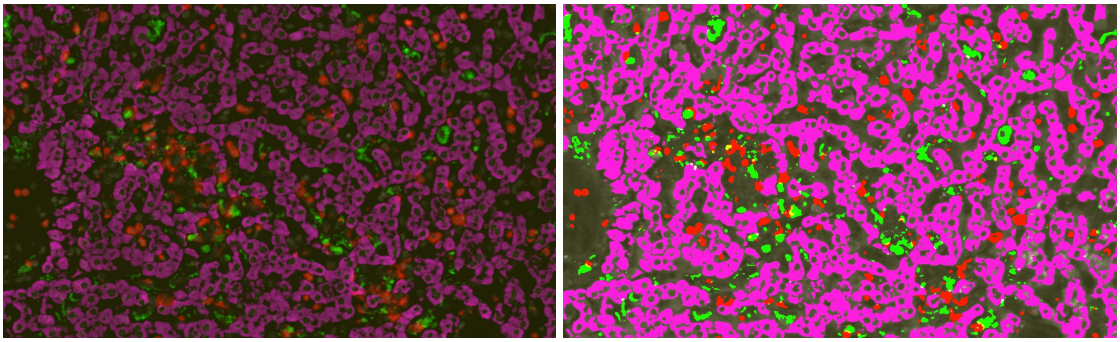

Terminal

Figure 13: Changes over time in area of hepatic tissue immunoreactive for VP35 (Green), Myeloperoxidease (Red) and Heppar (Cyan).

EBOV VP35 percent immunoreactivity ranged from a minimum of 0.0021% (controls excluded; 0%) at 3 DPE to a maximum of 3.01% in a terminal animal. As in mIHC-1, intergroup statistical significance for VP35 was observed across all time points except for 6 DPE relative to terminal animals and between control, 3 DPE and 4 DPE animals relative to 6 DPE animals (Figure 14A). Myeloperoxidase (MPO) percent immunoreactivity ranged from a minimum of 0.21% in a control animal to a maximum of 2.51% in a 6 DPE animal. Statistical significance of terminal and 6 DPE animals was observed when compared to all other groups ≤ 5 DPE and between control and 3 DPE animals relative to 5 DPE animals (Figure 14B). Heppar percent immunoreactivity ranged from 60.99% in a control animal to 40.07% in a terminal animal. Statistical significance was observed across all groups except for between 6 DPE and terminal animals (Figure 14C).

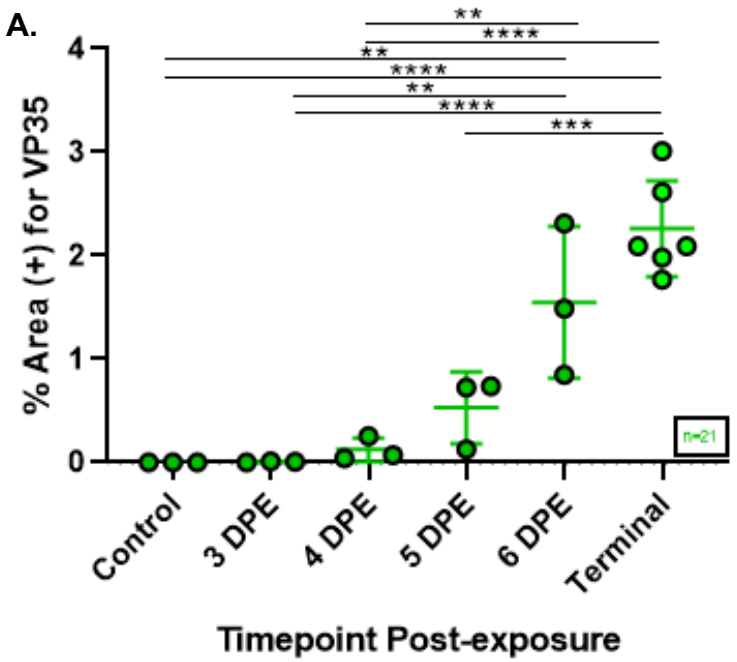
A.
% Area (+) for VP35
0
1
2
3
4
**
****
**
****
**
****
***
n=21
Control
3 DPE
4 DPE
5 DPE
6 DPE
Terminal
Timepoint Post-exposure

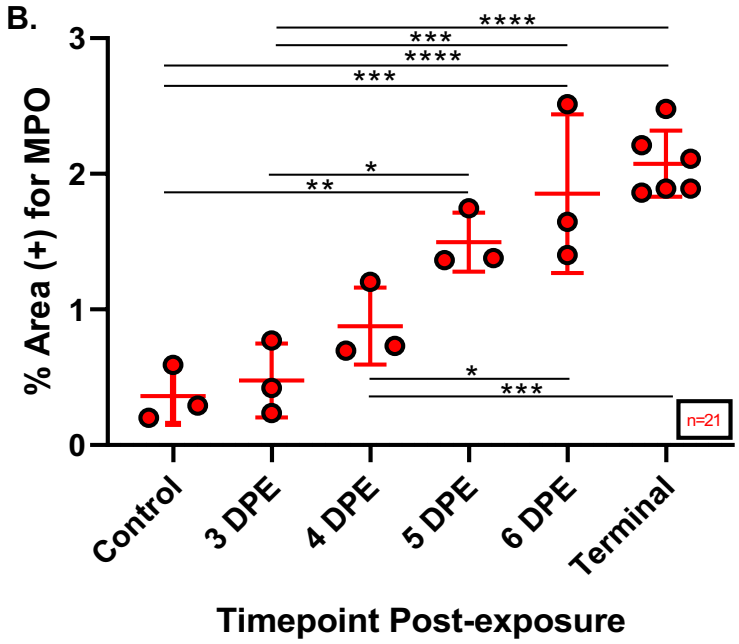
B.
% Area (+) for MPO
0
1
2
3
****
***
****
***
*
**
*
***
n=21
Control
3 DPE
4 DPE
5 DPE
6 DPE
Terminal
Timepoint Post-exposure

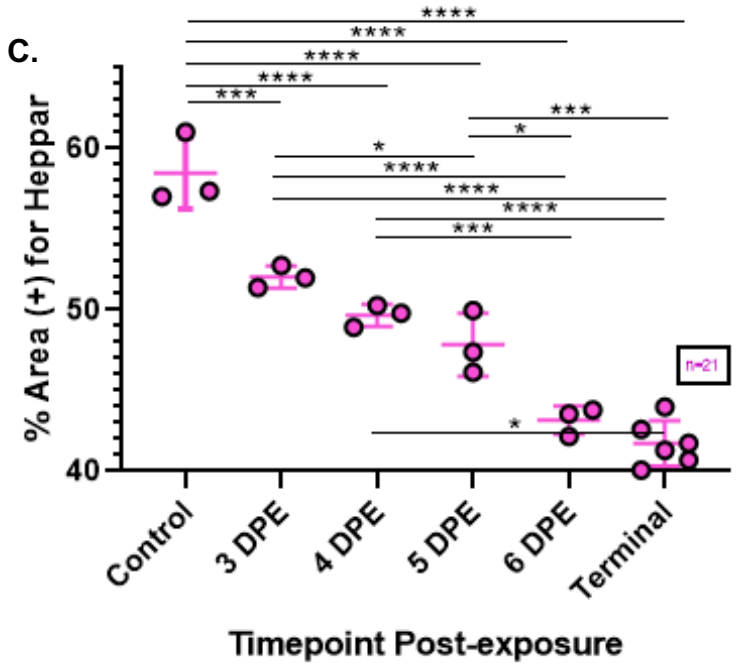

Figure 14: Temporal changes in the total area % immunoreactivity of mIHC-2 viral and host biomarkers in the liver of Rhesus Macaques.
(A) VP35 Assay 2, (B) Myeloperoxidase (MPO), (C) Heppar
One-way ANOVA and post-hoc Tukey correction for multiple comparisons: P-value < 0.0001 for all analyses performed.

Raw Image **Halo HP Mark-up**

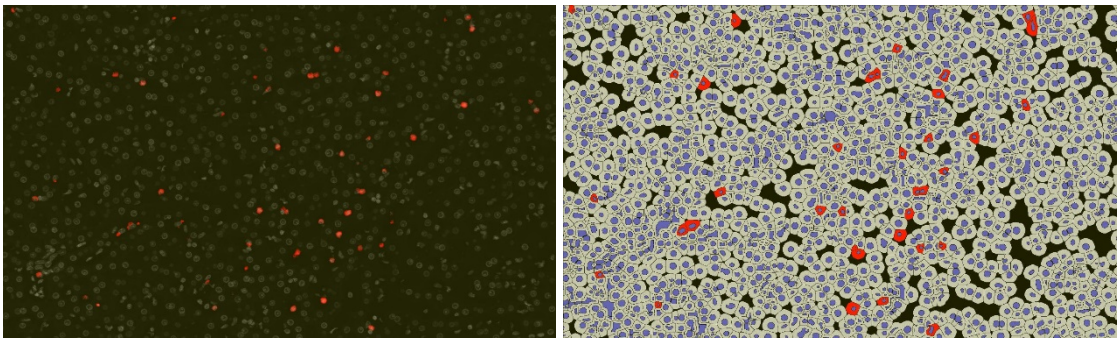

Control

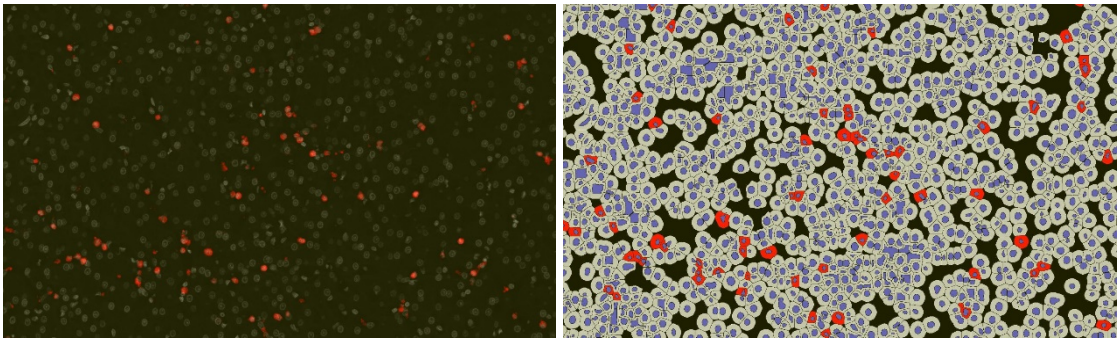

3 DPE

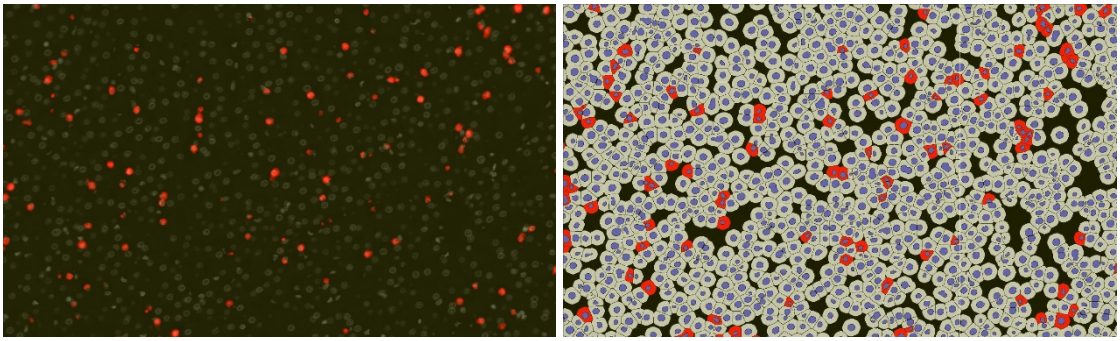

4 DPE

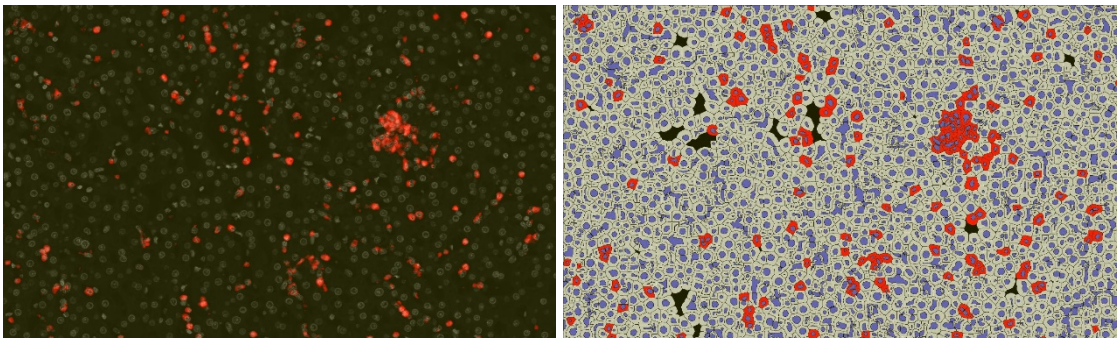

5 DPE

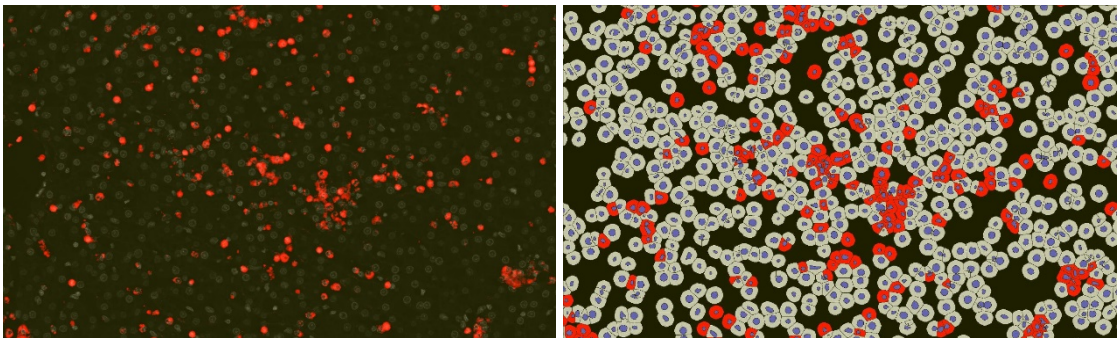

6 DPE

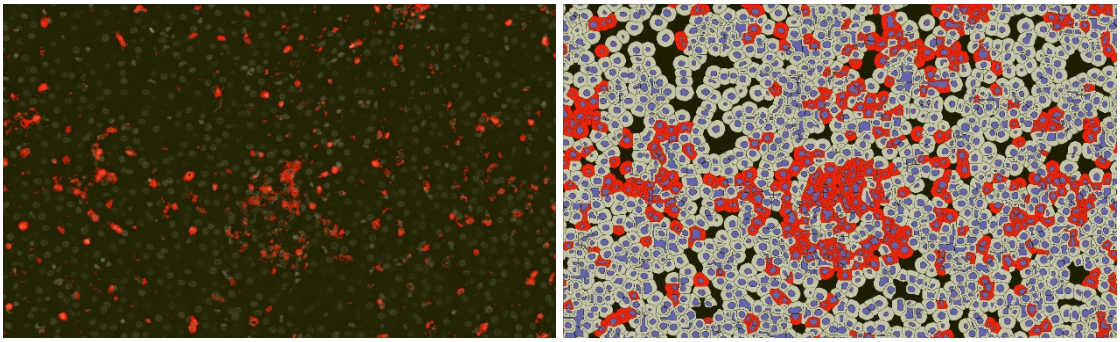

Terminal

Figure 15: Changes over time in number of cells per μm² of hepatic tissue immunoreactive for MPO (Neutrophil marker).

Number of cells per μm² immunoreactive for MPO ranged from 0.000107156 in a control animal to 0.001078165 in a 6 DPE animal. Statistical significance of terminal and 6 DPE animals was observed when compared to all other groups ≤ 4 DPE as well as for control-3 DPE animals relative to 5 DPE animals (Figure 16).

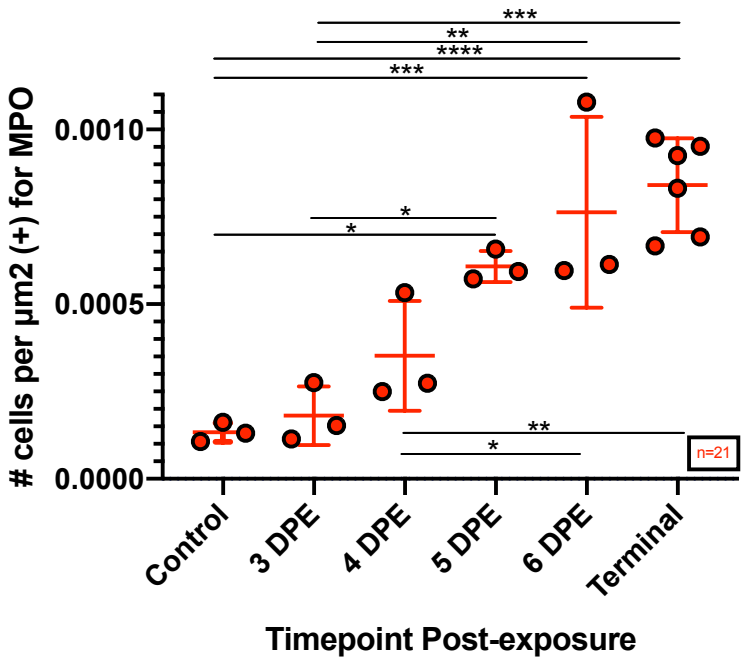

Figure 16: Temporal change in the number of cells per µm² immunoreactive for MPO.
One-way ANOVA and post-hoc Tukey correction for multiple comparisons: P-value < 0.0001.

The decrease in Heppar area quantification over time was strongly correlated with changes in immunoreactivity for VP35 as was the temporal increase in MPO (r = -081; r = 0.88). Changes in Heppar and MPO were also strongly negatively correlated to each other (r = -0.87). Additionally, AQ and HP module results for MPO were very highly correlated (r = 0.99).

Table 9. Correlation Matrix for mIHC-2.

	VP35	Heppar	MPO	Heppar & VP35	MPO & VP35
VP35	1.00	**-0.81**	**0.88**	0.71	**0.90**
Heppar	**-0.81**	1.00	**-0.87**	-0.69	-0.74
MPO	**0.88**	**-0.87**	1.00	**0.75**	**0.77**
Heppar & VP35	0.71	-0.69	**0.75**	1.00	0.59
MPO & VP35	**0.90**	-0.74	**0.77**	0.59	1.00

Colocalization of Biomarker Immunoreactivity - Condition 2

Colocalization of VP35 with both MPO and with Heppar, which may indicate viral infection of hepatocytes, was statistically increased between peracute (control-4 DPE) and terminal animals. Colocalization of VP35 and MPO (Figure 17A) ranged from 0.00051% at 3 DPE to 0.20% in a terminal animal. Colocalization of VP35 and Heppar (Figure 17B) ranged from 0.0040% at 3 DPE to 0.44% in a terminal animal.

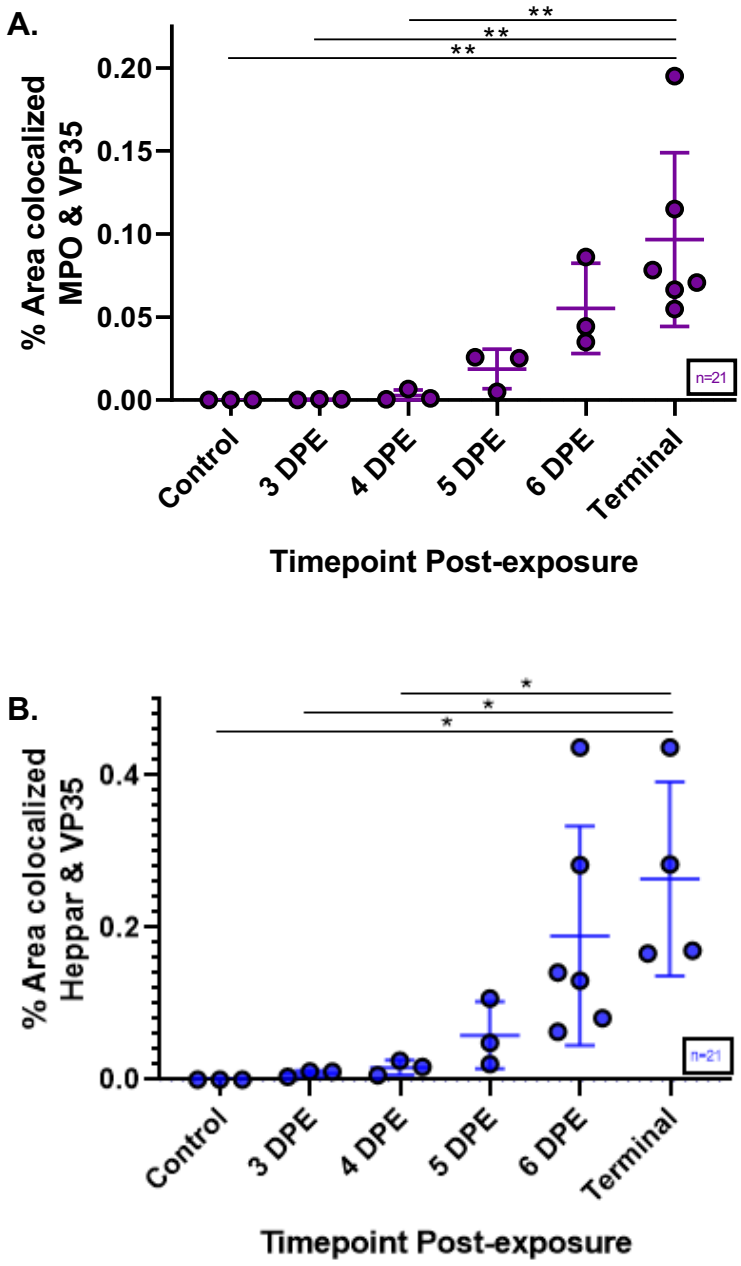

Figure 17: Temporal changes in the colocalization of mIHC-2 viral and host biomarkers in the liver of Rhesus Macaques.
(A) Myeloperoxidase (MPO) and VP35, (B) Heppar and VP35
One-way ANOVA and post-hoc Tukey correction for multiple comparisons: (A) P-value = 0.0017, (B) P-value = 0.0073

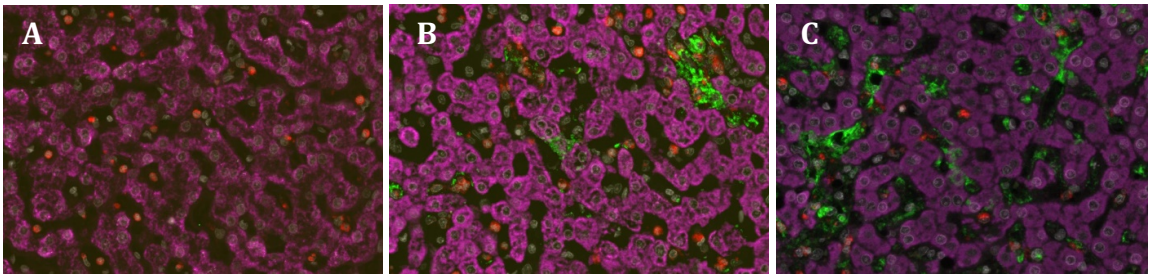

Figure 18: Changes in mIHC-2 results from 3 DPE to Terminal animals.
(A) 3 DPE animal showing presence of neutrophils (MPO) in hepatic sinusoids with rare observation of VP35, (B) 4 DPE animal showing rare colocalization of VP35 and Heppar and increased VP35 immunoreactivity, (C) Terminal animal showing even more pronounced immunoreactivity for VP35 confined predominantly to the sinusoidal compartment.

FISH Digital Image Analysis Area Quantification (AQ)

Independent Biomarker Hybridization

Raw Image **Halo™ AQ Mark-up**

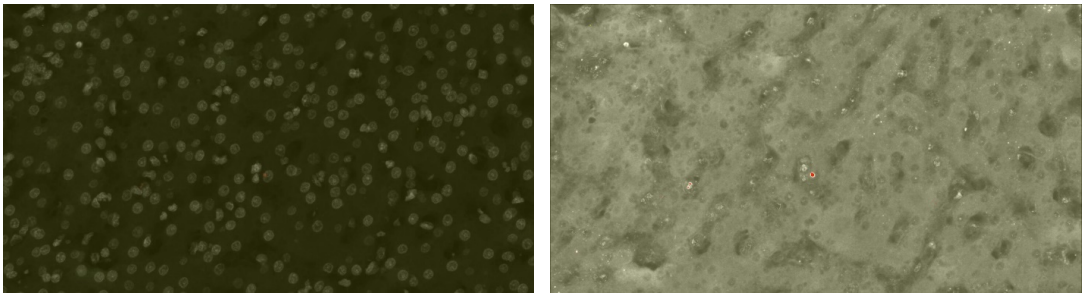

Control

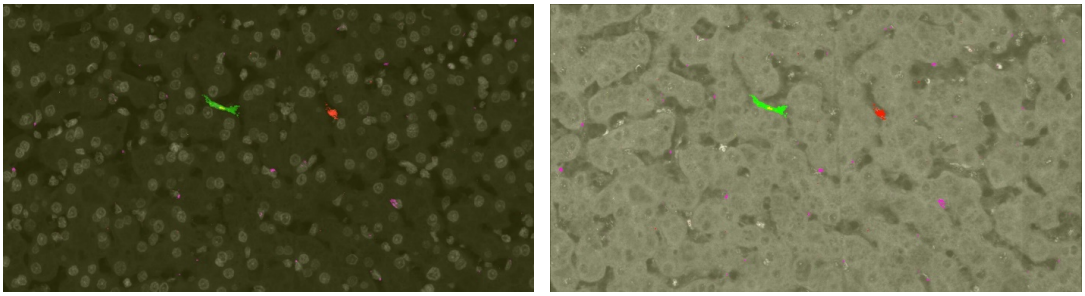

3 DPE

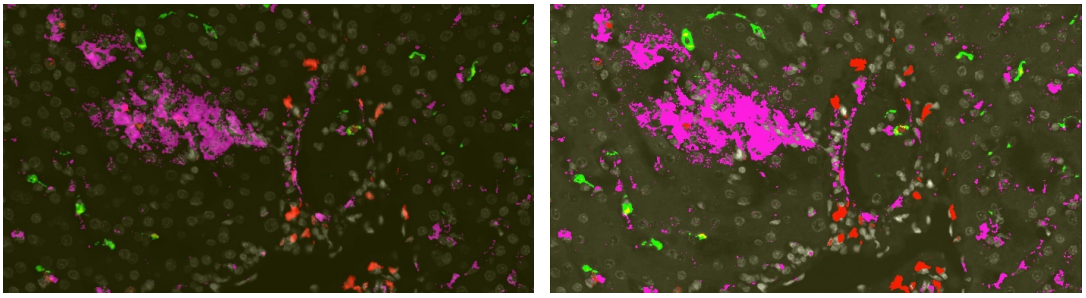

4 DPE

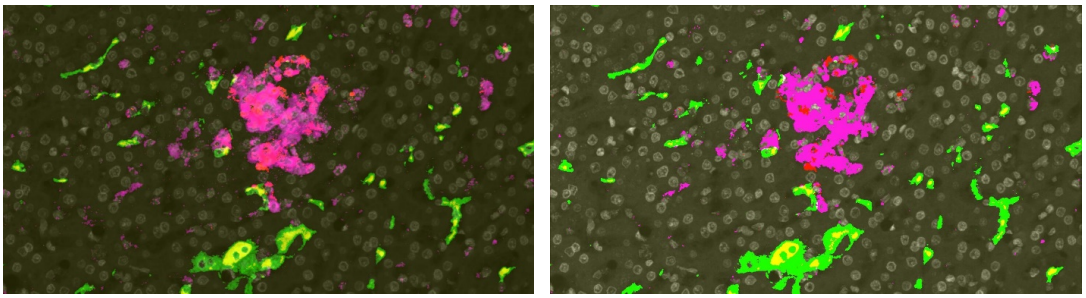

5 DPE

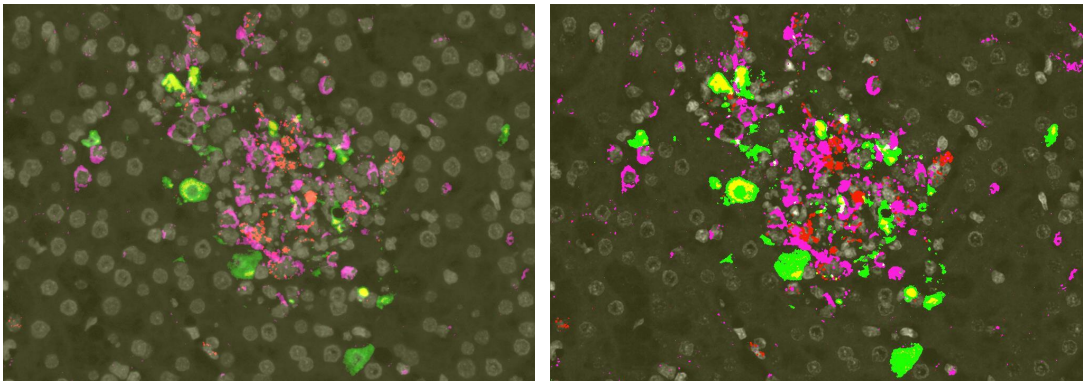

6 DPE

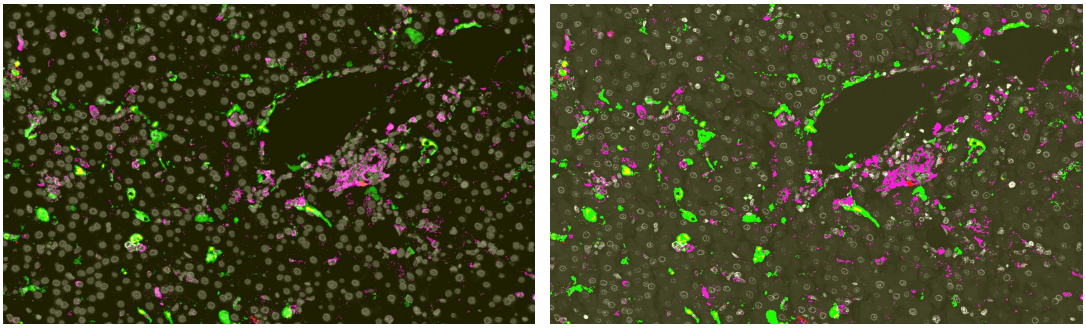

Terminal

Figure 19: Changes over time in area of hepatic tissue hybridized for *VP35 (Green)*, *IL-6 (Red)*, and *ISG-15 (Cyan)* genes.

EBOV *VP35* hybridization ranged from a minimum of 0.0316% (controls excluded; 0%) at 3 DPE to a maximum of 2.70604% in a terminal animal. Intergroup statistical significance for VP35 expression was observed across peracute and 6 DPE animals as well as between control and terminal animals (Figure 20A). Interleukin-6 (*IL-6*) hybridization ranged from a minimum of 0.00203% in a control animal and 0.00956% at 3 DPE to a maximum of 1.01279% in a terminal animal. Statistical significance of terminal animals was observed when compared to all peracute groups (Figure 20B). Interferon-stimulated gene-15 (*ISG-15*) hybridization ranged from a minimum of 0.00000643% in a control animal and 0.0211% at 3 DPE to a maximum of 1.47283% in a 6 DPE animal. Statistical significance of 6 DPE animals was observed when compared to all other groups, including terminal animals, and statistical significance was observed between peracute and terminal animals as well as between control-3 DPE and 5 DPE animals (Figure 20C).

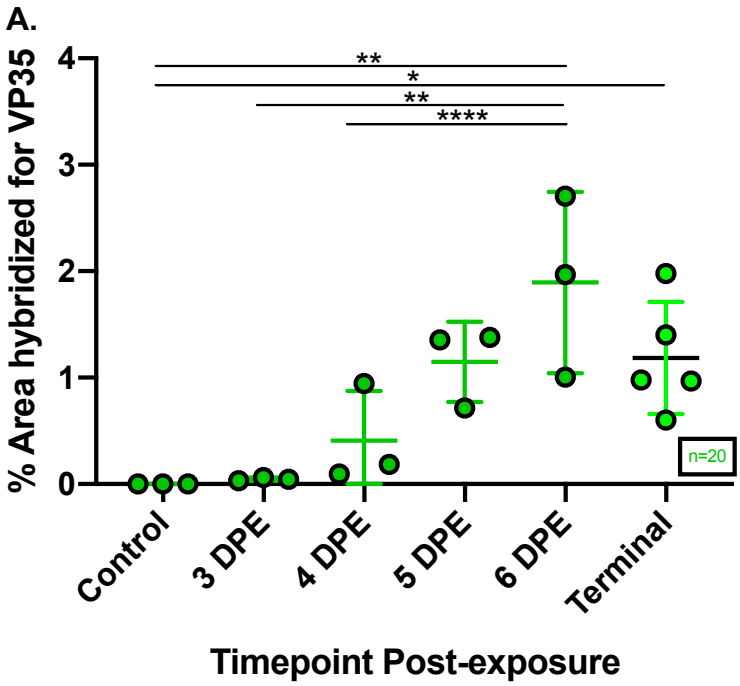
A.
% Area hybridized for VP35
4
3
2
1
0
**
*
**
****
n=20
Control
3 DPE
4 DPE
5 DPE
6 DPE
Terminal
Timepoint Post-exposure

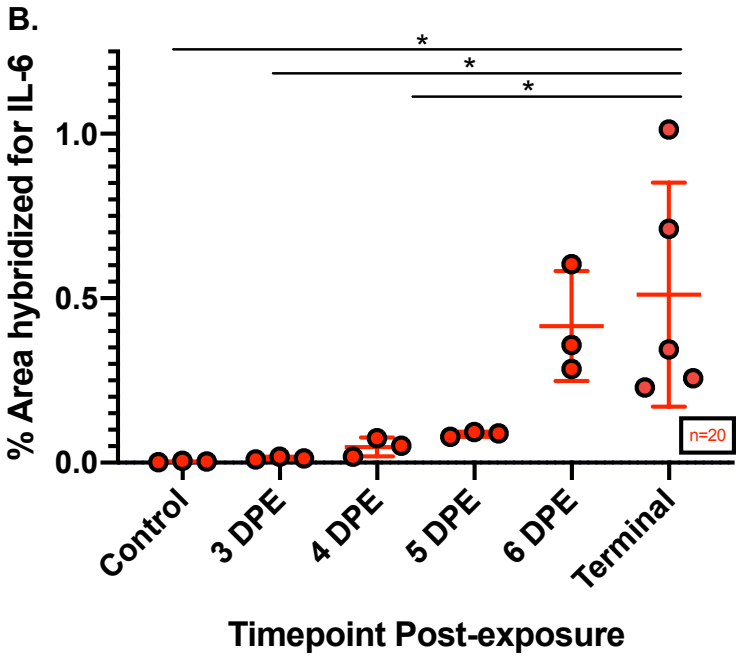
B.
% Area hybridized for IL-6
1.0
0.5
0.0
*
*
*
n=20
Control
3 DPE
4 DPE
5 DPE
6 DPE
Terminal
Timepoint Post-exposure

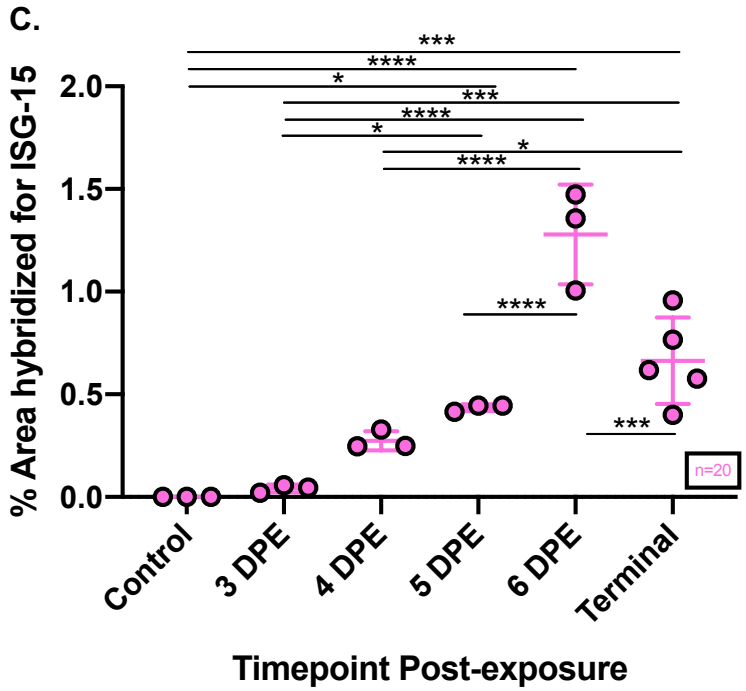

Figure 20: Temporal changes in the total area quantification of viral and host gene expression in the liver of Rhesus Macaques.
(A) *VP35*, (B) Interleukin-6 (*IL-6*), (C) Interferon-stimulated Gene-15 (*ISG-1*)
One-way ANOVA and post-hoc Tukey correction for multiple comparisons:
A) P-value = 0.0013, B) P-value = 0.0072, (C) P-value < 0.0001

Table 10. Correlation Matrix for FISH.

	VP35	ISG-15	IL-6	ISG-15 & IL-6	ISG-15 & VP35	IS-15, IL-6 & VP35	IS-15, IL-6 & VP35
VP35	1.00	0.75	0.38	0.19	0.52	0.77	0.60
ISG-15	0.75	1.00	0.63	0.67	0.78	0.83	0.90
IL-6	0.38	0.63	1.00	0.74	0.83	0.72	0.68
ISG-15 & IL-6	0.19	0.67	0.74	1.00	0.68	0.56	0.82
ISG-15 & VP35	0.52	0.78	0.83	0.68	1.00	0.84	0.72
IL-6 & VP35	0.77	0.83	0.72	0.56	0.84	1.00	0.82
IS-15, IL-6 & VP35	0.60	0.90	0.68	0.82	0.72	0.82	1.00

Simple linear regression indicates that *only ISG-15* positively predicts increased hybridization for *VP35* (Figure 21), and there is a stronger correlation between *ISG-15* and *VP35* (r = 0.75) than when comparing *IL-6* and *VP35* (r = 0.38). ISG-15 and IL-6 were also positively correlated with each other (r = 0.63).

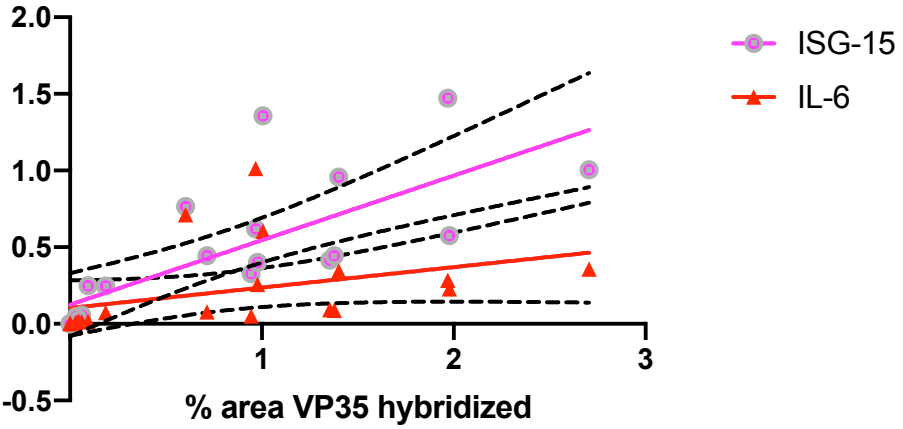

Figure 21: Simple linear regression of FISH host biomarker gene expression on EBOV VP35 viral marker expression.
IL-6: *%VP35 = 0.1333*(%IL-6) + 0.1035, R-square = 0.1460, P-value = 0.0964*
ISG-15: *%VP35 = 0.4211*(%ISG-15) + 0.1248, R-square = 0.5655, P-value = 0.0001*

Colocalization of Biomarker Hybridization

Colocalization of *ISG-15* and *IL-6* hybridization was prominent in peri-portal areas in acute and terminal disease (Figure 23) and was statistically increased between control-3 DPE and terminal animals. Colocalization of *ISG-15* and *IL-6* hybridization ranged from 0.00% in a control animal and 0.000134% at 3 DPE to 0.0877% in a terminal animal (Figure 22A). Colocalization of both *ISG-15* and VP35 hybridization as well as *IL-6* and *VP35* hybridization were significantly increased between peracute and 6

DPE-terminal animals as well as between 5 DPE and terminal animals. More rare colocalization of *ISG-15* and *VP35* hybridization ranged from 0.00000432% at 3 DPE to 0.0352% in a terminal animal (Figure 22B). More frequent colocalization of *IL-6* and *VP35* hybridization ranged from 0.000803% at 3 DPE to 0.200183% in a terminal animal and also increased significantly from 5 to 6 DPE (Figure 22C). While also more rare, colocalized hybridization of all three genes included in FISH did occur and ranged from 0.0000016% at 3 DPE to 0.0116% in a 6 DPE animal. Colocalization of *ISG-15*, *IL-6* and *VP35* increased significantly from peracute time points (control-4 DPE) when compared to both 6 DPE and terminal animals as well as from 5 to 6 DPE and from 6 DPE to terminal animals (Figure 22D).

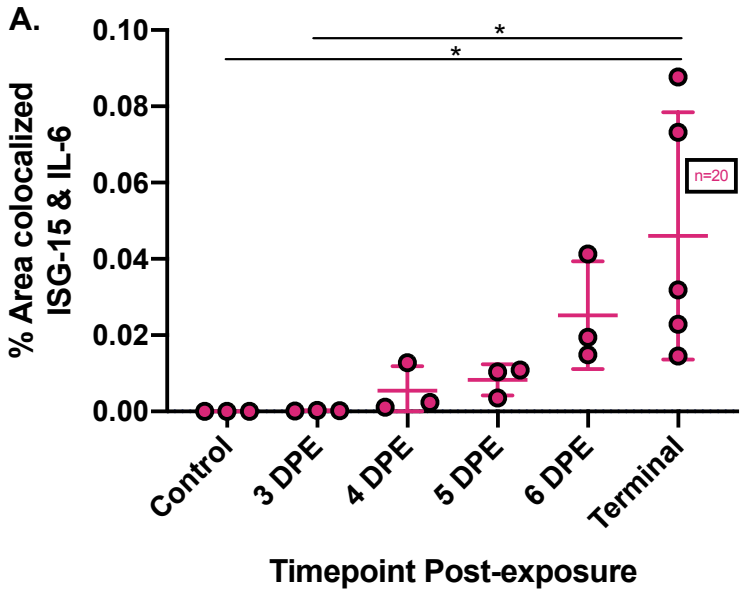

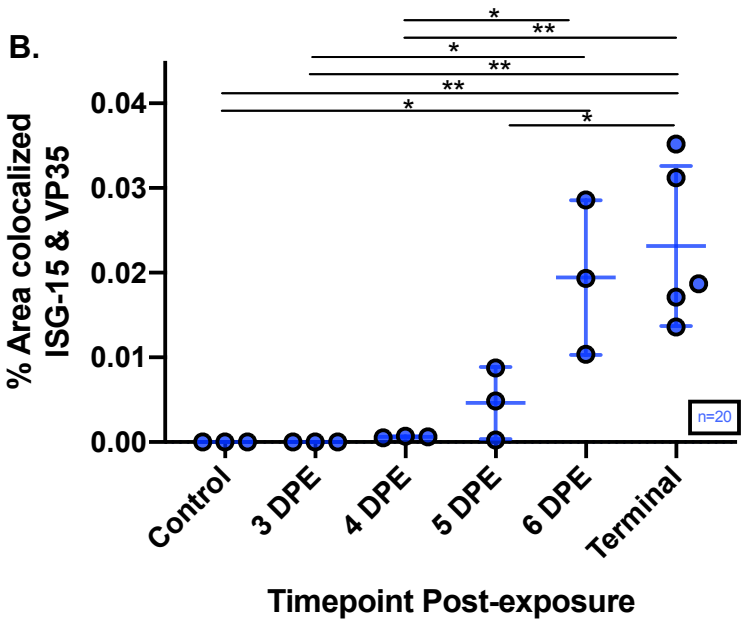
B.
% Area colocalized
ISG-15 & VP35
0.04
0.03
0.02
0.01
0.00
*
**
*
**
**
*
*
n=20
Control
3 DPE
4 DPE
5 DPE
6 DPE
Terminal
Timepoint Post-exposure

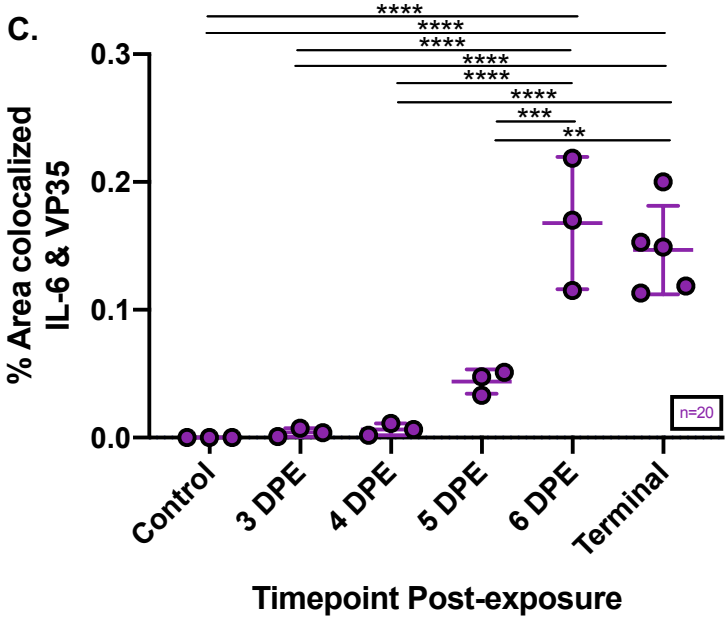
C.
% Area colocalized
IL-6 & VP35
0.3
0.2
0.1
0.0
****
****
****
****
****
****
***
**
n=20
Control
3 DPE
4 DPE
5 DPE
6 DPE
Terminal
Timepoint Post-exposure

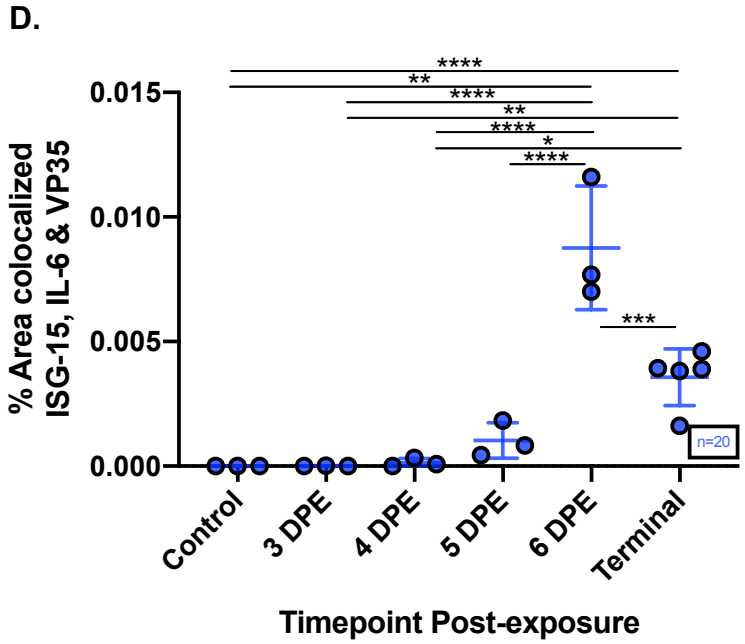

Figure 22: Temporal changes in the colocalization of viral and host biomarker gene expression in the liver of Rhesus Macaques.
(A) *ISG-15* and *IL-6*, (B) *ISG-15* and *VP35*, (C) *IL-6* and *VP35*, (D) *ISG-15*, *IL-6* and *VP35*
One-way ANOVA and post-hoc Tukey correction for multiple comparisons:
(A) P-value = 0.0182, (B) P-value = 0.0003, (C) P-value < 0.0001, (D) P-value < 0.0001

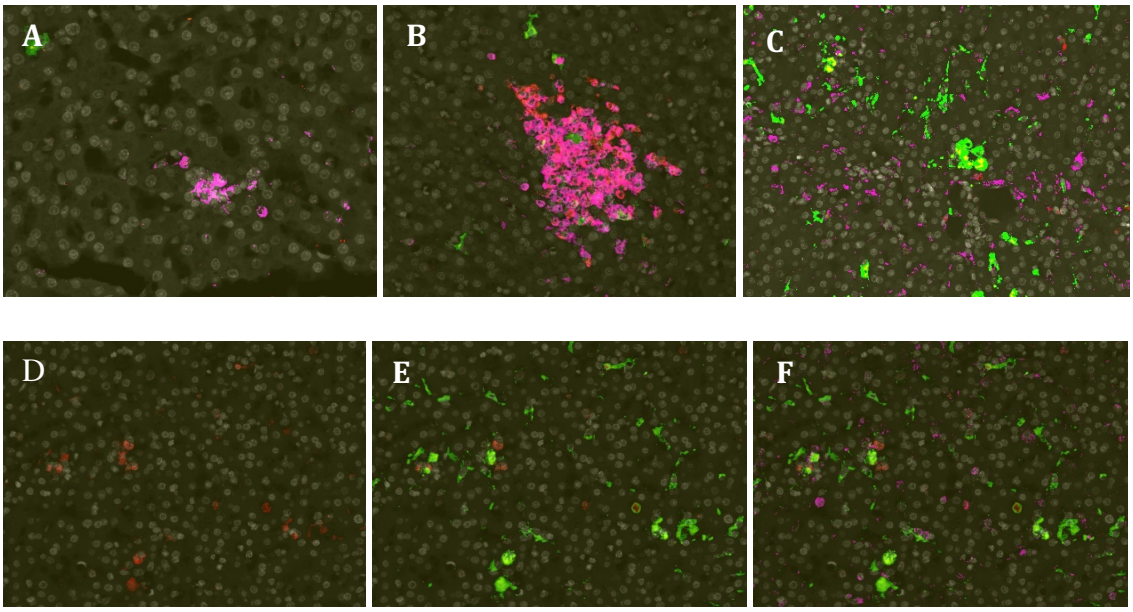

Figure 23: Changes in FISH observed quantitiatively and qualitatively over time. (A) Small aggregate of *ISG-15* hybridized cells visible in 3 DPE animal (Ordinal Score-1), (B) Larger cluster of *ISG-15* hybridized cells (Ordinal Score-2) with visible colocalization of *IL-6*, (C) *Diffuse global ISG-15* hybridization (Ordinal Score-3) in a 5 DPE animal, (D) Visualization of only the red channel (*IL-6*), (E) Colocalization (yellow) of *IL-6* within *VP35* hybridized cells, (F) Separation of channels shows colocalization of *IL-6* and *VP35* hybridization, but no observed colocalization of *ISG-15* and *VP35* hybridization.

Qualitative Findings for Biomarker Hybridization

In Situ hybridization-positivity for EBOV *VP35* was characterized by either generalized cytoplasmic signaling or intense discrete cytoplasmic foci interpreted to represent viral ribonucleoprotein complexes. Hybridization was initially reserved to sinus histiocytes at 3 DPE (3/3), later observed within hepatocytes at 4 DPE (2/3), and ultimately within blood leukocytes, fibrovascular stroma (vascular smooth muscle, fibroblasts, myofibroblasts, & pericytes) and endothelium by 5 DPE (1/3). By 6 DPE, hybridization persisted within all of these anatomical compartments (9/9); however, was

more prominent in the fibrovascular stroma for terminal animals when compared to earlier time points. Only two animals had marked hepatocyte hybridization (≥30%) (5 DPI & 6 DPI). Control animals (3/3) displayed no EBOV *VP35* hybridization.

In Situ hybridization-positivity for *IL-6* mRNA was characterized by fine discrete cytoplasmic puncta. Hybridization was initially mild and restricted to sporadic sinus histiocytes, portal, and central fibrovascular stroma in both control and 3 DPE animals (6/6). By 4 DPE *IL-6* hybridization progressed to moderate severity within the aforementioned compartments (2/3) and was first observed within the hepatic capsule (2/3). By 5 DPE hybridization progressed to marked severity (2/3), and first became apparent in blood leukocytes. There was an apparent decline in *IL-6* hybridization for the 8 DPE terminal animals when compared to all animals between 4-7 DPE. *IL-6* hybridization was never observed within hepatocytes (21/21). Colocalization of *IL-6* and EBOV *VP35* hybridization was most apparent within areas of hepatocellular necrosis containing intense cellular inflammatory infiltrate.

ISG-15 hybridization was the most ubiquitous in reference to affected cell phenotypes. Hybridization was first observed at 3 DPE in scattered sinusoidal histiocytes (1), followed by clusters of ISG-15 hybridized histiocytes (2), and finally generalized global ISG-15 hybridization in histiocytes, hepatocytes, blood, biliary epithelium, and/or vascular compartments (3). Colocalization with EBOV *VP35* was extremely rare; however, hybridization was frequently observed in close proximity to infected cells.

Table 11. Semi-quantitative findings for FISH.

	VP35 HYBRIDIZATION				IL-6 HYBRIDIZATION					ISG-15 HYBRID.
TIME POINT	***blood***	***sinus histiocytes***	***hepatocytes***	***endothelium and fibrovascular stroma***	***blood***	***sinus histiocytes***	***hepatocytes***	***endothelium and fibrovascular stroma***	***capsule***	***Ordinal Score***
CONTROL	-	-	-	-	-	+	-	+	-	0
CONTROL	-	-	-	-	-	+	-	+	-	0
CONTROL	-	-	-	-	-	+	-	+	-	0
3 DPE	-	+	-	-	-	+	-	+	-	1
3 DPE	-	+	-	-	-	+	-	+	-	1
3 DPE	-	+	-	-	-	+	-	+	-	2
4 DPE	-	++	-	-	-	+	-	++	-	2
4 DPE	-	++	+	-	-	++	-	++	+	2
4 DPE	-	+++	++	-	-	++	-	+++	+	3
5 DPE	+	+++	+++	+	+	+++	-	+++	+	3
5 DPE	-	++	+	-	-	++	-	++	+	2
5 DPE	+	++	++	+	+	+++	-	+++	+	3
6 DPE	+	+++	++	+	+	+++	-	+++	+	3
6 DPE	+	++	++	+	+	+++	-	+++	+	3
6 DPE	+	+++	+++	+	+	+++	-	+++	+	3
TERMINAL - 6 DPE	+	++	++	+	+	++	-	++	+	3
TERMINAL - 6 DPE	+	+++	++	++	+	++	-	++	+	3
TERMINAL - 7 DPE	+	+++	++	++	+	+++	-	++	+	3
TERMINAL - 7 DPE	+	++	++	++	+	++	-	++	+	3

TERMINAL - 8 DPE	+	++	+	++	+	++	-	+	+	3
TERMINAL - 8 DPE	+	++	++	++	-	++	-	+	+	3

+, EBOV RNA- positive cells or hybridization in specified compartment were rarely detected; ++, EBOV-positive cells and/or compartment-specific hybridization were occasionally detected; +++, EBOV-positive cells and/or compartment-specific hybridization were frequently detected; –, no EBOV-positive cells or hybridization in specified compartment were detected

Comparison of Findings from Brightfield, mIHC and FISH

Percent total area immunoreactivity for VP35 in mIHC-1 and mIHC-2 for serial liver sections collected from each animal was compared via paired t-test and showed no statistically significant difference (P-value < 0.0001) indicating that thresholds across the AQ modules used for the green channel, which was used to visualize VP35, were highly precise. Very strong positive correlation was also indicated by the Pearson correlation coefficient (r = 0.9909 and P-value < 0.0001) (Appendix III). For all biomarkers except Heppar, there was no statistically significant change in peracute animals (control-4 DPE) indicating that increase in percent immunoreactivity for VP35 and strongly correlated changes in CD68, MP, and TF do not occur until between 4 and 5 days post-infection.

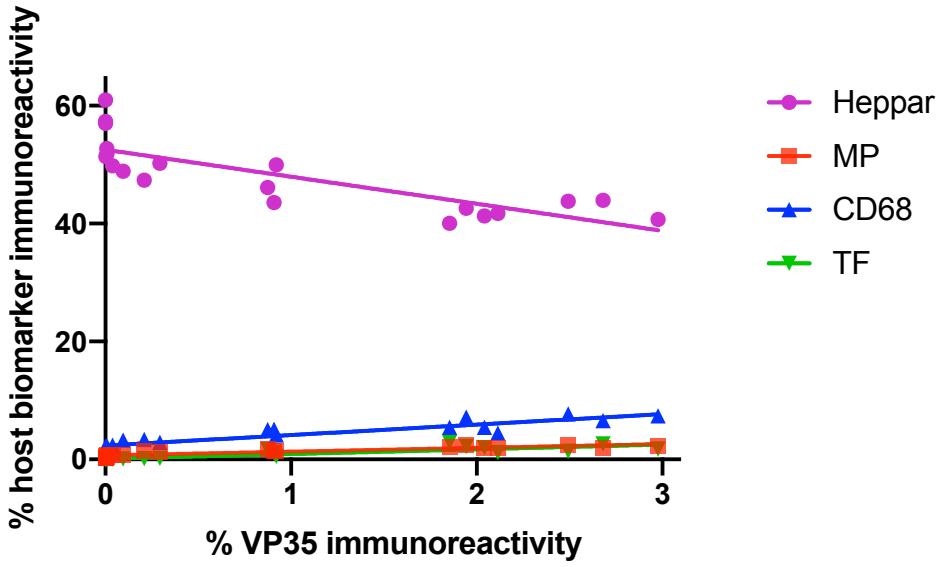

Figure 24: Simple linear regression of mIHC host biomarker immunoreactivity on EBOV VP35 viral marker immunoreactivity.
Equations included in Appendix IV. All P-values < 0.0001.

Across mIHC conditions 1 and 2, simple linear regression showed a statically significant (P-value < 0.0001) relationship between all markers, including MPO, and percent VP35 immunoreactivity (Figure 24). All host biomarker variability across and within groups for each time point can partially predict variance in VP35 (R square > 50%, P-value < 0.0001).

The only 3 DPE animal with viral inclusions observed in histiocytes during histopathological analysis also had the highest percent of colocalization of VP35 and CD68 of any of the 3 DPE animals, (0.0039%) and had a higher percent tissue immunoreactivity for CD68 (2.38%), although not for VP35. Hepatocytic inclusions became apparent at 5 DPE histopathologically, when percent colocalization of Heppar and VP35 was also first measured to be statistically significant (0.20% and above although one 4 DPE animal with 0.25% merging did not get evaluated as having viral inclusions).

Increases in individual host biomarkers were not consistently matched to increases in cumulative liver ordinal scores (i.e., some animals with higher scores had lower percent area immunoreactivity for associated biomarker(s) relative to animals with a lower score) but overall statistical trends, from simple linear regression (Appendix IV) and testing for correlation (Table 12), indicated a strong positive predictive relationship between histopathological, immunohistochemical, and *In Situ* hybridization findings.

Pearson's correlation coefficient confirmed that all biomarkers were strongly correlated with histopathology scores for necrosis, inflammation, and fibrin deposition as well as cumulative liver score ($r > 0.5$; $p < 0.001$). *ISG-15* was most strongly correlated

with CD68 (r=0.83) and also strongly correlated with MPO (r = 0.78). *IL-6* was most strongly correlated with VP35 and TF (r = 0.74; r = 0.73) while least correlated with VP35 hybridization (r = 0.38; P value < 0.05). Both MPO and CD68 were very strongly correlated with not only each other (r = 0.95) but also overall liver score (r = 0.0.83; r = 0.84). Heppar was also strongly correlated to cumulative score (r = -0.90) and was negatively correlated with MPO (r=-0.89). Increase in VP35 over time was also very strongly correlated with Necrosis Score (r = 0.91) and CD68 (r = 0.90) and strongly correlated with all other host biomarkers and ordinal scores (r > 0.50).

Table 12. Heat map of correlation coefficients for ordinal semi-quantitative and continuous quantitative results.

	Ordinal Liver Score	***Necrosis Score***	***Inflamm. Score***	***Fibrin Score***	VP35	Heppar	MP	CD68	TF	*VP35*	*ISG15*	*IL6*
Ordinal Liver Score	1.00	0.85	**0.92**	**0.91**	0.79	**-0.90**	0.83	0.84	0.73	0.73	0.72	0.65
Necrosis Score	0.85	1.00	0.88	0.88	**0.91**	-0.83	0.87	0.87	0.83	0.79	0.64	0.60
Inflamm. Score	**0.92**	0.88	1.00	**0.90**	0.84	-0.83	0.88	0.87	0.79	0.77	0.68	0.68
Fibrin Score	**0.91**	0.88	**0.90**	1.00	0.80	-0.84	0.85	0.83	0.77	0.80	0.74	0.65
VP35	0.79	**0.91**	0.84	0.80	1.00	-0.81	0.88	**0.90**	0.87	0.78	0.63	0.74
Heppar	**-0.90**	-0.83	-0.83	-0.84	-0.81	1.00	-0.89	-0.84	-0.81	-0.71	-0.77	-0.64
MP	0.83	0.87	0.88	0.85	0.88	-0.89	1.00	**0.95**	0.84	0.89	0.78	0.59
CD68	0.84	0.87	0.87	0.83	**0.90**	-0.84	**0.95**	1.00	0.84	0.89	0.83	0.66
TF	0.73	0.83	0.79	0.77	0.87	-0.81	0.84	0.84	1.00	0.61	0.59	0.73
VP35	0.73	0.79	0.77	0.80	0.78	-0.71	0.89	0.89	0.61	1.00	0.75	0.38
ISG15	0.72	0.64	0.68	0.74	0.63	-0.77	0.78	0.83	0.59	0.75	1.00	0.63
IL6	0.65	0.60	0.68	0.65	0.74	-0.64	0.59	0.66	0.73	0.38	0.63	1.00

Observation of area quantification (AQ) over time post-infection showed a trend of increasing inflammation in the liver of EBOV-infected rhesus macaques, indicated by a statistically significant rise in percent total area immunoreactivity for macrophage (CD68), Tissue Factor (TF), and neutrophil (MPO) biomarkers. This was also confirmed via cell phenotyping, with an increase in number of neutrophils (cells positive for MPO) and macrophages (cells positive for CD68) measured per μm^2 over time, and correlates with hepatic inflammation, as indicated via analysis of H&E. Increased Tissue Factor, also indicative of inflammation, was measured via AQ at earlier time points (starting at 3 DPE) than fibrin deposition was observed histopathologically (4 DPE and later).

Comparing sections used in histopathological analysis and mIHC, visible increases in size and frequency of histiocytic aggregates and colocalization within aggregates of CD68 and VP35 occurred over time, as Necrosis Score increased (Figure 25).

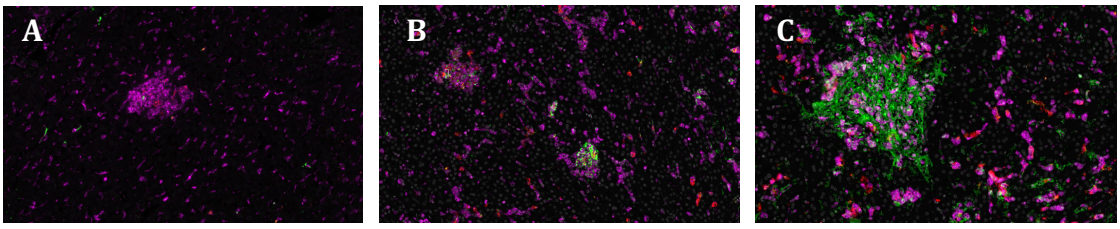

Figure 25: Temporal progression of necrosis severity and % immunoreactivity for biomarkers.
(A) 5-DPE, Necrosis-1, (B) 6 DPE; Necrosis-2, (C) Terminal; Necrosis-3

DISCUSSION

Use of DIA as a Tool for EBOV Pathogenesis Research

Previous research has led to important findings concerning NHP host-response to EBOV, confirming virulence and identifying tissue tropism and sites of viral persistence (Geisbert et al., 2003a, Geisbert et al., 2003b; Cooper et al., 2018; Chugtai et al., 2016). However, pathology studies have primarily been restricted to terminal animals dictated by pre-determined clinical endpoints and use of semi-quantitative or descriptive qualitative approaches. Specifically, immunohistochemical analysis has traditionally relied on methods that are not easily reproducible including qualitative descriptions of immunoreactivity, semi-quantitative ordinal scoring or categorical definitions (rare, moderate, frequent), qualitative cell phenotyping (i.e. cognitive application of histology knowledge in the context of differential nuclear counterstains) and manual cell counting, which is extremely time intensive and prone to observer bias and variability in reporting (Fedchenko & Reifenrath, 2014).

This was the first study that quantitatively evaluated temporal dissemination of EBOV infection within distinct anatomical compartments of the liver combined with quantitative and qualitative spatial analysis of the pro-inflammatory cytokine *IL-6* and the interferon-stimulating gene *ISG-15* by utilizing digital image analysis (DIA) on whole slide images (WSI). In comparison to qualitative analysis, DIA enables researchers with more reproducible and robust datasets that are amenable to statistical analysis and comparison with other study datasets (Snead et al., 2016; Rizzardi et al., 2012). Snead et

al. (2016) reviewed 3017 cases across surgical subspecialties, which were evaluated by 17 pathologists via DP, and compared results to previous analysis via routine brightfield microscopy, evaluated by the same or different pathologists. Results were within the 95% confidence interval for intra-observer and inter-observe variability, indicating there was no statistically significant difference between DP and legacy brightfield analysis for histopathological diagnosis in the majority of cases. Rizzardi et al. (2012) compared IHC staining results for tissue microarrays from 215 ovarian serous carcinoma specimens using DIA and semi-quantitative visual scoring. They found strong agreement between classification of carcinomatous areas through DIA and manual annotation, confirmed via Spearman correlations. Previous reviews have also found that DIA makes it feasible to decipher subtle and minute changes, which potentially could reflect magnitudes of biological difference, through the generation of continuous variable data. An example includes measurement of the number or area of infiltrating leukocytes in wild-type versus knock-out mice for a specific gene linked to development of an autoimmune disorder, rather than having to rely on qualitative evaluation of global severity of inflammation (Webster & Dunstant, 2014). DIA also greatly improves efficiency and reproducibility of analysis, since modules are semi-automatic and analysis algorithms/parameters can be shared for reuse within and across studies. However, use of DIA has primarily been limited to studies of cancers and neurological disorders and there is not yet significant evidence for its utility in infectious diseases research (Rizzardi et al., 2012).

To improve our understanding of the applications of DIA for EBOV pathogenesis research, we supplemented descriptive ordinal and qualitative pathology workflows with

digital pathology, image analysis, mIHC, and mFISH. Using DIA, we were able to measure statistically significant quantitative temporal changes in WSIs of liver from EBOV-infected rhesus macaques during **peracute** (3-4 DPE), **acute** (5-6 DPE), and **terminal** (6-8 DPE) infection that would not have been feasible to capture with qualitative observational analysis alone, including phenotyping and colocalization of biomarkers over time. Our research highlights the potential benefits of and challenges encountered in applying DIA to infectious disease pathogenesis research.

In comparing our histopathological ordinal findings to those acquired via DIA, the limitations of observational analysis become apparent. Our scale for our ordinal data was developed through user-defined criteria that we subjectively interpreted to represent the global study variability, rather than continuous and precise measurements of specific compartments and/or cell types of interest. In addition, ordinal scoring does not represent a true linear relationship for temporal changes (e.g., the difference between a score of "1" and "2" is not necessarily of the same magnitude as the difference between a score of "2" and "3"). For example, in our ordinal scoring, necrosis scores of 1 or 2 represent evident ongoing hepatocyte necrosis, as depicted by hypereosinophilic cytoplasm and pyknotic nuclei, whereas a score of 3 represents large areas of hepatocellular loss, with minimal active hepatocyte necrosis. The same goes for our inflammation scores, where scores of 1 and 2 represent sinusoidal expansion by histiocytes whereas a 3 is representative of inflammatory aggregates in areas of necrosis with significant infiltration of neutrophils.

Digital Image Analysis for mIHC: Findings and Limitations

Using DIA, we were able to objectively and precisely measure changes in cell populations as relates to EBOV pathogenesis, including inflammation and necrosis, over time. With area quantification and cell phenotyping, we detected changes during peracute and acute infection that did not appear significant via qualitative or semi-quantitative observation alone. Ordinal scores for liver inflammation, fibrin thrombi, hepatocellular necrosis and cumulative score increased substantially but not significantly from 4-5 DPE. Using the more sensitive area quantification DIA module we were able to detect statistically significant changes not reflected by ordinal scores in percent positive immunoreactivity for CD68, TF, MPO and Heppar and probe hybridization for *IL-6* and *ISG-15* from peracute to acute and terminal EBOV infection.

Dissemination of EBOV to the liver did not become histopathologically evident until approximately 4 DPE, although it was detected via mIHC and mFISH at 3 DPE. We first detected EBOV immunoreactivity free in sinusoids and in sinusoidal histiocytes at 3 DPE, which increased significantly from peracute to acute and terminal infection. We found that temporal increase in EBOV immunoreactivity was positively correlated with acute and terminal increases in neutrophils and macrophages within the liver (statistically significant increase in MPO in 5 DPE-terminal animals; significant increase in CD68 in 6 DPE and terminal animals; increased inflammation score) and overexpression of Tissue Factor (significant increase in terminal animals; further correlated with increased fibrin score). Whether increasing numbers of macrophages represent kupffer cell hyperplasia and/or migration of non-resident macrophages to the liver post-infection could not be

determined given that CD68 is non-specific and expressed on the membrane of all monocyte lineage cells. Increase in EBOV immunoreactivity was negatively correlated with necrosis of hepatocytes (i.e. statistically significant decrease in Heppar across all time points; increased necrosis score). We also measured a high correlation between increased immunoreactivity for MPO and decreased reactivity for Heppar, which reflects that neutrophils, which are phagocytic innate immune cells, are likely being recruited to sites of necrosis in the liver to clean up necrotic cellular debris (Lämmerman, 2016).

In our study, while all biomarkers related to inflammation were found to increase significantly, via both AQ as well as HP analysis where applicable, there was the most inter-group frequency of statistical significance for temporal increase in immunoreactivity for TF, with significant changes observed even when comparing 5 DPE to terminal animals. This correlates with our observational findings, in which fibrin score was most sensitive for detecting inter-group variations, showing DIA is able to accurately recapitulate observational analysis while also highlighting the ability of DIA to better establish statistical significance relative to ordinal scoring.

Our finding that loss of hepatocytes (decrease in Heppar immunoreactivity) was statistically significant across all time points, even between control and 3 DPE animals, and was inversely correlated with number of neutrophils and histiocytes, which were both strongly positively correlated with increased necrosis score over time, indicates that necrosis is an early and sustained effect of EBOV infection in the liver. Again, our DIA results for necrosis correlated strongly with our observational finding that necrosis score was the second most sensitive to inter-group variation and provide additional measures of

statistical significance not captured through ordinal scoring. While hepatocellular necrosis has been established as a histologic hallmark of EBOV in NHPs and other animal models (Geisbert et al., 2003a; Cooper et al., 2018), no study has used IHC to quantify hepatocellular loss over time following EBOV infection by displaying temporal loss of immunoreactivity to a liver-specific antigen (Heppar).

Our findings are consistent with past IHC research, which has reported presence of EBOV in sinusoidal histiocytes starting at 3 DPE, an increase in macrophages, neutrophils and TF over time, and small foci of hepatocellular necrosis in the liver of humans and NHPs with fatal or acute EBOV (Geisbert et al., 2003a; Geisbert et al., 2003b; Wyers et al., 1999). Previous studies have reported that neutrophilia is associated with fatal outcomes of EBOV in humans as well as cynomolgus macaques and rhesus macaques (McElroy et al, 2019; van der Ven et al., 2015; Geisbert et al., 2003a). Geisbert et al. (2003a) observed neutrophilia occurring from 1 to 4 days post-infection via hematology with increased cell count persisting through 6 DPE as well as observing increased neutrophils in hepatic sinusoids and central veins beginning at 4 DPE in cynomolgus and rhesus macaques. Our quantitative analysis further substantiates these findings and supports that an increased tissue demand of the liver is in part responsible for neutrophilia. Geisbert et al. (2003b) also described significant overexpression of TF in cynomolgus macaques using hematology, found via transmission electron microscopy that this increased TF expression was associated with macrophages, and qualitatively described and observed fibrin deposition associated with EBOV-infected macrophages in response to infection (2003a).

Certain studies on EBOV pathogenesis using traditional methods did not observe inflammatory infiltration in the liver or claimed that there was only minimal inflammation of EBOV-infected NHPs (Ryabchikova et al, 1999, Martines, 2015). Similarly, we could not establish statistical significance for semi-quantitative inflammation scores except when comparing peracute and terminal animals. By using DIA, we were able to measure significant changes across additional time points and for specific cell types, which highlights that the small but significant changes in immunoreactivity that we measured can be difficult to capture accurately through qualitative and semi-quantitative approaches.

We could not establish statistical significance when comparing controls to peracute animals for biomarkers, even when employing DIA. This is in part attributed to the small sample size of this study. NHPs, while the gold standard for EBOV pathogenesis research, are expensive, require special facilities and housing, additional training of personnel, and present distinctive ethical challenges when compared to rodents leading, which contributed to our small sample size (Siragam et al., 2018; St. Claire et al., 2017). However, our results clearly do indicate a measurable, although not statistically significant, increase in immunoreactivity for all biomarkers beginning as early as 4 DPE and steadily growing by orders of magnitude across subsequent days post-exposure, which is further reflected by increased inflammation score over time. These findings are also supported by and build upon previous histopathological research in EBOV-infected green monkeys and baboons, which showed increased severity of hepatocellular damage beginning at 4 DPE and continuing to worsen through 6 DPE,

with much less severe changes observed at 3 DPE (Ryabchikova et al., 1999).

We could not apply cell phenotyping modules to evaluate viral colocalization within cell subsets because we elected to train algorithms to minimize false positives and found that this compromised our sensitivity and underestimated the biology we were characterizing. Thus, we instead relied on a less complex but more specific tool in area quantification (AQ). Using AQ, we found that colocalization of CD68 and VP35 immunoreactivity were significantly increased from peracute to acute and peracute to terminal infection and that increases in immunoreactivity for CD68 and VP35 are furthermore highly correlated, as indicated by Pearson's correlation coefficient. We additionally found a highly positive correlation between TF and CD68, as well as TF and VP35, and a statistically significant increase in colocalization over time for these biomarkers. We also found that increase in colocalization of MPO and VP35 immunoreactivity, while not as large as that seen for CD68 and VP35, was statistically significant over time.

While we cannot definitively report that colocalization represents biological processes occurring in the same cell of interest given the inherent resolution limitations afforded by standard microscopy, previous research supports the conclusion that increased colocalization of CD68 and VP35 does in fact represent a trend of increasing infection of macrophages by EBOV. Macrophages have been shown to support viral replication and are infected early on after EBOV exposure (Geisbert et al., 2003a). Geisbert et al. (2003a) found that macrophages in the liver were immunoreactive for EBOV starting at 3 DPE and increased numbers of macrophages were infected from 4

DPE onwards relative to earlier time points. This study did not provide quantitative findings but instead categorized immunoreactivity as “never”, “rarely”, “occasionally”, and “frequently” detected in cells.

Significant correlation of TF, CD68 and VP35 can be explained by acknowledging that TF is expressed on the membrane of activated CD68 positive cells and is overexpressed during EBOV because VP35 indirectly activates the extrinsic coagulation pathway through activation of macrophages. Specifically, EBOV GP interacts with TLR4 on the macrophage cell membrane during cell entry, leading to induction of a pro-inflammatory response that includes increased *IL-6* and TF expression (Geisbert et al., 2003b; Olejnik et al., 2017; Okumara et al., 2010; Lai et al., 2017). Although neutrophils have not been shown to support EBOV replication, they have been found to be susceptible to infection and modulate the host immune response (Mohamadzadeh et al., 2006) and therefore colocalization of MPO and VP35 could represent increase in number of infected neutrophils over time. However, free extracellular EBOV has been described within hepatic sinusoids and increased colocalization could simply reflect the fact that increased numbers of neutrophils were observed over time (Geisbert et al, 2003a; Ryabchikova et al., 1999).

Observational analysis of our stained WSIs did indicate that during peracute infection EBOV was predominantly present extracellularly within sinusoids and in sinusoidal histiocytes and a relatively modest number of hepatocytes were infected even during acute and terminal disease. This was confirmed via AQ, which measured more macrophages than hepatocytes immunoreactive for VP35, and detected relatively small

changes in colocalization of immunoreactivity over time in comparison to more substantial changes for individual biomarker immunoreactivity. This finding supports previous semi-quantitative research in NHPs with occasional detection of immunoreactive kupffer cells starting at 3 DPE and frequent detection from 4-6 DPE, but only rare detection of immunoreactive hepatocytes starting at 4 DPE and occasional detection at 5-6 DPE (Geisbert et al., 2003a). Given that progressive hepatocyte necrosis is an established hallmark of EBOV (Marzi et al, 2015), our findings of statistically significantly decreasing Heppar immunoreactivity and an absence of substantial colocalization of Heppar and VP35 (maximum colocalization 0.4% in a terminal animal compared to 1.0% for CD68 and VP35) is reflected to confirm significant increase in Ca

Digital Image Analysis for FISH: Findings and Limitations

To date, RNA sequencing has been used to measure differential expression of cytokine and innate host immune response in EBOV using peripheral blood from naturally EBOV-infected humans or in experimentally inoculated NHPs. Acknowledging that RNA sequencing cannot provide spatial context of mRNA within tissue architecture, it is currently unknown which cell phenotypes drive differential cytokine and innate host responses in the context of EBOV (Geisbert et al., 2003a; Caballero et al., 2016; Speranza et al., 2018). While the mIHC results outlined confirm and expand upon existing histopathological and immunohistochemical analyses of EBOV-infected animals, the mFISH performed as part of this study and analyzed via DIA provides novel spatial insight into genes associated with the pro-inflammatory state and host innate response of

EBOV.

The Halo™ module designed for FISH DIA was particularly difficult to fine-tune and, given our slide resolution (200x), we could not use it to count distinct puncti or number of hybridized cells for WSIs and instead had to rely on the more accurate but superficial level of analysis afforded by the area quantification module, which we supplemented with semi-quantitative observational analysis. Given the additional challenges of fine-tuning the AQ module for FISH analysis, we will also be working to validate our algorithms and make our FISH findings more reliable before further publication of our results discussed here. Using AQ, we were able to collect preliminary findings pertaining to changes in hybridization over time and, through a combination of DIA and qualitative analysis, we were able to capture colocalization by tissue compartment and cell phenotype.

Hybridized tissue for *VP35* mRNA was measured to significantly increase by 4 DPE whereas percent tissue immunoreactivity for VP35 antigen was not significantly increased until greater than or equal to 6 DPE and after, relative to peracute animals. Additionally, we found that in terminal animals *VP35* hybridization was decreased on average, although not statistically significantly different from, values seen at 6 DPE. This could indicate that viral load is no longer at its peak and replication has decreased. Furthermore, terminal animals have reached pre-determined endpoints, suggesting that progression of clinical disease is not entirely linked to viral load. *ISG-15* and *IL-6* were significantly increased from peracute to acute (6 DPE) infection but decreased on average from 6 DPE to terminal animals. *IL-6* showed considerable variability in terminal

animals, with a much wider range of hybridization than at 6 DPE. While *IL-6* was relatively frequently colocalized with *VP35* in comparison with *ISG-15*, there was not strong correlation between percent hybridization for *VP35* and *IL-6*. Colocalization of *ISG-15* with *VP35* was extremely rare; however, *ISG-15* hybridization was more frequently observed in close proximity to infected cells.

Previous research also showed that EBOV mRNA was detected in cells that were negative for EBOV antigen at 2 DPE in the liver, consistent with our findings, and that *VP35* hybridization subsequently increased at 3 and 4 DPE, but could not establish statistical significance due to use of ordinal scoring (Geisbert et al., 2003a). Peak viral load in EBOV-infected NHPs, including rhesus macaques, was also measured to occur between 5-7 DPE followed by a decrease in viremia at later time points, consistent with our finding of decreased average viral replication in terminal animals (Madelain et al., 2018). Additionally, our observation of relatively infrequent *VP35* and *ISG-15* colocalization and more frequent *VP35* and *IL-6* colocalization supports previous research wherein infection of permissive cells, specifically immortalized human hepatic cells (Huh7) and primary monocyte-derived dendritic cells (mdDC), by EBOV has been shown to promote interleukin expression, with significant levels at 4-5 DPE, and inhibit host interferon responses (Speranza & Connor, 2017). Previous research has also shown that viral infection triggers an uncontrolled pro-inflammatory response in NHPs and induces a cytokine storm, including upregulation of *IL-6* expression, measured via hematology, which contributes to DIC and in severe cases, death (Madelain et al., 2018). In vivo research with rhesus macaques has also measured a strong increase in *ISG-15* in

circulating immune cells as early as 2-4 DPE (Caballero et al., 2016). Caballero et al. (2016) found, via real-time PCR, that IFN and ISG levels peaked in the liver at 4 DPE and remained elevated throughout acute infection but only detected a statistically significant upregulation at 8 DPE. However, our findings indicate that in the liver this response significantly increases from as early as 4 to 6 DPE (peracute to acute infection).

Caballero et al. (2016) hypothesized that upregulation of the innate immune response may be explained by bystander cell activation or mutations in VP35 that stop it from effectively blocking interferon response in infected cells. In using RNA extraction and sequencing, this and similar studies could not provide any information regarding localization within specific anatomical or cellular compartments of the liver. Our quantitative findings support the hypothesis put forth in previous research suggesting that following EBOV host cell infection, neighboring cells are capable of being appropriately primed to help mitigate further viral dissemination (Caballero et al., 2016; Speranza & Connor, 2017).

Our qualitative findings indicate that peracutely *IL-6* hybridization is found in sinusoidal histiocytes and, during acute infection, within the endothelium, fibrovascular stroma and hepatic capsule. The shift of *VP35* from histiocytes and hepatocytes to fibrovascular stroma near the end of acute infection may represent an evolutionary adoption of EBOV aimed to enable viral persistence. A recent study conducted on rhesus macaques found via IHC analysis of the EBOV viral protein NP that viral persistence occurs in the eyes, brain and testes via vascular structures but did not find evidence of persistence in key sites of viral replication such as the liver (Zeng et al., 2017). Together,

our findings and past research could indicate that during acute infection, when viral replication has already peaked, EBOV is beginning to travel from primary sites of replication like the liver to tissues where viral persistence occurs.

Future research using dual IHC-FISH staining could better link gene expression to specific tissue compartments and cell phenotypes. Further research is also required to evaluate effect of EBOV infection on host and bystander cells and viral persistence of EBOV, which will be a challenge given low survivability of NHPs post-EBOV infection (Madelain et al., 2018). However, there is ongoing research to address mortality rates in NHPs and work to more closely recapitulate lethality in humans using this animal model, including through mucosal inoculation, variable inoculation dose and concurrent use of MCMs (Claire et al., 2017; Alfson et al., 2015; Alfson et al., 2017; Dowall et al., 2017).

Study Limitations

We observed significant inter-slide variation in reference to fluorescence intensity among animals from the same treatment groups. Although our mIHC and ISH methods and image acquisition parameters were standardized, we interpret this observation to be multifactorial, resulting from a combination of pre-analytical and inherent biological variability. Several of the animals from this study reached terminal endpoints and were then euthanized at 6 DPE (n = 2), 7 DPE (n = 2), or 8 DPE (n = 3) while others were humanely euthanized at pre-determined time points. Time from death to tissue collection plays a critical role in the degree of tissue autolysis, of which the former is well established to influence downstream ancillary test results including IHC and ISH

(Kaushik et al., 2014; Rao, 2016). Furthermore, it is not known how long tissues were fixed in 10% neutral buffered formalin before being processed, which could potentially serve as an additional layer of variability that could have influenced results. Tris-based buffers were used to overcome the majority of negative side effects associated with longer fixation times, specifically RNA degradation, which has been well documented with prolonged fixation (von Ahlfen et al., 2007).

Due to the global variation of fluorescent intensities across specimens, we were unable to run a single algorithm in batch mode across the entire study that we interpreted to accurately represent the biological processes we aimed to characterize. This problem was addressed in an iterative validation process that is described in our methods. While we were able to provide more robust and reliable histopathology results relative to studies conducted without DIA, we could not establish easily reproducible data. For results from DIA pathogenesis research to become more reproducible, it will be critically important to standardize and automate tissue processing, differential tissue labeling and image acquisition. Additionally, reproducibility will require further refinement of image analysis software to overcome the limitations we encountered that warranted application of iterative semi-manual algorithm development, for which a standard set of parameters cannot simply be shared and adopted for future research.

Since our results are representative of a single 5 μm liver section from each of the 21 rhesus macaques enrolled in this study, our findings may not fully capture the potential global variability within this organ; however, our findings still provide novel quantitative insights into the temporal dissemination of EBOV within the liver

complemented by host spatial gene expression. Additionally, while we showed significant correlation between various measured biomarkers and histomorphological changes, correlation does not necessarily equal causation. Correlations could be directly linked (cause-effect) or indirectly linked by an additional biological process not characterized through our employed methodologies. Based on our approach, we cannot determine whether changes in one parameter directly caused changes in another and we cannot definitely conclude that merging of IHC and ISH biomarkers truly represented colocalization given the resolution limitations of epi-fluorescent microscopy. Future research investigating different combinations of biomarkers, comparing IHC and FISH results to clinical and hematological findings, and conducting dual IHC-FISH could provide additional insight into the relationship between host and viral biomarkers associated with EBOV pathogenesis in the liver.

Implications and Future Research

Although there were limitations to our research, given that Halo™ has not previously been used for EBOV research, we were able to optimize and validate DIA algorithms to produce quantitative results, which were highly correlated with observational findings, and provide clear evidence that DIA has the potential to facilitate more rigorous and efficient analysis for infectious disease pathogenesis. Application of DIA to our mIHC and FISH slides allowed us to reliably define host-response to EBOV in rhesus macaques, which can inform future models of disease and development of MCMs.

DIA results from NHP EBOV pathogenesis studies can serve as a reference for and inform development of novel disease models such as PHH and iPSC-derived hepatocyte infection models, multicellular in vitro platforms, and synthetic organ platforms (i.e. vascularized micro-liver), that more accurately recapitulate EBOV relative to immortalized cell lines. Analysis of correlation can be employed through quantitative analysis to validate or disprove proposed biological processes described using in vitro platforms. These new liver tissue models, if shown via DIA to faithfully recapitulate EBOV-induced host responses in the liver of infected NHPs, could complement use of NHPs as a more cost-effective, ethical and accessible model for EBOV pathogenesis research and drive discovery for, help to refine or eventually even replace animal models (Bennett et al., 2017).

Additionally, semi-quantitative ordinal scoring is not as effective a tool for precisely defining microscopic thresholds in pathogenesis studies because of the limitations previously discussed. Using DIA, thresholds representative of diagnostic or prognostic significance can be established through continuous quantitative datasets that are amenable to statistical analyses. Furthermore, these highly sensitive and quantitative thresholds can be used to investigate multi-institutional fidelity of NHP studies, or studies using other models for EBOV, among each other and in the context of natural disease in humans. DIA could even one day be used in experimental MCM studies to set thresholds for efficacy and precisely determine mechanism of action at the molecular level, which is required as part of pre-clinical development under the FDA's *"Animal Rule",* and for now can serve as high throughput screening platforms for drug candidates to then test in

animal models. Furthermore, DIA findings can be integrated with in vitro, omics, and other clinical and biological datasets, given their continuous quantitative nature, providing more robust and informative statistical information to confirm NHPs as an appropriate disease model and further accelerate MCM research. The NIAID IRF study, which provided our tissue samples, collected extensive data that will provide clinical, physiologic and gross findings that can then be integrated with our histologic data to inform model development for products requiring FDA approval.

The "*Animal Rule"* requires a "sufficiently well-characterized animal model for predicting the response in humans" for a given disease in order to use that animal in MCM trials (FDA, 2005). In order to use rhesus macaques and other NHPs in animal studies for approval of any MCMs for EBOV, additional knowledge and evidence of disease pathology, as provided in this study through use of DIA, could be of value. Current research has been able to demonstrate similarities in EBOV pathogenesis between humans and NHPs but DIA has the ability to measure the same trends, and possibly lack of statistically significant differences for them, in humans versus NHPs.

Although DIA is currently entirely a research tool and not yet validated or reproducible enough to use under Good Laboratory Practice (GLP), with further refinement and development DIA could one day become a useful approach for overcoming challenges to demonstrating MCM efficacy and mechanism of action to the degree required to gain approval under *"Animal Rule".* For example, a recent study evaluated efficacy of a recombinant inhibitor of TF as a treatment in EBOV-infected rhesus macaques (Geisbert et al., 2003b), after in vitro research showed that EBOV-

infected monocytes and macrophages overexpress TF (Geisbert et al., 2003b; Geisbert et al., 2003c). Using DIA, we were able to measure discrete changes in TF immunoreactivity within the liver over time and relate this to CD68 and VP35 immunoreactivity. Future research could use cell phenotyping, once better optimized, to accommodate the heterogeneity of cell phenotypes observed in whole organs in order to evaluate changes in TF immunoreactivity as well as in the total number of CD68+ macrophages colocalized with and likely coexpressing TF in control versus treated animals. These findings could then also be related to changes in survival rates. This would provide spatial and visual evidence of the efficacy of a TF inhibitor in mitigating progression of EBOV across time points post-exposure, and potentially further accelerate its approval as a host-directed therapy for EBOV.

Specifically for DIA of FISH, comparisons of hybridization patterns between sham and vaccine inoculated animals could one day help to fast-track vaccine approval under *"Animal Rule"*. Efficacy of the rVSV-EBOV vaccine, which produces EBOV GP to provoke a neutralizing immune response to infection, has been studied in NHPs using transcriptomics, which found via hematology that over 100 transcripts associated with the innate immune response, particularly ISGs, were differentially downregulated following vaccination (Menicucci et al., 2017). DIA of FISH could provide novel insights into the mechanism of action by which the vaccines alter the immune response in favor of the host following EBOV infection. This approach could also be of value in identifying which cell types drive the early immune response to EBOV infection. Findings could furthermore be used to develop treatments that target EBOV infection earlier on based on

cell-specific acute host responses.

Our findings corroborate past research that has demonstrated NHP fidelity to human EBOV infection and pathogenesis and indicated NHPs as a reliable model for MCM research (Piorkowski et al., 2017; Zaki & Goldsmith, 1999). Given the rarity of EBOV infected human clinical tissue specimens and the fact that it is not ethical to conduct clinical research outside of naturally occurring outbreaks, this study has built on previous experimental NHP models of EBOV. We have integrated novel quantitative outputs using DIA to characterize the temporal dissemination of EBOV within distinct liver cellular compartments and to characterize spatial gene responses known to play a role in EBOV pathogenesis and host response.

To further develop integration of DIA into pathology workflows for infectious disease research, Dr. Crossland has proposed a collaborative digital pathology pipeline for national and regional biocontainment laboratories. This pipeline would introduce cross-institution, cloud-based use of DIA. To date, for the most part, BSL-4 research has been siloed across the few institutions approved to work with category A bioterrorism agents like EBOV, leading to lack of standardization in interpreting and reporting of results and making it next to impossible to directly compare findings across studies conducted at different institutions (Fedchenko et al., 2014). Using DIA and shared algorithms, this can be overcome, particularly if pre-analytical standardization is improved through use of automated staining methods to minimize variability. Through sharing of results across a global network of institutions, analysis would be expedited, as would follow-up research.

Our findings provide new and significant details about EBOV pathogenesis and model development and refinement through the application of DIA. In comparing DIA to traditional models for histopathology, using findings from our own research as well as previous studies, we have shown that the value of DIA for infectious disease research could be exponential. DIA has the potential to reduce workload of analysis on veterinary pathologists, improve standardization and objectivity of results, foster collaboration and speed up research, and one day could contribute to development and approval of MCMs for urgent public health threats like EBOV.

Appendix I: Euthanasia Criteria

PARAMETER	DEGREE OF PARAMETER	SCORE
Overall clinical appearance; signs of hemorrhage	**Normal appearance, no petechial or ecchymotic hemorrhages**	**0**
	Facial edema, photophobia, cyanosis, prolonged coagulation profile	**2**
	Severe diarrhea, vomiting, dehydration, petechiae	**5**
	Persistent epistaxis, melena, retrobulbar hemorrhage	**10**
Respiratory rate, mucous membranes (MM) color, and Dyspnea (Difficulty breathing/labored respirations)	**Normal signs (Respiratory rate = 32 to 50 BPM; MM pink)**	**0**
	Mild (Respiratory rate = 51 to 65 BPM, with slightly increased effort; MM pale pink)	**2**
	Moderate (Respiratory rate = 66 to 80 BPM, with obvious difficulty breathing; MM muddy pink)	**7**
	Severe (Respiratory rate = > 80 BPM; respirations labored; MM blue)	**10**
Recumbency	**Normal – Not lying down when enter room**	**0**
	Lying down when enter room but gets up readily when approached	**5**
	Lying down when enter room but gets up with stimulation at cage front	**8**
	Lies down; will not get up even with excessive stimulation at cage front	**10**
Non-Responsiveness	**Normal – bright, alert, responsive**	**0**
	Mild, slightly depressed; slightly decreased appetite; puts head down when personnel in room; acts disinterested when personnel in room	**3**
	Moderately non-responsive; very disinterested in personnel; hunched or lying down; will get up when approached or prodded	**5**
	Severe; completely non-responsive to noxious stimuli such as toe-pinch; will not get up despite significant prodding	**10**
Core temperature of anesthetized animal (Normal in non-anesthetized macaque = 37 – 39°C = 98.6 – 102.2°F)	**>36.7°C (>98°F)**	**0**
	36.7>X>33.8°C (98-93.3°F)	**3**
	<33.8°C (<93.2°F)	**10**
Clinical score		*

Appendix II: mIHC Condition – 3

Table AI. Optimized conditions for mIHC-3.

Primary Antibody	*Animal and Isotype*	*Tissue marker*	Manufacturer, Catalog # and Lot #	Conc.	**TSA-conjugated Fluorochrome**	Manufacturer, Catalog # and Lot #	Conc.	**AR**
VP35	Ms IgG2b	EBOV Viral particles	Kerafast EMS703 090315	1/300	Green	PerkinElmer FP1487A 2380385	1/400	1
CK19 4E8	Ms IgG1	Oval cells, Biliary epithelium	ThermoFisher MA5-15884 TD2559278	1/600	Far red	PerkinElmer FP1497A 2491340	1/100	2
Smooth Muscle Actin (1A4 (asm-1))	Ms IgG2a	Myofibroblasts, Smooth Muscle	ThermoFisher MA5-11547 TF2585891C	1/600	Red	PerkinElmer FP1488A 2496488	1/200	3

Due to lack of staining specificity of Smooth Muscle Actin (SMA) in the red channel, quantitative digital image analysis was not performed for this assay. However, immunostained slides were scanned for observational analysis in Halo™. There was no visible merging of VP35 and SMA until 6 DPE, indicating that smooth muscle cells surrounding vessels in the liver were not visibly infected with EBOV at earlier time points. Merging of VP35 and CK19 was visible in single cells at 6 DPE but there did not appear to be merging of VP35 and CK19 at biliary ducts. Without DIA it was not possible to assess the degree of colocalization for CK19, SMA, and VP35 and changes in colocalization over time or whether there was any increase in percent area immunoreactive for CK19, which might be indicative of oval cell hyperplasia within the liver.

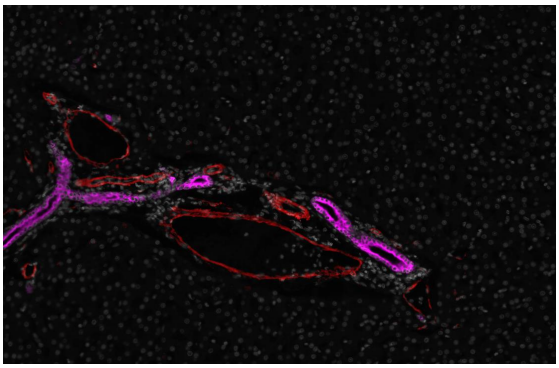

Control

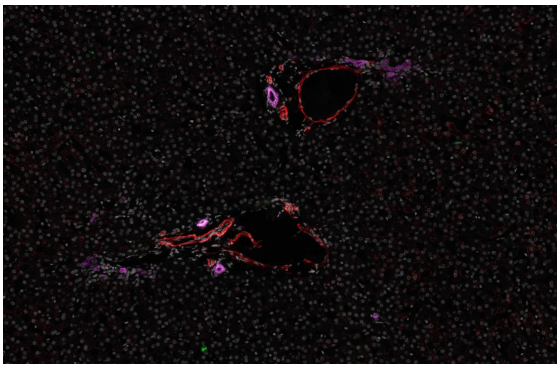

3 DPE

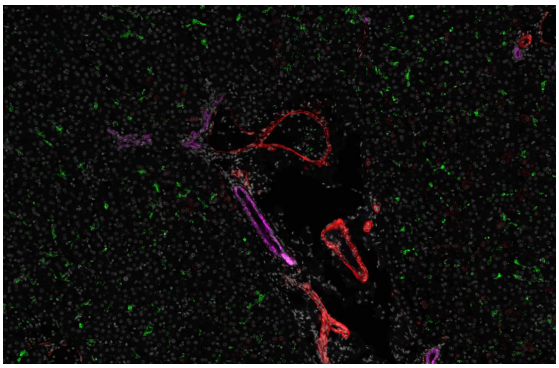

4 DPE

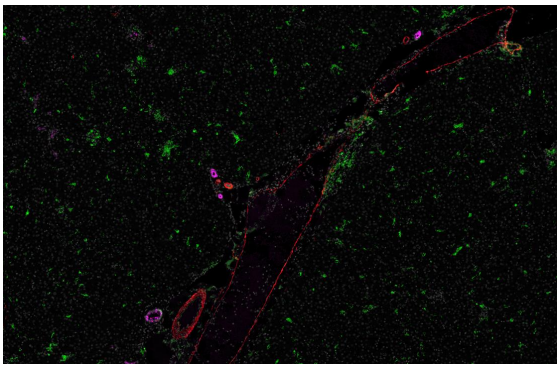

5 DPE

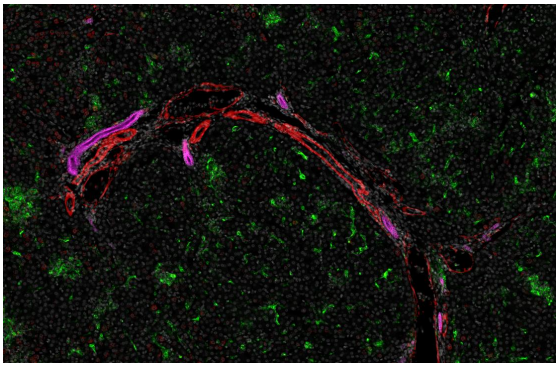

6 DPE

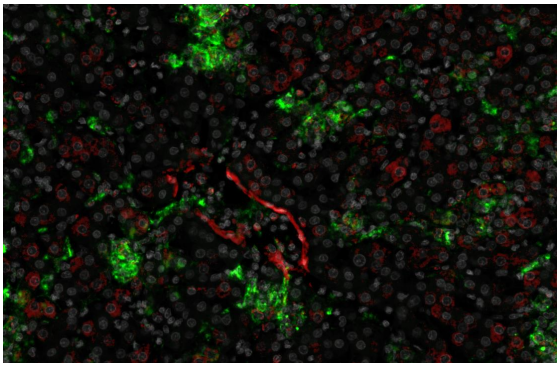

6 DPE; increased magnification

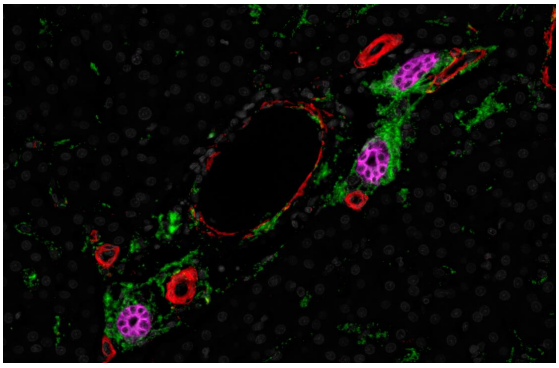

Terminal

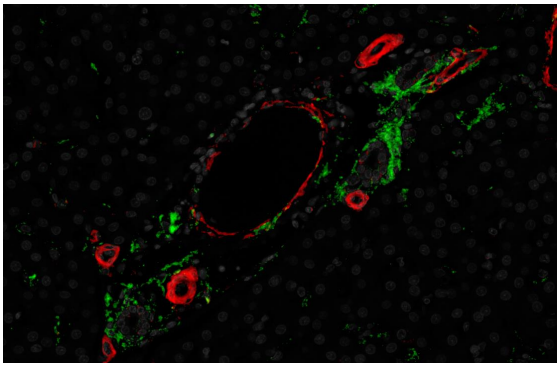

Terminal; Purple channel turned off

Figure AI. Changes over time in observation of VP35 (Green), Smooth Muscle Actin (Red) and CK19 (Cyan) in liver of EBOV-infected Rhesus Macaques.
6 DPE image with increased magnification shows that, even with color deconvolution, SMA is not only staining smooth muscle cells but is also diffusely positive in surrounding hepatocytes, indicating lack of specificity that would distort AQ and HP results.
Terminal image with purple channel turned off highlights lack of merging of CK19 and VP35 at biliary ducts.

Appendix III: VP35 mIHC-1 and mIHC-2 Correlation

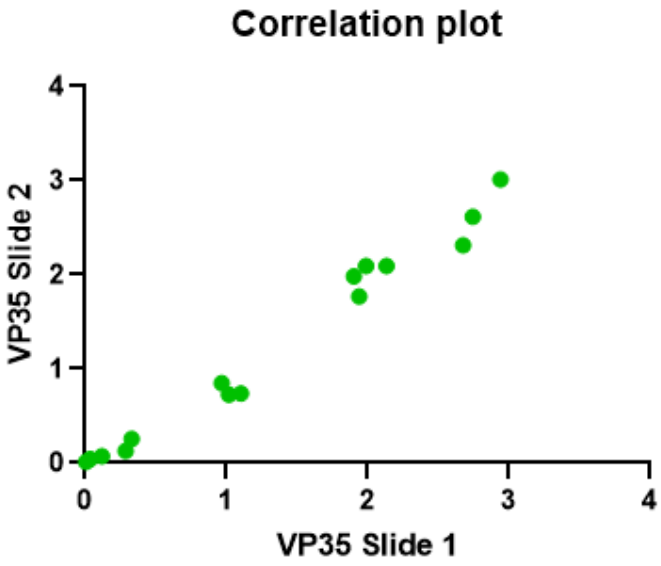

Figure: Correlation between percent total tissue area immunoreactive for VP35 in serial sections from assays 1 and 2.
Pearson's correlation coefficient **(***r) = 0.9909, P-value < 0.0001.*

Appendix IV: Simple linear regression of results

Outcome	Predictive Variable	Regression Equation	R-square	P-value
% VP35 Immunoreactivity	TF	Y = 0.8072*X + 0.1046	0.7493	<0.0001
	CD68	Y = 1.775*X + 2.357	0.8533	<0.0001
	MPO	Y = 0.6417*X + 0.6753	0.8000	<0.0001
	Heppar	Y = -4.587*X + 52.54	0.6666	<0.0001
	IL-6	Y = 0.1583*X + 0.04530	0.4014	0.0036
	ISG-15	Y = 0.3398*X + 0.1513	0.6046	<0.0001
Ordinal Liver Score	VP35	Y = 0.2817*X - 0.2568	0.6392	<0.0001
	Coloc. Of VP35, TF and CD68	Y = 0.02310*X - 0.01521	0.6710	<0.0001
	Coloc of VP35 and Heppar	Y = 0.02407*X - 0.002129	0.3990	0.0028
	IL-6	Y = 0.05835*X - 0.02923	0.4421	0.0014
	ISG-15	Y = 0.1017*X + 0.04820	0.5217	0.0003
Necrosis Score	VP35	Y = 0.9780*X + 0.04399	0.8335	<0.0001
	TF	Y = 0.8319*X + 0.09976	0.6934	<0.0001
	CD68	Y = 1.773*X + 2.401	0.7414	<0.0001
	MPO	Y = 0.6647*X + 0.6683	0.7478	<0.0001
	Heppar	Y = -4.955*X + 52.78	0.6777	<0.0001
	Coloc of VP35 and Heppar	Y = 0.07521*X + 0.02631	0.3875	0.0034
Inflammation Score	VP35	Y = 0.8665*X - 0.1967	0.7095	<0.0001
	TF	Y = 0.7533*X - 0.1268	0.6165	<0.0001
	CD68	Y = 1.743*X + 1.731	0.7776	<0.0001
	MPO	Y = 0.6529*X + 0.4183	0.7826	<0.0001
	Heppar	Y = -4.824*X + 54.59	0.6966	<0.0001
Fibrin Score	VP35	Y = 0.9403*X - 0.06119	0.6423	<0.0001
	TF	Y = 0.8378*X - 0.03155	0.5864	<0.0001
	CD68	Y = 1.859*X + 2.040	0.6798	<0.0001
	MPO	Y = 0.7078*X + 0.5212	0.7070	<0.0001
	Heppar	Y = -5.451*X + 54.07	0.6840	<0.0001

REFERENCES

Alfson, K. J., Avena, L. E., Beadles, M. W., Staples, H., Nunnely, J. W., … Griffiths, A. (2015). Particle-to-PFU Ratio of Ebola Virus Influences Disease Course and Survival in Cynomolgus Macaques. *Journal of Virology, 89*(13), 6773-6781. https://doi.org/10.1128/JVI.00649-15

Alfson, K. J., Avena, L. E., Worwa, G., Carrion, R., & Griffiths, A. (2017). Development of a Lethal Intranasal Exposure Model of Ebola Virus in the Cynomolgus Macaque. *Viruses, 9*(11), 319. https://doi.org/10.3390/v9110319

Baseler, L., Chertow, D. S., Johnson, K. M., Feldmann, H., Morens, D. M. (2017). The Pathogenesis of Ebola Virus Disease. *Annual Review of Pathology: Mechanisms of Disease, 12*(1), 387-418. https://doi.org/10.1146/annurev-pathol-052016-100506

Bennett, R. S., Huzella, L. M., Jahrling, P. B., Bollinger, L., Olinger, G. G., Hensley, L. E. (2017). Nonhuman Primate Models of Ebola Virus Disease. In: Mühlberger E., Hensley L., Towner J. (eds.) Marburg- and Ebolaviruses. *Current Topics in Microbiology and Immunology, 411*, 171-193. Retrieved from https://link.springer.com/chapter/10.1007%2F82_2017_20

Blackwell Science Ltd. (2001). Review: Interleukin 6 and Haemostasis. *British Journal of Haematology 115*, 3-12. Retrieved from https://onlinelibrary.wiley.com/doi/pdf/10.1046/j.1365-2141.2001.03061.x

Buseh, A. G., Stevens, P. E., Bromberg, M., Kelber, S. T. (2015). The Ebola epidemic in West Africa: Challenges, opportunities, and policy priority areas. *Nursing Outlook, 63*(1), 30-40. https://doi.org/10.1016/j.outlook.2014.12.013

Caballero, I. S., Honko, A. N., Gire, S. K., Winnicki, S. M., Melé, M., … Connor, J. H. (2016). In vivo Ebola virus infection leads to a strong innate response in circulating immune cells. *BMC Genomics, 17*, 707. https://doi.org/10.1186/s12864-016-3060-0

Carter, R. J., Cohn, A., Callis, A., Schuchat, A., Estivariz, C. F., Seward, J. F., Legardy-Williams, J. K., … Gibson, L. (2018). Implementing a Multisite Clinical Trial in the Midst of an Ebola Outbreak: Lessons Learned From the Sierra Leone Trial to Introduce a Vaccine Against Ebola. *The Journal of Infectious Diseases, 217*(1), S16–S23. https://doi.org/10.1093/infdis/jix657

Chughtai, A. A., Barnes, M., & Macintyre, C. R. (2016). Persistence of Ebola virus in various body fluids during convalescence: evidence and implications for disease transmission and control. *Epidemiology and Infection, 144*(8), 1652-60. https://doi.org/10.1017/S0950268816000054

Cooper, T. K., Huzella, L., Johnson, J., Rojas, O., Yellayi, S., … Zeng, X. (2018). Histology, immunohistochemistry, and in situ hybridization reveal overlooked Ebola virus target tissues in the Ebola virus disease guinea pig model. *Scientific Reports, 8*(1250). https://doi.org/10.1038/s41598-018-19638-x

Dhama, K., Karthik, K., Khandia, R., Chakraborty, S., Munjal, A., Latheef, S. K., … Chaicumpa, W. (2018). Advances in Designing and Developing Vaccines, Drugs, and Therapies to Counter Ebola Virus. *Frontiers in Immunology, 9*, 1803. https://doi.org/10.3389/fimmu.2018.01803

dos Santos, P. F. & Mansur, D. S. (2017). Beyong ISGlylation: Functions of Free Intracellular and Extracellular ISG15. *Journal of Interferon & Cytokine Research, 37*(6). http://doi.org/10.1089/jir.2016.0103

Dowall, S.D., Jacquot, F., Landon, J., Rayner, E.L., Hall, G., … Carroll, M.W. (2017). Post-exposure treatment of non-human primates lethally infected with Ebola virus with EBOTAb, a purified ovine IgG product. *Scientific Reports, 7*(4099). https://doi.org/10.1038/s41598-017-03910-7

El Sayed, S. M., Abdelrahman, A. A., Ozbak, H. A., Hemeg, H. A., Kheyami, A. M., Rezk, N., … Fathy, Y. M. (2016). Updates in diagnosis and management of Ebola hemorrhagic fever. *Journal of Research in Medical Sciences, 21*, 84. https://doi.org/10.4103/1735-1995.192500

Espeland, E. M., Tsai, C., Larsen, J., Disbrow, G. L. (2018). Safeguarding against Ebola: Vaccines and therapeutics to be stockpiled for future outbreaks. *PLoS Neglected Tropical Diseases, 12*(4), e0006275. https://doi.org/10.1371/journal.pntd.0006275

Fedchenko, N., & Reifenrath, J. (2014). Different approaches for interpretation and reporting of immunohistochemistry analysis results in the bone tissue - a review. *Diagnostic Pathology, 9*, 221. https://doi/10.1186/s13000-014-0221-9

Food and Drug Administration (FDA) Center for Drug Evaluation and Research (CDER). (2015). Product Development Under the Animal Rule: Guidance for Industry. Retrieved from https://www.fda.gov/downloads/drugs/guidances/ucm399217.pdf

Geisbert, T. W., Henley, L. E., Larsen, T., Young, H. A., Reed, D. S., Gesibert, J. B., Scott, D. P., … Davis, K. J. (2003a). Pathogenesis of Ebola Hemorrhagic Fever in Cynomolgus Macaques: Evidence that Dendritic Cells Are Early and Sustained Targets of Infection. *The American Journal of Pathology, 163*(6), 2347-2370. https://doi.org/10.1016/S0002-9440(10)63591-2

Geisbert, T. W., Hensley, L. E., Davis, K. J., Jahrling, P. B., Young, H. A., & Kagan, E. (2003b). Mechanisms Underlying Coagulation Abnormalities in Ebola Hemorrhagic Fever: Overexpression of Tissue Factor in Primate Monocytes/Macrophages Is a Key Event. *The Journal of Infectious Diseases, 188*(11), 1618–1629. http://doi.org/10.1086/379724

Geisbert, T. W., Hensley, L. E., Jahrling, P. B., Larsen, T., Geisbert, J. B., Paragas, J., … Vlasuk, G. P. (2003c). Treatment of Ebola virus infection with a recombinant inhibitor of factor VIIa/tissue factor: a study in rhesus monkeys. *The Lancet, 362*(9400), 1953–1958. http://doi.org/10.1016/S0140-6736(03)15012-X

Hayden, F. G., Bausch, D. G., Friede, M. (2017). Experimental therapies for Ebola Virus Disease: What have we learned? *The Journal of Infectious Diseases, 215*(2), 167-170. https://dx.doi.org/10.1093/infdis/jiw496

Hellman, J. (2015). Addressing the Complications of Ebola and Other Viral Hemorrhagic Fever Infections: Using Insights from Bacterial and Fungal Sepsis. *PLoS Pathogens, 11*(10), e1005088. https://doi.org/10.1371/journal.ppat.1005088

Herman, M., & Bogunvic, D. (2017). ISG15: In Sickness and in Health. *Trends in Immunology, 38*(2), 79-93. http://dx.doi.org/10.1016/j.it.2016.11.001

Hoenen, T., Groseth, A., Flazarano, D., Feldmann, H. (2006). Ebola virus: unravelling pathogenesis to combat a deadly disease. *Trends in Molecular Medicine, 12*(5), 206-215.

Hutchinson, K. L. & Rollin, P. E. (2007). Cytokine and Chemokine Expression in Humans Infected with Sudan Ebola Virus. *The Journal of Infectious Diseases, 196*(2), S357–S363. https://doi.org/10.1086/520611

Johnson, E., Jaax, N., White, J., Jahrling, P. (1995). Lethal experimental infections of rhesus monkeys by aerosolized Ebola virus. *International Journal of Experimental Pathology, 76*(4), 227-236. Retrieved from https://www.ncbi.nlm.nih.gov/pmc/articles/PMC1997182/

Kaushik N, & Green S (2014). Pre-analytical errors: their impact and how to minimize them. *MLO Medical Laboratory Observer, 46*(5): 22, 24, 26. Retrieved from https://www.mlo-online.com/home/article/13006606/preanalytical-errors-their-impact-and-how-to-minimize-them

Lai, C., Strange, D. P., Wong, T. A. S., Lehrer, A. T., Verma, S. (2017). Ebola Virus Glycoprotein induces an Innate Immune Response In vivo via TLR4. *Frontiers in Microbiology, 8*, 1571. https://doi.org/10.3389/fmicb.2017.01571

Lämmermann, T., & Kienle, K. (2016). Neutrophil swarming: an essential process of the neutrophil tissue response. *Immunological Reviews, 273*(1), 76–93. http://doi.org/10.1111/imr.12458

Lee, J. E., & Saphire, E. O. (2009). Ebolavirus glycoprotein structure and mechanism of entry. *Future Virology, 4*(6), 621-635. https://doi.org/10.2217/fvl.09.56

Lefebvre, A., Fiet, C., Belpois-Duchamp, C., Tiv, M., Astruc, K., Aho Glélé, L. S. (2014). Case fatality rates of Ebola virus diseases: A meta-analysis of World Health Organization data. *Médecine et Maladies Infectieuses, 44*(9), 412-416. https://doi.org/10.1016/j.medmal.2014.08.005

Lin, K. L., Twenhafel, N. A., Connor, J. H., Cashman, K. A., Shamblin, J. D., Donnelly, G. C., Mulltiplex immunofluorescence OV and ensure that in Marburg Virus Angola Infection following Aerosol Challenge in Rhesus Macaques. *Journal of Virology, 89*(19), 9875.

Lubaki, N. M., Younan, P., Santos, R. I., Meyer, M., Iampietro, M., … Bukreyev,A. (2016). The Ebola Interferon Inhibiting Domains Attenuate and Dysregulate Cell-Mediated Immune Responses. *PLoS Pathogens, 12*(12), e1006031. https://doi.org/10.1371/journal.ppat.1006031

Madara, J. J., Han, Z., Ruthel, G., Freedman, B. D., Harty, R. N. (2015). The multifunctional Ebola virus VP40 matrix protein is a promising therapeutic target. *Future Virology, 10*(5), 537-546. https://doi.org/10.2217/fvl.15.6

Madelain, V., Baize, S., Jacquot, F., Reynard, S., Fizet, A., … Gueclj, J. (2018). Ebola viral dynamics in nonhuman primates provides insights into virus immuno-pathogenesis and antiviral strategies. *Nature Communications, 9*(4013). https://doi.org/10.1038/s41467-018-06215-z

Martines, R. B., Ng, D. L., Greer, P. W., Rollin, P. E., & Zaki, S. R. (2014). Tissue and cellular tropism, pathology and pathogenesis of Ebola and Marburg Viruses. *The Journal of Pathology, 235*(2), 153-174. https://doi.org/10.1002/path.4456

Marzi, A., Feldmann, F., Hanley, P. W., Scott, D. P., Günther, S., & Feldmann, H. (2015). Delayed Disease Progression in Cynomolgus Macaques Infected with Ebola Virus Makona Strain. *Emerging Infectious Diseases, 21*(10), 1777–1783. https://doi/10.3201/eid2110.150259

McElroy, A. K., Shrivastava-Ranjan, P., Harmon, J. R., Martines, R. B., Silva-Flannery, L., Flietstra, T. D....Spiropoulou, C. F. (2019). Macrophage Activation Marker Soluble CD163 Associated with Fatal and Severe Ebola Virus Disease in Humans. *Emerging Infectious Diseases, 25*(2), 290-298. https://dx.doi.org/10.3201/eid2502.181326

Meyers, L., Frawley, T., Gross, S., Kang, C. (2015). Ebola Virus Outbreak 2014: Clinical Review for Emergency Physicians. *Annals of Emergency Medicine, 65*(1), 101-108. https://doi.org/10.1016/j.annemergmed.2014.10.009

Mohamadzadeh, M., Coberley, S. S., Olinger, G. G., Kalina, W. V, Ruthel, G., Fuller, C. L., … Schmaljohn, A. L. (2006). Activation of Triggering Receptor Expressed on Myeloid Cells-1 on Human Neutrophils by Marburg and Ebola Viruses. *Journal of Virology*, *80*(14), 7235 LP-7244. http://doi.org/10.1128/JVI.00543-06

Mühlberger, E., & Hensley, L. L. (2017). Marburg- and Ebolaviruses: From Ecosystems to Molecules (Marburg- and Ebolaviruses: From Ecosystems to Molecules No. 411) (pp. 1–460). https://doi.org/10.1007/978-3-319-68948-7

Nakayama, E., & Saijo, M. (2013). Animal models for Ebola and Marburg virus infections. *Frontiers in Microbiology, 4*, 267. https://doi.org/10.3389/fmicb.2013.00267

National Institute of Allergy and Infectious Diseases (NIAID). (2018). Investigational Therapeutics for the Treatment of People with Ebola Virus Disease (ClinicalTrials.gov Identifier: NCT03719586). Retrieved from https://clinicaltrials.gov/ct2/show/NCT03719586?term=mab114&rank=2

Okumura, A., Pitha, P. M., Yoshimura, A., & Harty, R. N. (2009). Interaction between Ebola virus glycoprotein and host toll-like receptor 4 leads to induction of proinflammatory cytokines and SOCS1. *Journal of Virology, 84*(1), 27–33. https://doi:10.1128/JVI.01462-09

Olejnik, J., Forero, A., Deflubé, L. R., Hume, A. J., Manhart, W. A., Nishida, A., … Mühlberger, E. (2017). Ebolaviruses Associated with Differential Pathogenicity Induce Distinct Host Responses in Human Macrophages. *Journal of Virology, 91*(11), e00179-17. https://doi/10.1128/JVI.00179-17

Perry, D. L., Bollinger, L., & White, G. L. (2012). Perry, D. L., Bollinger, L., & White, G. L. (2012). The Baboon (Papio spp.) as a model of human Ebola virus infection. *Viruses, 4*(10), 2400-16. https://doi.org/10.3390/v4102400

Piorkowski, F. J., Quérat, G., Carbonnelle, C., Pannetier, D., Mentré, F., … de Lamballerie, X. (2017). Implementation of a non-human primate model of Ebola disease: Infection of Mauritian cynomolgus macaques and analysis of virus populations. *Antiviral Research, 140*, 95-105. https://doi.org/10.1016/j.antiviral.2017.01.017

Rao, S., Masilamani, S., Sundaram, S., Duvuru, P., & Swaminathan, R. (2016). Quality Measures in Pre-Analytical Phase of Tissue Processing: Understanding Its Value in Histopathology. *Journal of Clinical and Diagnostic Research, 10*(1), EC07–EC11. https://doi/10.7860/JCDR/2016/14546.7087

Reisler, R. B., Yu, C., Donofrio, M. J., Warren, T. K., Wells, K. S., Garza, N. L., … Cardile, A. P. (2017). Clinical Laboratory Values as Early Indicators of Ebola Virus Infection in Nonhuman Primates. *Emerging Infectious Disease Journal, 23*(8), 1316. https://doi.org/10.3201/eid2308.170029

Rizzardi, A. E., Johnson, A. T., Vogel, R. I., Pambuccian, S. E., Henriksen, J., Skubitz, A. P. N., … Schmechel, S. C. (2012). Quantitative comparison of immunohistochemical staining measured by digital image analysis versus pathologist visual scoring. *Diagnostic Pathology, 7*(1), 42. http://doi.org/10.1186/1746-1596-7-42

Ryabchikova, E. I., Kolesnikova, L. V, & Luchko, S. V (1999). An Analysis of Features of Pathogenesis in Two Animal Models of Ebola Virus Infection. *The Journal of Infectious Diseases, 179*(Supplement_1), S199–S202. http://doi.org/10.1086/514293

Siragam, V., Wong, G., & Qiu, X. G. (2018). Animal models for filovirus infections. *Zoological Research, 39*(1), 15–24. https://doi/10.24272/j.issn.2095-8137.2017.053

Smither, S. J., Nelson, M, Eastaugh, L., Nunez, A., Salguero, F. J., Lever, M. S. (2015). Experimental Respiratory Infection of Marmosets (Callithrix jacchus) With Ebola Virus Kikwit. *The Journal of Infectious Diseases, 212*(2), 1S336–S345. https://doi.org/10.1093/infdis/jiv371

Snead, D. R. J., Tsang, Y.-W., Meskiri, A., Kimani, P. K., Crossman, R., Rajpoot, N. M., … Cree, I. A. (2016). Validation of digital pathology imaging for primary histopathological diagnosis. *Histopathology, 68*(7), 1063–1072. http://doi.org/10.1111/his.12879

Snoy, P. J. (2010). Establishing Efficacy of Human Products Using Animals: The US Food and Drug Administration's "Animal Rule." *Veterinary Pathology, 47*(5), 774–778. https://doi.org/10.1177/0300985810372506

Spiropoulou, C. F., Spengler, J. R., Nichol, S. T., Saturday, G., Lavender, K. J., Martellaro, C., … Keck, J. G. (2017). Severity of Disease in Humanized Mice Infected With Ebola Virus or Reston Virus Is Associated With Magnitude of Early Viral Replication in Liver. *The Journal of Infectious Diseases, 217*(1), 58–63. http://doi.org/10.1093/infdis/jix562

Speranza, E., & Connor, J. H. (2017). Host Transcriptional Response to Ebola Virus Infection. *Vaccines, 5*(3), 30. https://doi.org/10.3390/vaccines5030030

Speranza, E., Bixler, S. L., Altamura, L. A., Arnold, C. E., Pratt, W. D., Taylor-Howell, C., … Connor, J. H. (2018). A conserved transcriptional response to intranasal Ebola virus exposure in nonhuman primates prior to onset of fever. *Science Translational Medicine, 10*(434). https://doi.org/10.1126/scitranslmed.aaq1016

St Claire, M. C., Ragland, D. R., Bollinger, L. & Jahrling, P. B. (2017). Animal Models of Ebolavirus Infection. *Comparative Medicine, 67*(3), 253–262. Retrieved from https://www.ncbi.nlm.nih.gov/pmc/articles/PMC5482517/?report=classic

Takamatsu, Y., Kolesnikova, L., & Becker, S. (2018). Transport of Ebola virus nucleocapsids. *Proceedings of the National Academy of Sciences of the United States of America, 115*(5), 1075-1080. https://doi.org/10.1073/pnas.1712263115

Tanaka, T., Narazaki, M., & Kishimoto, T. (2014). IL-6 in inflammation, immunity, and disease. *Cold Spring Harbor Perspectives in Biology, 6*(10), a016295. https://doi/10.1101/cshperspect.a016295

van der Ven, A. J., Netea, M. G., van der Meer, J. W., & de Mast, Q. (2015). Ebola Virus Disease has Features of Hemophagocytic Lymphohistiocytosis Syndrome. *Frontiers in Medicine, 2*, 4. doi:10.3389/fmed.2015.00004

von Ahlfen, S., Missel, A., Bendrat, K., & Schlumpberger, M. (2007). Determinants of RNA quality from FFPE samples. *PLoS One, 2*(12), e1261. https://doi.org/10.1371/journal.pone.0001261

Webster, J. D., & Dunstan, R. W. (2014). Whole-Slide Imaging and Automated Image Analysis: Considerations and Opportunities in the Practice of Pathology. *Veterinary Pathology, 51*(1), 211-223. https://doi.org/10.1177/0300985813503570

Wyers, M., Fernandez, B., Le Guenno, B., Boesch, C., Guigand, L., Formenty, P., & Cherel, Y. (1999). Histopathological and Immunohistochemical Studies of Lesions Associated with Ebola Virus in a Naturally Infected Chimpanzee. *The Journal of Infectious Diseases, 179*(Supplement 1), S54–S59. http://doi.org/10.1086/514300

Zaki, S. & Goldsmith, C. (1999). Pathologic features of filovirus infections in humans. *Current Topics in Microbiology and Immunology, 235*, 97–116. Retrieved from https://www.ncbi.nlm.nih.gov/pubmed/9893381

Zeng, X., Blancett, C. D., Koistinen, K. A., Schellhase, C. W., Bearss, J. J., Radoshitzky, S. R., … Sun, M. G. (2017). Identification and pathological characterization of persistent asymptomatic Ebola virus infection in rhesus monkeys. *Nature Microbiology, 2*(17113). https://doi.org/10.1038/nmicrobiol.2017.113

CURRICULUM VITAE